		Form Approved OMB No. 074-0188

REPORT DOCUMENTATION PAGE

Public reporting burden for this collection of information is estimated to average 1 hour per response, including g the time for reviewing instructions, searching existing data sources, gathering and maintaining the data needed, and completing and reviewing the collection of information. Send comments regarding this burden estimate or any other aspect of the collection of information, including suggestions for reducing this burden to Washington Headquarters Services, Directorate for Information Operations and Reports, 1215 Jefferson Davis Highway, Suite 1204, Arlington, VA 22202-4302, and to the Office of Management and Budget, Paperwork Reduction Project (0704-0188), Washington, DC 20503.

1. AGENCY USE ONLY (Leave blank)	2. REPORT DATE 4 May 2007	3. REPORT TYPE AND DATE COVERED

4. TITLE AND SUBTITLE Nonlinear Acoustic Landmine Detection: Profiling Soil Surface Vibrations and Modeling Mesoscopic Elastic Behavior	5. FUNDING NUMBERS

6. AUTHOR(S)
 Genis, Sean A.

7. PERFORMING ORGANIZATION NAME(S) AND ADDRESS(ES)		8. PERFORMING ORGANIZATION REPORT NUMBER

9. SPONSORING/MONITORING AGENCY NAME(S) AND ADDRESS(ES)		10. SPONSORING/MONITORING AGENCY REPORT NUMBER
US Naval Academy Annapolis, MD 21402		Trident Scholar project report no. 352 (2007)

11. SUPPLEMENTARY NOTES

12a. DISTRIBUTION/AVAILABILITY STATEMENT This document has been approved for public release; its distribution is UNLIMITED.	12b. DISTRIBUTION CODE

13. ABSTRACT Acoustic-to-seismic (A/S) coupling involving airborne sound is used to generate soil vibrations that interact with the top plate of a buried landmine. Due to scattering, the interaction at the soil-mine interface produces an enhanced and strongly nonlinear soil surface vibration directly over the buried landmine. Resonant tuning curves of the soil-mine system show that the nonlinear behavior observed near resonance for "on the mine" locations is considerably stronger that that seen "off the mine." This suggests that some false alarms due to the resonant effects of the ground's natural layering may be eliminated by comparing the frequency softening in resonant tuning curves between "off" and "on target" locations. Experiments with the soil-mass oscillator (SMO) apparatus show that the nonlinear acoustic landmine detection problem involves mesoscopic nanoscale nonlinear elastic behavior. Resonant tuning curves have linear backbones, a behavior also characteristic of certain geomaterials (sandstone). Elasto-slip (Iwan 1966) and LISA (Scalerandi *et al* 2002) models of hysteresis are used to explain this phenomenon. The soil-mine interface, which is modeled using a soil-plate oscillator (SPO) apparatus, is extremely nonlinear. The SPO is excited using both acoustic and electromagnetic means. A/S coupling experiments are employed to simultaneously measure vibrations at the underside of a buried clamped plate and the soil surface. Electrodynamic experiments determine the motional impedance of a combined soil-plate system. (continued on p.2)

14. SUBJECT TERMS
hysteresis, mesoscopic, nonlinear, nonclassical nonlinearity, acoustic landmine detection

15. NUMBER OF PAGES 122
16. PRICE CODE

17. SECURITY CLASSIFICATION OF REPORT	18. SECURITY CLASSIFICATION OF THIS PAGE	19. SECURITY CLASSIFICATION OF ABSTRACT	20. LIMITATION OF ABSTRACT

NSN 7540-01-280-5500
 (Rev.2-89)

Standard Form 298
Prescribed by ANSI Std. Z39-18
298-102

(continued from p.1) At large drive amplitudes, the backbone curves obtained from the SPO exhibit more complicated behavior, which is described using a bilinear hysteresis model (Caughey 1966). Nonlinear acoustic landmine detection experiments are performed in the anechoic chamber facility using both a buried acrylic drum-like mine simulant and a VS 1.6 plastic anti3 tank landmine. Using an automated laser Doppler vibrometer, soil surface vibrations are profiled as a function of scan position. Elements of both the elasto-slip and bilinear hysteresis models appear in these experiments.

NONLINEAR ACOUSTIC LANDMINE DETECTION:
PROFILING SOIL SURFACE VIBRATIONS AND MODELING MESOSCOPIC ELASTIC BEHAVIOR

By

Midshipman 1/c Sean A. Genis
United States Naval Academy
Annapolis, Maryland

Certification of Adviser Approval

Professor Murray S. Korman
Physics Department

Acceptance for the Trident Scholar Committee

Professor Joyce E. Shade
Deputy Director of Research & Scholarship

USNA-1531-2

Abstract

Acoustic-to-seismic (A/S) coupling involving airborne sound is used to generate soil vibrations that interact with the top plate of a buried landmine. Due to scattering, the interaction at the soil-mine interface produces an enhanced and strongly nonlinear soil surface vibration directly over the buried landmine. Resonant tuning curves of the soil-mine system show that the nonlinear behavior observed near resonance for "on the mine" locations is considerably stronger that that seen "off the mine." This suggests that some false alarms due to the resonant effects of the ground's natural layering may be eliminated by comparing the frequency softening in resonant tuning curves between "off" and "on target" locations.

Experiments with the soil-mass oscillator (SMO) apparatus show that the nonlinear acoustic landmine detection problem involves mesoscopic nanoscale nonlinear elastic behavior. Resonant tuning curves have linear backbones, a behavior also characteristic of certain geomaterials (sandstone). Elasto-slip (Iwan 1966) and LISA (Scalerandi *et al* 2002) models of hysteresis are used to explain this phenomenon.

The soil-mine interface, which is modeled using a soil-plate oscillator (SPO) apparatus, is extremely nonlinear. The SPO is excited using both acoustic and electromagnetic means. A/S coupling experiments are employed to simultaneously measure vibrations at the underside of a buried clamped plate and the soil surface. Electrodynamic experiments determine the motional impedance of a combined soil-plate system. At large drive amplitudes, the backbone curves obtained from the SPO exhibit more complicated behavior, which is described using a bilinear hysteresis model (Caughey 1966).

Nonlinear acoustic landmine detection experiments are performed in the anechoic chamber facility using both a buried acrylic drum-like mine simulant and a VS 1.6 plastic anti-

tank landmine. Using an automated laser Doppler vibrometer, soil surface vibrations are profiled as a function of scan position. Elements of both the elasto-slip and bilinear hysteresis models appear in these experiments.

Acknowledgments

Table of Contents

List of Figures

List of Tables

Chapter 1 – Introduction

Historical Background

Landmines are present in more than 80 nations and contaminate more than 200,000 square kilometers of the world's landmass. Though accurate numbers are difficult to obtain the number of annual casualties caused by landmines is estimated to be upward of 6,500 per year.[1]

On an even more frightening scale, this amounts to more than 17 casualties per day around the globe. And in addition to severe human suffering, the presence of landmines also creates tremendous economic problems. Transit is difficult through potentially mined areas, and the threat of a single mine can often render otherwise fertile farmland useless. Per the 1997 Ottawa Treaty, also known as the Mine Ban Treaty, more than 140 signatories are undertaking mine clearance efforts. However, at the current rate of progress complete demining will require between 450 and 500 years.

History of Nonlinear Acoustic Landmine Detection

Nonlinear acoustic landmine detection has shown tremendous promise in recent years. Many anti-personnel and anti-tank mines are made predominantly from plastic components, making conventional detection schemes involving ground penetrating radar or metal detection extremely difficult and unreliable.

Over the past ten years, Dr. James Sabatier (at the University of Mississippi's National Center for Physical Acoustics) has documented that acoustical methods can accurately locate certain types of plastic anti-tank and anti-personnel mines (VS1.6, VS2.2) that are buried in gravel road beds. In particular, acoustic-to-seismic (A/S) coupling techniques have shown tremendous promise in reducing false alarm rates, which is critical for any practical detection technology.[2,3]

In Sabatier's setup, loudspeakers placed roughly 1 to 2 meters above the ground 10generate airborne acoustic pressure waves which interact at the surface of the ground to create seismic disturbances in the soil. The vibrations in the soil then interact with the top plate structure of the buried mine to produce an identifiable response.

At low frequencies (around 100 Hz) the wavelength of acoustic pressure waves is relatively long in comparison to the both the burial depth and thickness of an unearthed landmine. This justifies a lump-element treatment of the soil, mine case, and coupled soil-mine oscillator. For the case of a simple damped, linear treatment, the lump-element models of the soil (Figure 1), mine casing (Figure 2), and coupled soil-mine oscillator (Figure 3) are shown below.
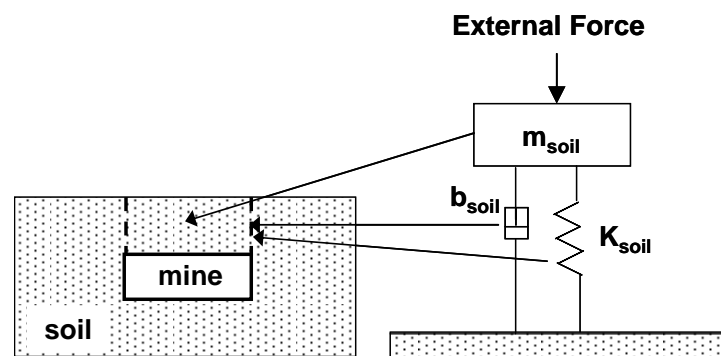
Figure 1 – Linear model of soil as a damped spring
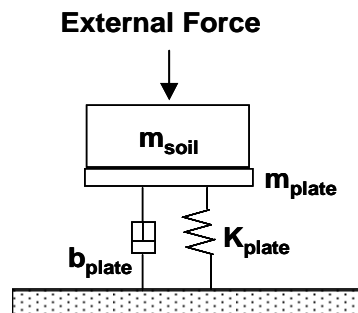
Figure 2 – Linear model of the top plate of a landmine as an elastic plate with lump-element mass loading

External Force
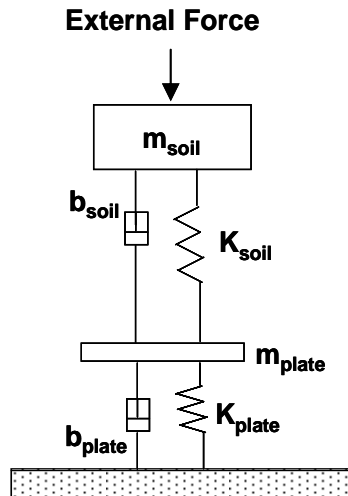
Figure 3 – Linear model of a soil and elastic plate coupled oscillator

Building upon the tremendous success of Sabatier's work, Donskoy[4] has further

improved upon acoustic detection techniques by introducing a physical model that incorporates

nonlinear characteristics. Nonlinear acoustic landmine detection schemes have proven

additionally effective at reducing and eliminating certain types of false alarms. Donskoy's

nonlinear vibro-acoustic technique for acoustic landmine detection arises from the fact that a

mine casing is much more compliant than a buried rock, metal debris, or roots. Soil oscillations

observed over such a compliant object are seen to exhibit strong nonlinear behavior that arises

primarily from interactions at the interface between the soil and the elastic top plate of a buried

landmine.

External Force
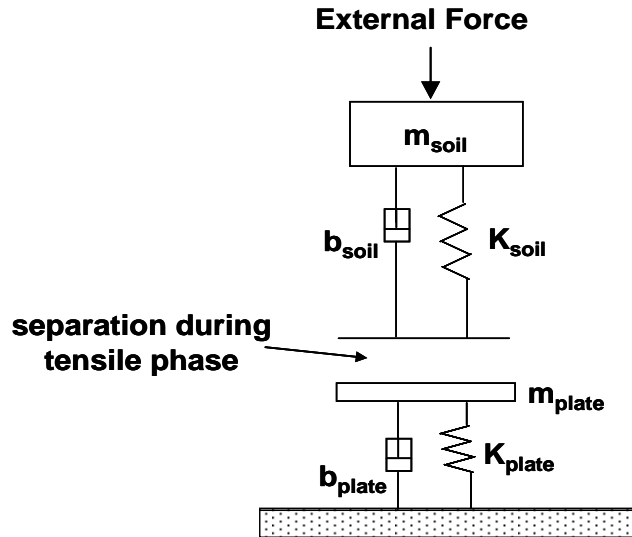
Figure 4 – Nonlinear model depicting separation between the elastic top plate of a landmine and soil during the tensile phase of oscillation

External Force
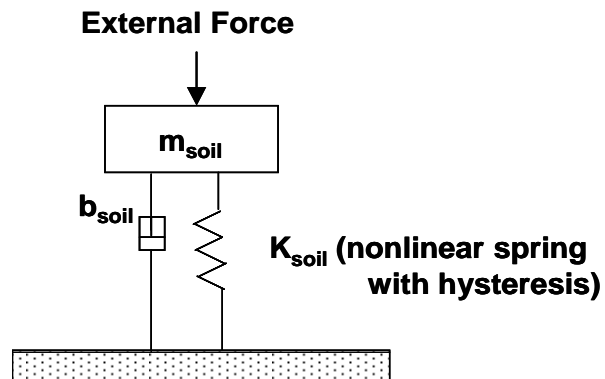
Figure 5 – Nonlinear model of soil as a hysteretic medium

F cos(wt)
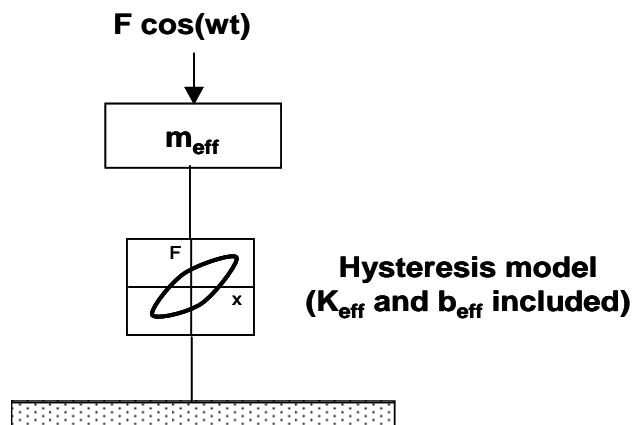
Figure 6 – Nonlinear model of the soil-mine system in agreement with a well-defined theory for bilinear hysteresis

Figure 4 is a description of the original one-dimensional nonlinear system proposed by Donskoy.[4]   Like Figure 3, both the plate and the soil are defined by their own elastic parameters. However, as the plate oscillates it causes a more complicated nonlinear vibration interaction with surrounding soil. Though not fully understood, there are believed to be partial separation effects between the soil column and the plate. In a simplified sense, these separation effects are modeled by the gap depicted in the Figure 4. The significant nonlinear behavior that arises from the partial separation and other nonlinear effects may be easily measured at the soil surface using a laser Doppler vibrometer (LDV), accelerometer, or geophone along with a spectrum analyzer.

In studying the effects of the soil-mine system, it is important to realize that the soil also exhibits its own nonlinear behavior. Figure 5 addresses this behavior by modeling the elastic behavior of the soil as a nonlinear spring. The question that arises, then, is to what extent the nonlinearity of the soil contributes to the overall nonlinearity observed when searching for landmines. In order to address this problem, a variety of experiments have been designed to isolate various facets of the intricate soil-mine oscillator.

The Soil-Mass Oscillator (SMO) facilitates the nonlinear study of soil alone. The experimental apparatus (described in more detail on pages 18-19 of this report) consists of a rigid steel toroid atop a rigid platform. Inside the toroid is a column of soil, sitting beneath a rigid mass plug. Mass loading experiments are used to determine the elastic stiffness of the soil medium. Resonant tuning curve experiments show that the nonlinearity inherent to the soil is mesoscopic elastic, or nonclassical, in nature because the detuning of the resonant frequency occurs as a linear function of the displacement amplitude of oscillation. The nonlinearity arises from a mesoscopic stress-strain hysteresis in the granular lattice structure, as shown in Figure 6,

which is similar to the behavior observed in geomaterials such as sandstone. An elasto-slip model composed of a series-parallel model of Jenkin's elements[5] is used to quantify the degree of nonlinearity inherent to the soil. A statistical model based upon a Preisach-Mayergoyz (PM) formalism[6] is also examined as a viable option for explaining the mesoscopic nanoscale elastic behavior.

The Soil Plate Oscillator (SPO) consists of a soil column resting atop a thin clamped plate and supported within a short cylindrical tube. The SPO affords an opportunity to study the contributions of the soil-top plate interface to the overall nonlinearity of the buried landmine system. A clamped plate without soil mass-loading is considered to be a very well behaved linear system. When a soil column is added above the clamped plate, resonant tuning curve experiments show the system to be nonlinear. If the plate is thick enough to be considered rigid, the nonlinearity observed is due predominantly to the soil alone. However, if the plate is relatively thin and compliant in comparison to the stiffness of the soil column, the observed nonlinearity results from the combined effects of soil and soil-plate interface nonlinearity. For low amplitude excitation, the elasto-slip and PM models predict the resonant behavior witnessed in the system. For extremely thin plates subjected to large excitation levels, though, a model exhibiting bilinear hysteretic behavior[7] proves to be more useful.

The aggregate effects of soil and soil-plate nonlinearity, namely the acoustic-to-seismic coupling excitation and the subsequent near-field scattering that generates enhanced soil surface vibrations, are examined using a buried acrylic mine simulant and a plastic VS 1.6 Italian anti-tank mine. A self-designed LabVIEW® control system is used to conduct one- and two-dimensional profiles of soil surface vibrations. Here, computer controlled stepper motors position a laser Doppler vibrometer (LDV) in a discrete scan pattern in order to profile soil

surface vibrations both on and off the target. Data is saved directly to a computer (AMD

Athlon^{TM} XP 2200+ processor, 1.84 GHz, 512 MB RAM) in a fully automated process.

The observed behavior from resonant tuning curve experiments of the buried simulant

and VS 1.6 corresponds very closely to results obtained from SMO and SPO experiments. That

is, resonant frequency softening corresponding to an increase in acoustic drive amplitude is

witnessed. The behavior over a compliant object, either mine or mine simulant, is more similar

to the bilinear hysteretic model employed in the case of the SPO. Conversely, off target behavior

is more akin to the elasto-slip model used in analyzing the SMO.

Experiments are also conducted in order to determine the limitations of "forward-

looking" mine detection. The rough surface scattering which enables a LDV to be used when

measuring soil-surface vibrations also limits detection at shallow grazing angles. Shallow

grazing angles often cause a noisy speckle pattern that inhibits forward-looking mine detection.

At some minimum grazing angle the signal-to-noise ratio becomes so weak that no resonant

response is detectable. Forward scattering experiments are performed to determine the limiting

grazing angle in the experimental system.

Chapter 2 – Experimental Procedures and Results

2.1 Soil Mass Oscillator

The granular nature of soil makes it an inherently nonlinear medium. In order to accurately interpret the nonlinear responses observed in systems involving buried landmines or landmine simulants, it is first necessary to separate and examine the nonlinear contributions of the soil itself.

The soil-mass oscillator, depicted in Figure 7, is built for the purpose of studying the nonlinear properties of the soil medium alone. A soil sample is enclosed by a thick-walled steel toroid, concrete platform, and aluminum slug. This setup creates a soil column reminiscent of the rods of geomaterials used when performing resonant bar experiments.[8] An Agilent 35670A spectrum analyzer generates a swept sine signal that is amplified to drive a 12-inch diameter subwoofer positioned two feet above the soil-mass oscillator. The massive concrete slab base is needed to reduce the natural resonant vibration frequencies of the concrete floor in the laboratory room. A geophone placed on top of the aluminum slug measures soil surface vibrationsm which are digitally recorded by the Agilent spectrum analyzer. (More detailed specifications and descriptions of all the experimental equipment used, including the Agilent spectrum analyzer and the geophone, are included in Appendix A). Apart from daily environmental changes involving temperature and humidity, the only variable quantities in the soil-mass oscillator experiments are the magnitudes of mass loading, mass of the soil column, and acoustic drive amplitude. Varying any of these parameters *ceteris paribus* enables one to study the nonlinear oscillator under different resonant conditions.

Steel Toroid: 6cm tall, 17.7 cm
outer diameter, 10.3 cm inner
diameter

Aluminum Plug: 5 cm tall, 9.5
cm diameter
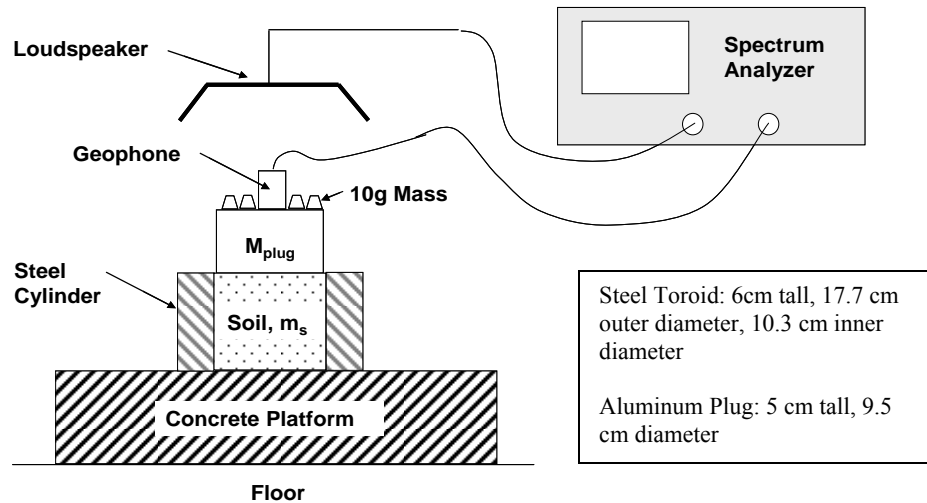
Figure 7 – Soil-mass oscillator schematic

2.1a. Soil Stiffness – 1-D Model

Controlled mass loading of the soil-mass oscillator allows the spring constant of the soil

to be experimentally determined. At low drive amplitudes, the linear system behaves as a driven

oscillator with damping, so according to Newton's second law

$$\sum F_x = -kx - b\dot{x} + F_{ext}\cos\omega t = m\ddot{x}$$

Equation 1

where $-kx$ is a linear restoring force, $-b\dot{x}$ is a damping force, and $F_{ext}\cos\omega t$ is an externally

applied driving force. This yields the following equation of motion for the system,

$$m\ddot{x} + b\dot{x} + kx = F_{ext}\cos\omega t$$

Equation 2

The homogenous solution for the damped harmonic oscillator is

$$x(t) = Ae^{-\alpha t}\cos(\omega_{res}t + \beta)$$

Equation 3

where

$$\omega_{res} = \sqrt{\omega_0^2 - \alpha^2}$$

$$\alpha = \frac{b}{2m}$$

$$\omega_0 = \sqrt{\frac{k}{m}}$$

<div align="right">**Equation 4**</div>

and A and β are determined by initial conditions. The particular solution to the equation of motion is given as

$$x(t) = \frac{F_{ext}\sin(\omega t - \phi)}{\omega\sqrt{b^2 + \left(\omega m - \frac{k}{\omega}\right)^2}}$$

<div align="right">**Equation 5**</div>

$$\phi = \tan^{-1}\left(\frac{\omega m - \frac{k}{\omega}}{b}\right)$$

<div align="right">**Equation 6**</div>

In the case of weak or negligible damping, the solution simplifies to

$$x(t) = \frac{F_{ext}\cos\omega t}{\omega^2 m - k}$$

<div align="right">**Equation 7**</div>

Under experimental conditions, if the driving force is also relatively weak then the spring constant for the weakly damped, weakly driven harmonic oscillator is shown to be

$$k = m\omega^2$$

<div align="right">**Equation 8**</div>

From Equation 8, it is now possible to calculate the effective spring constant of the soil. Tuning curves of soil surface velocity versus frequency are collected as precise mass weights are

added to the system for an invariant drive amplitude. For each 10 gram mass that is added, the system softens and the effective mass becomes

$$m_{eff} = M_{plug} + \frac{1}{3}m_{soil} + m_{weights}$$

Equation 9

The mass of the soil is approximated as the mass of a linear spring oscillating with a fixed mass on one end.[9] When Equation 8 is inserted into Equation 9, the relationship for determining the spring constant becomes

$$k_{eff} = \left(M_{plug} + \frac{1}{3}m_{soil} + m_{weights} \right)\omega_0{}^2$$

Equation 10

That is, the square of the natural resonant angular frequency is inversely proportional to the effective mass, where the constant of proportionality is k_{eff}.

For a typical data run, the Agilent spectrum analyzer operates in the swept sinusoidal mode. The acoustic drive amplitude is kept at a low, or "infinitesimal" amplitude so that the tuning curve behavior is kept as close to the linear regime as possible. Larger, or "finite," amplitudes could detune the system and produce an unwanted shift in the resonant peak to slightly lower frequencies as the effective spring constant "softens." A plot of Equation 10 for each resonant peak produces Figure 8. For this particular example using (673.3 ± 0.1) grams of dry, sifted masonry sand, the spring constant is computed from a regression analysis to be

$$k_{eff} = (4.4 \pm 0.1) \times 10^6 \frac{N}{m}.$$
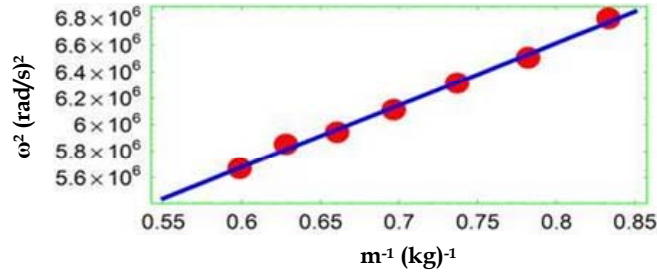
Figure 8 – Linear regression of ω^2 versus m^{-1} used to determine the effective stiffness of the Soil-Mass Oscillator.

From linear acoustic theory it is known that the longitudinal velocity of sound, c, propagating through a medium is[10]

$$c = \sqrt{\frac{Y}{\rho}}$$

<div align="right">**Equation 11**</div>

where ρ is the density of the medium and Y is its Young's, or elastic, modulus. Young's modulus is defined as stress over strain, so for the case of longitudinal compression or expansion of magnitude ΔL,

$$Y \equiv \frac{\sigma}{\varepsilon} = \frac{F/A}{\Delta L/L_0} = \frac{k(\Delta L)L_0}{A(\Delta L)} = \frac{kL_0}{A}$$

<div align="right">**Equation 12**</div>

Here, L_0 is the equilibrium length and A is the cross sectional area of the effective column through which the sound is propagating. Substituting Equation 12 into Equation 11, the expression for the sound speed in a medium is equal to

$$c = \sqrt{\frac{kL_0}{\rho A}}$$

<div align="right">**Equation 13**</div>

For the data in Figure 8, the sound speed in the soil $\left(T = 20^\circ C\right)$ is (149 ± 1) m/s.

Algebraic manipulation of Equation 13 also provides a method to verify the value of k found from the regression analysis above.

$$k = \frac{\rho c^2 A}{L_0}$$

<div align="right">**Equation 14**</div>

2.1b. Nonlinear Observations from Acoustic-to-Seismic (A/S) Coupling Experiments

To this point, the soil has only been studied in a linear context. Acoustic-to-seismic (A/S) coupling techniques provide a manner in which to begin examining the nonlinear elastic properties of the soil. In A/S experiments, a specimen is subjected to driving acoustic pressures of varying amplitude and the relative shift in frequency is observed. Tuning curves (plots of the amplitude of the resonant response versus frequency) are generated for various sound pressure levels. The acoustic drive level remains constant throughout the duration of a sweep but is uniformly incremented between successive sweeps.

In Figure 9, tuning curves are shown for frequency sweeps conducted in the 325 to 375 Hz bandwidth. The collection of tuning curves shows a clear decrease in peak resonant frequency as acoustic excitation increases. This shift is depicted by the locus of peak amplitudes for each tuning curve, also referred to as a backbone curve, and is indicative of softening of the soil's effective spring constant. Each of the additional ten tuning curve families collected from the soil mass oscillator (displayed in Appendix C) have a linear backbone curve, suggesting that the nonlinear behavior of the soil is mesoscopic elastic in nature.
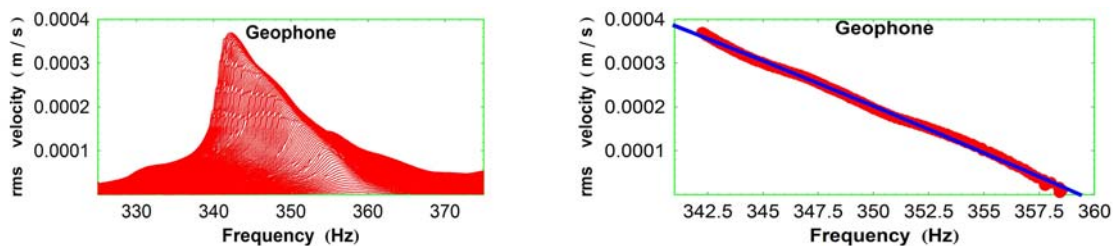
Figure 9 – Nonlinear tuning curves and linear backbone curve from the soil-mass oscillator using dry, sifted masonry sand.

2.1c. Mesoscopic Elastic Behavior

A mesoscopic description of the physical world, which lies between the macroscopic and microscopic levels, is needed in order to understand and explain the elasticity of granular media. Whereas classical nonlinearity results from the microscopic stress-strain response of each individual grain of sand (see Figure 10), mesoscopic nonlinearity, sometimes referred to as nonclassical nonlinearity, arises from the interaction of a small aggregate of grains with their immediate neighbors. In the mesoscopic model, nonlinearity results from a "stick-slip" mechanism. When initially stressed the points of contact between grains bind, or "stick" together. As stress continues to build a yield point is reached and the grains suddenly "slip" (see Figure 11). This "slip-stick" type nonlinearity is the primary cause for the mesoscopic elastic behavior observed in the soil-mine system.
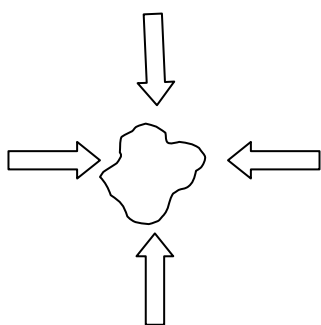
Figure 10 – Classical nonlinearity. On the microscopic scale, each single grain of sand exhibits a strain response when subjected to an external stress.
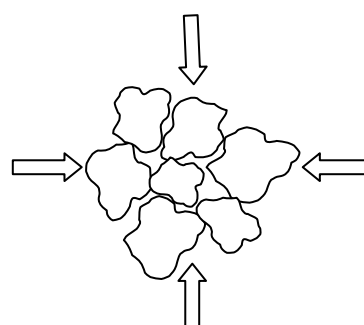
Figure 11 – Mesoscopic nonlinearity. On the mesoscopic scale, individual grains interact with neighboring grains. The points of contact between grains cause a "stick-slip" strain response when stressed.

2.1d. The Iwan Model of One-Dimensional Forced Oscillations with Hysteresis

The stick-slip nature of mesoscopic nonlinear media creates another observable nonlinear effect called hysteresis. Hysteretic systems are not only state dependent but also history dependent. That is, in order to properly describe a hysteretic system it is not sufficient to know only its current condition, but also how it arrived at that present condition. As grains of soil continuously stick and slip the soil lattice structure is altered.   The macroscopic effect of these fluctuations is a change in the net lattice yield force of the system, measurements of which serve as a quantifiable measure of the degree of nonlinearity in a system.

Iwan[11] presents a hysteretic model based upon series-parallel construct of elasto-slip elements. As shown in Figure 12, the hysteretic system is a parallel network of "slip-stick" spring components known as Jenkin's elements. Each spring is linear and each slip damper has a maximum allowable force $\dfrac{f_i}{N}$, which is different for each of the N elements in the model.   If the maximum allowable force of any particular element is exceeded, the element in question will yield and its spring constant will no longer contribute to the elastic behavior of the macroscopic system. The force-deflection response for a single Jenkin's element is shown in Figure 13.
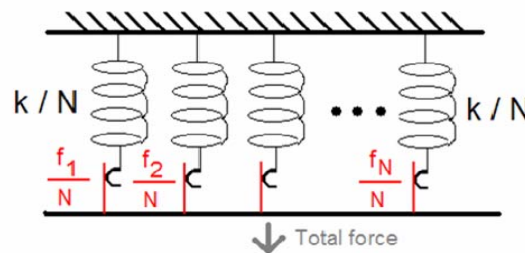
Figure 12 – Combined model of elasto-slip hysteresis
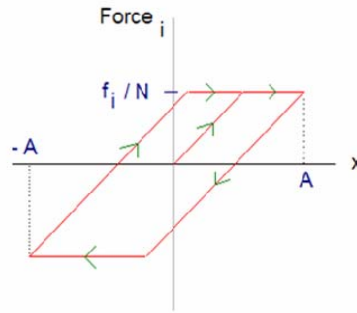
Figure 13 – Force-deflection diagram for one element in the elasto-slip model

The lattice yield force is a stress threshold above which the specimen is no longer in the linear elastic region of deformation. If a sample is stressed beyond its lattice yield point, it will not return to its prestressed condition simply by removing the external stress. Thus, the stress-strain diagram will form a hysteretic loop as seen in Figure 14.
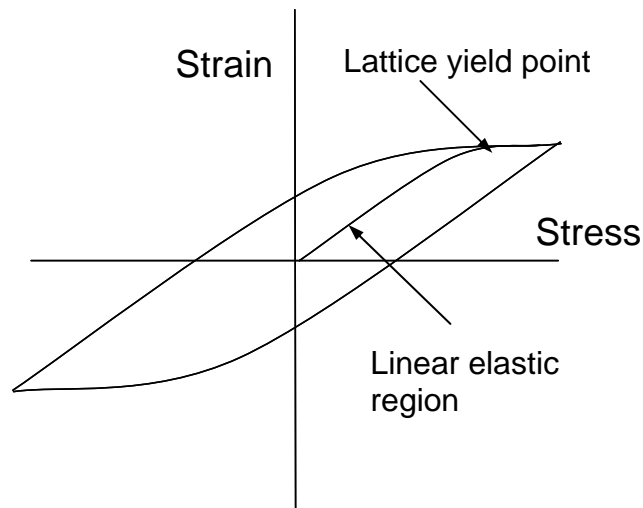
Figure 14 – Hysteresis loop created by exceeding the yield force of a system

The actual force at which each element slips varies, but according to Iwan's model the yield forces are distributed equally about a mean value, F_y. If the distribution function, φ, is a band-limited function with width Δf and normalized area, the following parameters can be defined:

$$\beta = \frac{\Delta f}{2F_y}$$

Equation 15

$$Q \equiv \frac{kA}{F_y}$$

<div align="right">**Equation 16**</div>

Here, β is a dimensionless parameter that defines the bandwidth of the "flat" distribution

function centered about F_y. For the case when $\beta \to 0$, the distribution has infinitesimal width.

That is, all the constituent Jenkin's elements have identical yield forces. As $\beta \to 1$, the

bandwidth of the distribution becomes infinitely large. k is once again the spring constant and A

is the deflection amplitude of the stressed system, which makes Q the maximum dimensionless

amplitude of deflection. Hysteresis loops for different values of β are shown in Figure 15.

<div align="center">

β = 0 β = 0.5 β = 1

</div>
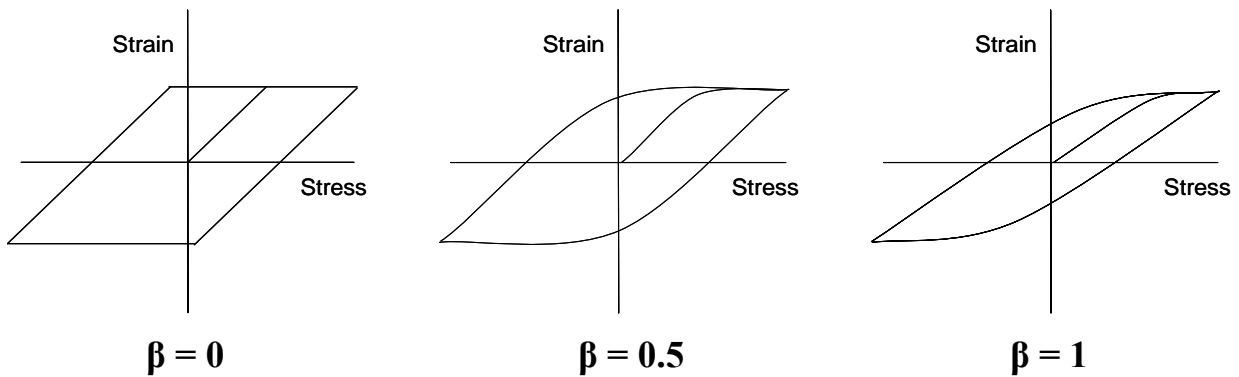
Figure 15 – Hysteresis loops for varying distribution functions, φ, defined by β

In Iwan's elasto-slip model of hysteresis, the equation of motion is

$$m\ddot{x} + f(x,\dot{x}) = F \cos \omega t$$

<div align="right">**Equation 17**</div>

where the function f accounts for hysteretic contributions. Using the method of equivalent

linearization,[7] the nonlinear term in Equation 17, $f(x,\dot{x})$, is replaced by an equivalent linear

restoring force, $\gamma\dot{x} + \kappa x$, and an error term $\varepsilon(x,\dot{x})$. That is

$$m\ddot{x} + \gamma\dot{x} + \kappa x + \varepsilon(x,\dot{x}) = F \cos \omega t$$

<div align="right">**Equation 18**</div>

Here, κ and γ are parameters dependent upon both amplitude and β. In order for the

substitution above to be valid, the error term must be minimized. In other words,

$$\frac{\partial \overline{[\varepsilon(x,\dot{x})]^2}}{\partial \gamma} = 0$$

Equation 19

$$\frac{\partial \overline{[\varepsilon(x,\dot{x})]^2}}{\partial \kappa} = 0$$

Equation 20

After the minimization is performed, the equation of motion becomes

$$m\ddot{x} + \gamma\dot{x} + \kappa x = F\cos\omega t$$

Equation 21

whose solution is assumed to be

$$x = A\cos\theta$$

Equation 22

where

$$\theta = \omega t - \psi$$

Equation 23

Here, A is the maximum amplitude of the vibration and ψ is the phase of the motion. The

equation for a tuning curve according to this model is given by

$$m\omega^2 = \frac{C(A)}{A} \pm \left\{ \left(\frac{F}{A}\right)^2 - \left[\frac{S(A)}{A}\right]^2 \right\}^{\frac{1}{2}}$$

Equation 24

where

$$C(A) = \frac{k}{A} = \frac{1}{\pi}\int_0^{2\pi} F(A,\theta)\cos\theta\, d\theta$$

Equation 25

$$S(A) = \frac{-\gamma}{A\omega} = \frac{1}{\pi}\int_0^{2\pi} F(A,\theta)\sin\theta\, d\theta$$

Equation 26

In order to make Equation 24 dimensionless, the following substitutions are made,

$$\eta = \frac{\omega}{\sqrt{k/m}}$$

$$r = \frac{F}{F_y}$$

$$C(Q) = \frac{C(A)}{F_y}$$

$$S(Q) = \frac{S(A)}{F_y}$$

Equation 27

The dimensionless form of a tuning curve is then

$$\eta^2 = \frac{C(Q)}{Q} \pm \left\{ \left(\frac{r}{Q}\right)^2 - \left[\frac{S(Q)}{Q}\right]^2 \right\}^{1/2}$$

Equation 28

though the backbone curve is simply

$$\eta^2 = \frac{C(Q)}{Q}$$

Equation 29

Here, the backbone curve is defined as the locus of normalized maximum amplitude responses obtained from each of the resonant tuning curves.

In order to determine the yield force of the masonry sand used in the soil-mass oscillator, a distribution function must first be selected. In other words, a value for β must be chosen.

Peak Response Amplitude vs Resonant Frequency
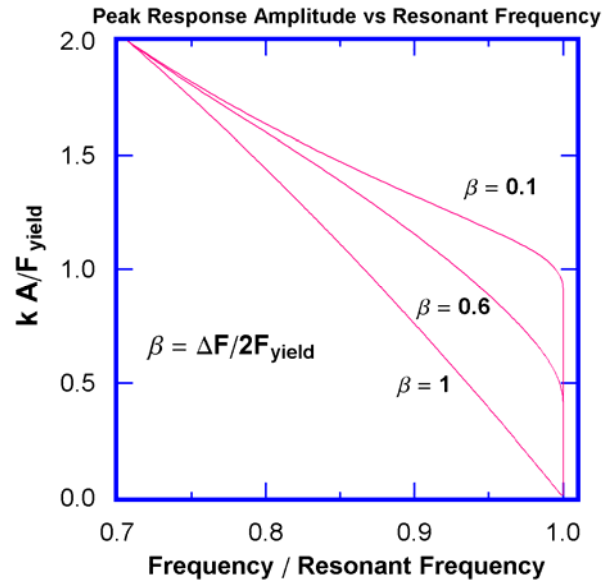
Figure 16 – Backbone curves from the Iwan model for various values of β.

Response Amplitude vs Frequency
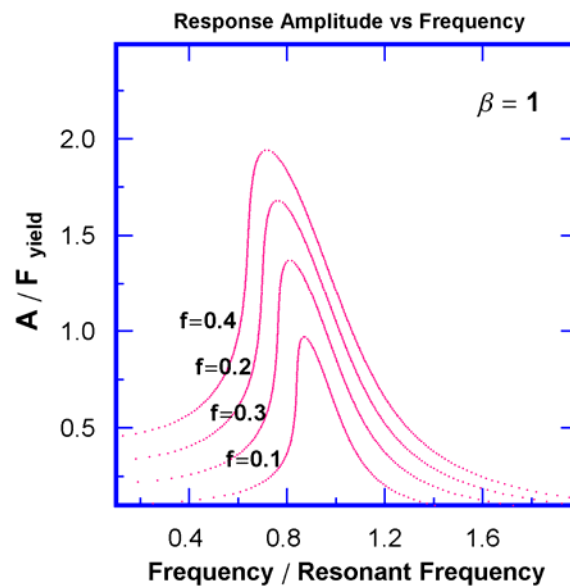
Figure 17 – Tuning curves predicted by the Iwan model for the case β=1.

Plots of backbone curves for various values of β are shown in Figure 16. Empirical

observations from the soil-mass oscillator correspond most closely to the case for $\beta = 1$. Sample

tuning curves predicted by the Iwan model for $\beta = 1$ are depicted in Figure 17. Under this

condition,

$$\eta \equiv \frac{\omega}{\omega_0}$$

Equation 30

$$C(Q) \equiv Q - \frac{Q^2}{4}$$

Equation 31

Substitution of Equation 30 and Equation 31 into Equation 29 provides

$$\left(\frac{\omega}{\omega_0}\right) = \left(1 - \frac{Q}{4}\right)^{\frac{1}{2}}$$

Equation 32

A binomial expansion for $Q \ll 1$ produces the relationship

$$\frac{f - f_0}{f_0} = -\frac{Q}{8} = \frac{-kA}{8F_y}$$

Equation 33

The spring constant, k, is determined from the mass loading experiment shown in Equation 10 and Figure 8. The yield force, F_y, is obtained from one of the tuning curve data sets and its corresponding backbone curve, such as that shown in Figure 9. However, the recorded data from the spectrum analyzer is in terms of velocity and not amplitude, as required by Equation 33. Velocity, u, is related to amplitude, A, in the following manner

$$A = \frac{|u|}{2\pi \langle f \rangle}$$

Equation 34

where $\langle f \rangle$ is the average frequency across a narrow bandwidth of the swept sinusoid. Substituting into Equation 33, the relationship becomes

$$\frac{f - f_0}{f_0} = \frac{-k}{8F_y}\left(\frac{|u|}{2\pi \langle f \rangle}\right)$$

Equation 35

This shows that a plot of particle velocity versus frequency will have

$$slope = \frac{2\pi\langle f\rangle}{f_0}\left(\frac{-8F_y}{k}\right)$$

<div align="right">**Equation 36**</div>

The yield force is

$$F_y = -\frac{(slope)kf_0}{16\pi\langle f\rangle}$$

<div align="right">**Equation 37**</div>

The linear regression of sound speed versus frequency for the data in Figure 9 is u = (7.56 ± 0.04) mm/s – (21.0 ± 0.1) μm*f. The spring constant is, $k = (6.1 \pm 0.1)$ x $10^6 \frac{N}{m}$. The yield force is, $F_y = (2.6 \pm 0.4)$ N.

The elastic modulus of the dry, sifted, "homogenous" soil is affected by its pre-stressed state, so that the initial conditions of every trial run are unique. As a result, the quantitative measure of nonlinearity will not be identical from trial to trial. Soil is affected by environmental conditions such as temperature, atmospheric pressure, and moisture content. Nevertheless, though it is not intentionally controlled, the laboratory environment throughout the duration of these experiments remained fairly consistent at 20° C. Results obtained from the soil-mass oscillator tend to be relatively repeatable. The average yield force for eleven trials using dry, sifted masonry sand is 2.9 N with a standard deviation of 0.4 N.

2.1e. Soil Comparison

It is expected that different soils exhibit different degrees of nonlinearity. This might be due in part to porosity as well as grain size and shape. Figure 18 shows the increasing drive amplitude experiment for the soil-mass oscillator using a dry, sifted, Mississippi loess soil rather than masonry sand. Loess soil is a much finer silt-like soil than masonry sand. Here, the slope of the backbone curve is steeper than in the case of masonry sand. Qualitatively, however, it

exhibits the same linear backbone curve indicative of mesoscopic elastic behavior. Using the

same technique as described for the masonry sand above, the yield force for the loess soil is

determined to be (5.9 ± 0.3) N.

| $u = (21 \pm 1)$ mm/s $- (63 \pm 3)$ μm $*f$ | $k = (4.7 \pm 0.1)$ MN/m | $F_y = (5.9 \pm 0.3)$ N |
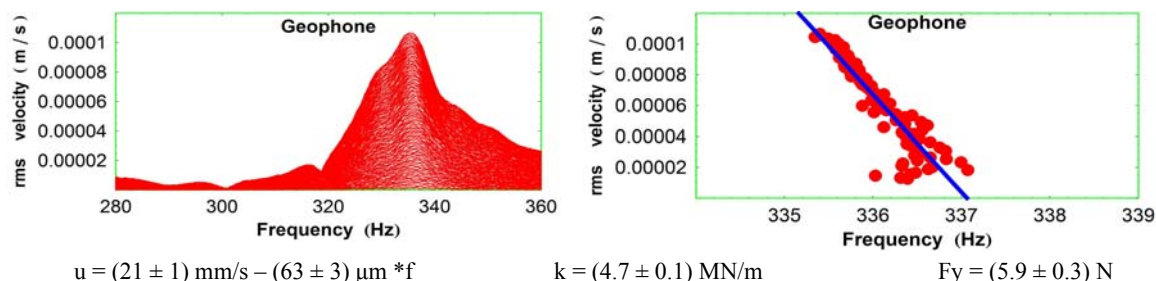
Figure 18 – Nonlinear tuning curves and linear backbone curve from the soil-mass oscillator using dry, sifted loess soil.

2.1f. Local Interaction Simulation Approach (LISA) Modeling

The elasto-slip model developed in 1966 by Iwan is not the only model available to

describe the nonclassical nonlinearity apparent in the soil-mass oscillator, and the LISA method

proposed by Scalerandi *et al*[6] certainly provides an alternative, more modern approach.

However, while extremely advantageous for lending physical intuition to the complex soil

system, it also has certain limitations which arise from its purely phenomenological nature.

The primary advantage of the LISA model lies in its ability to provide a conceptual

framework in which to envision the nonlinearity of the soil. For the sake of simplicity, only a

one-dimensional lattice is considered herein. Each grain and interstice form a single

subcomponent, referred to as a G-B unit or hysteretic elastic unit (HEU). A sample 1-D lattice is

shown in Figure 19. Each grain is considered to be entirely elastic, and the interstices obey a

"slip-stick" mechanism loosely similar to that proposed by Iwan. The overall behavior of a HEU

is governed by the combined behavior of its constituent grain and interstice. It is this aggregate

effect that is nonclassically nonlinear.

Each interstice has a specific yield force at which it changes from linear elastic to inelastic. From a physical standpoint, the compressive elastic properties of the interstice can be thought of in terms of "squeezing" a fluid from the interstice. Conversely, the tensile elastic properties of an interstice can be envisioned as the suction effect between two grains that are being pulled apart. For mathematical simplicity, however, the LISA model views each interstice as a small vacuum. That is to say, the mathematical complications caused by the fluid dynamics of air or water in interstice regions are not addressed mathematically.
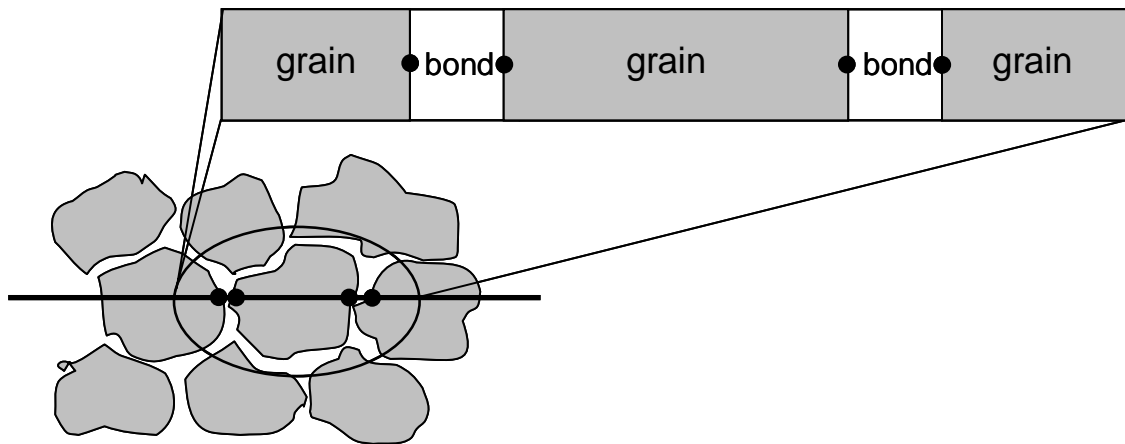

Figure 19 – Sample 1-D soil lattice depicting grain-bond-grain units

In the 1-D case, the grains and interstices are subject solely to longitudinal compression and tension. The constituent equation of state for each HEU is given as

$$\sigma = E\varepsilon + \eta\dot{\varepsilon} + \chi P_T$$

Equation 38

$\sigma = $ stress = force per area

$E = $ Young's (elastic) modulus

$\varepsilon = $ strain = elongation per equilibrium length of HEU

$\eta = $ viscosity coefficient

$$\dot{\varepsilon} = \text{strain time-rate of change}$$

$$\chi = \text{poroelastic threshold parameter}$$

$$P_T = \text{poroelastic pressure}$$

The LISA model assumes that every HEU obeys the same equation of state, but allows each interstice to have different pressure threshold values. The distribution of threshold values for every HEU in a sample is presented graphically in a Preisach-Mayergoyz (PM) space. A sample distribution of 300 HEUs is generated by the author using Mathematica$^{®}$ and is shown in Figure 20. (The PM formalism is described in greater detail in Appendix D).
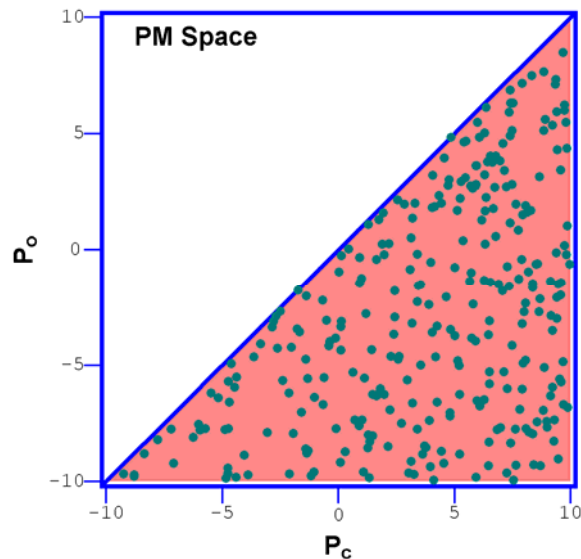

Figure 20 – Sample Preisach-Mayergoyz distribution of pressure thresholds for the HEU in a soil sample

In brief, each point in the PM-space distribution corresponds to a single HEU having a unique bi-state protocol as shown in Figure 21. As the acoustic pressure, P, changes, an interstice can shift from an open state, C_2, to a closed state, C_1, or vice versa. However, a "closing" will only occur if the pressure exceeds the closing pressure threshold, P_c, whereas an "opening" only results if the pressure drops below the opening pressure threshold, P_o.
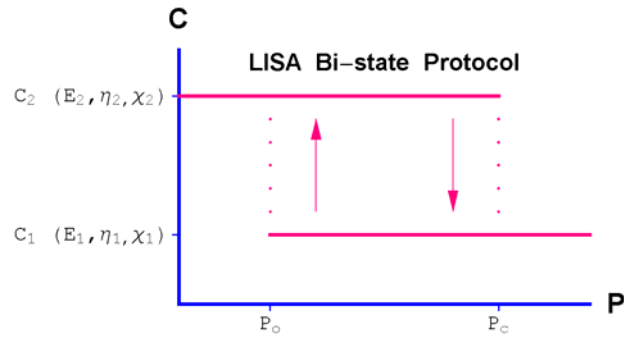
Figure 21 – Bi-state protocol for the LISA model. Each state is a function of three elastic parameters.

Each HEU is itself hysteretic, and the overall hysteretic behavior observed in the system is the aggregate contribution of all the elements. For example, a PM-space containing only two HEUs is shown in Figure 22. The corresponding stress-strain hysteresis loop that results from each HEU as the pressure field oscillates between -10 and 10 Pa is shown in Figure 23.
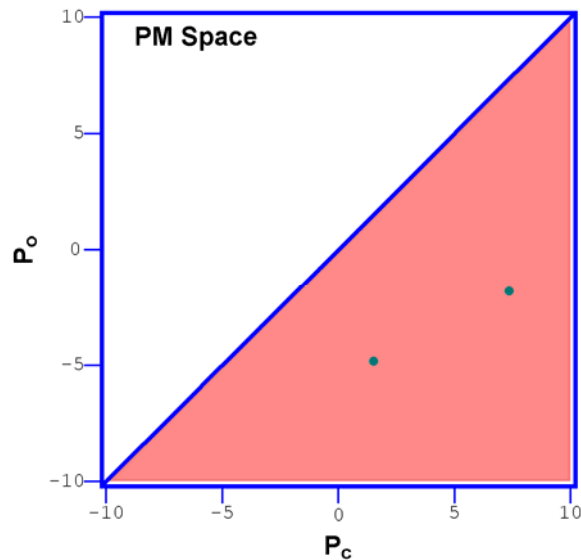

**Figure 22 – PM-space distribution of only two HEUs**
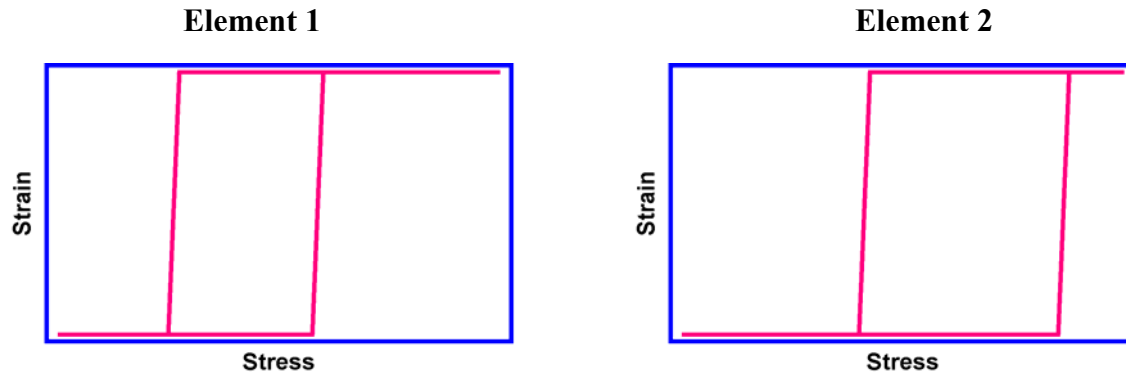
Element 1   **Element 2**

Figure 23 – Hysteretic contributions of individual elements in a PM-space distribution.

Superposition of the hysteretic contributions of elements one and two produces the overall

hysteresis loop for the two-element system that is seen in Figure 24. As the number of HEUs in

the system increases, the PM-space is more heavily populated and the overall hysteresis loop

becomes increasingly smoother. Examples of PM-space distributions having 50 and 300

elements and the corresponding hysteresis loops are shown in Figure 25 and Figure 26,

respectively.
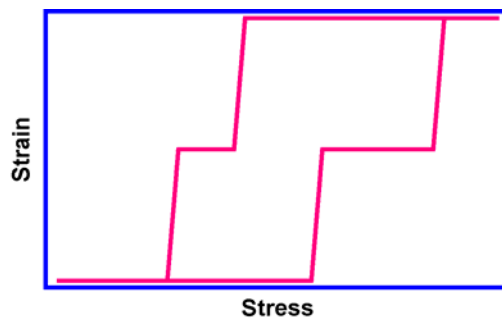
**Figure 24 – Overall hysteretic behavior of a two-element system.**
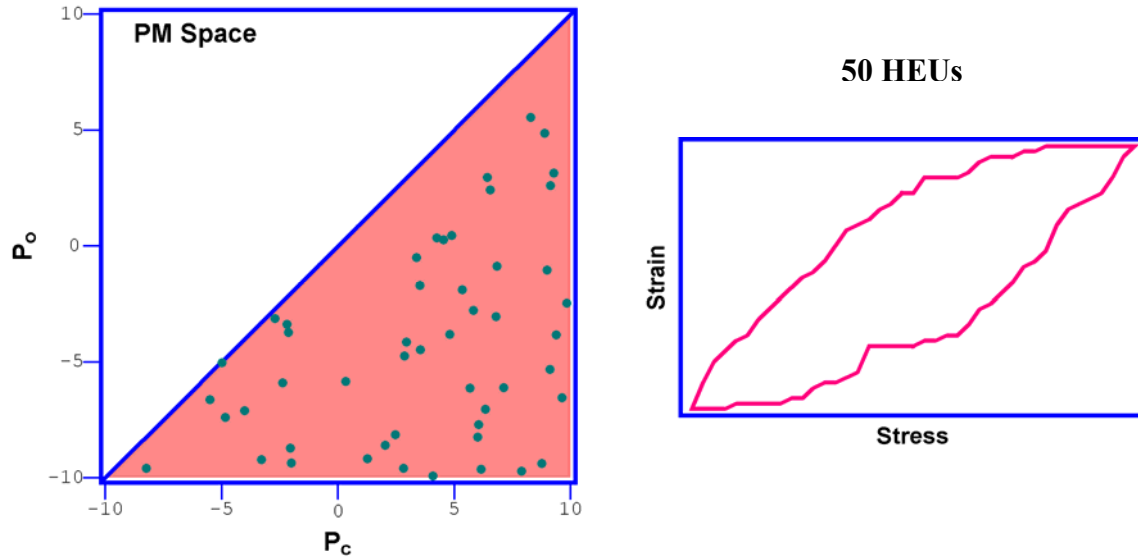
Figure 25 – PM-space distribution containing 50 HEUs and the corresponding hysteresis loop.
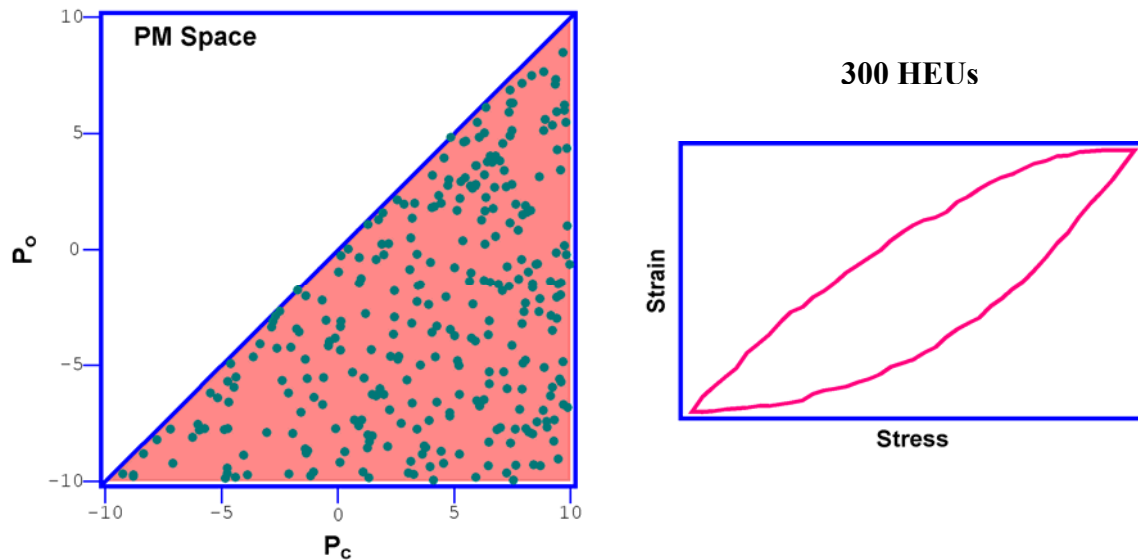

Figure 26 – PM-space distribution containing 300 HEUs and the corresponding hysteresis loop.

For a system with a large number of hysteretic elements, as in Figure 26, the phenomenological hysteresis loop behavior mirrors that predicted by Iwan (Figure 14). In fact, the shape of this hysteresis loop predicts tuning curve behavior with a linear backbone. Though additional numerical efforts beyond the scope of this project are required in order to generate

such tuning curves, the evident shared behavior with the Iwan model provides incredibly strong justification for the use of the LISA approach in modeling the buried landmine system.

While LISA is a tremendously promising model, it has certain aspects that must be further refined in order to make it useful in a predictive sense. From Equation 38 and Figure 21 it is clear that each of the two possible states in the bi-state protocol is dependent upon the three parameters E, η, and χ. However, the connection between these parameters and the microscopic physical world is not yet well understood. The model itself is "reverse engineered" from macroscopic observations of nonlinearity and not yet connected to the actual microscopic regime of individual grains. In other words, though the parameters E, η, and χ seem to be measurable microscopic quantities, as of yet there exists no conclusive experimental verification as to the role each plays in determining the observed overall nonclassical nonlinear behavior. Efforts are underway by Darling and TenCate to further develop the understanding between the aforementioned elastic parameters and physical microscopic reality using neutron diffraction techniques.[12]

An additional difficulty of the LISA model is that the PM space, in order to properly fit experimental results, depends heavily upon complicated adjustable parameters that are not well understood. In and of itself, the PM approach is not flawed. In fact, the statistical complexity of the distribution function as well as the probabilistic treatment of thermally induced state transitions makes it considerably more versatile than the band-limited function employed by Iwan. However, the PM distributions used in the LISA modeling done by Scalerandi *et al* were entirely arbitrary and disconnected from physical experimental specimens. Though every geospecimen possesses its own footprint in PM space, actually generating this PM space is a very demanding mathematical problem.

2.2 Soil Plate Oscillator

Moving beyond the nonlinearity which results from just soil alone, the soil-plate oscillator apparatus enables the study of the nonlinear interaction that occurs at the soil-mine interface. The soil-plate apparatus cuts away many of the additional complexities inherent in a real landmine and isolates the soil-elastic plate boundary.

This analysis begins with an examination of the vibration of a clamped plate, and then continues on to look at the coupled soil-plate system. As seen in Figure 27, an acrylic plate simulating the elastic top plate of a landmine is securely clamped between two aluminum flanges. As in the case of the soil-mass oscillator (Section 2.1), the Agilent spectrum analyzer provides a swept sine signal, which is amplified to drive a pair of three-inch diameter loudspeakers. The loudspeakers, in turn, generate an acoustic pressure wave that excites the system. An accelerometer affixed to the underside of the plate measures the vibration response of the plate. If the plate is loaded with a column of soil, a second accelerometer is placed atop the column to measure the response of the combined soil-plate system. As before, measurement data is recorded by the spectrum analyzer in dual channel operation. (Further descriptions of experimentally used equipment are given in Appendix A.)
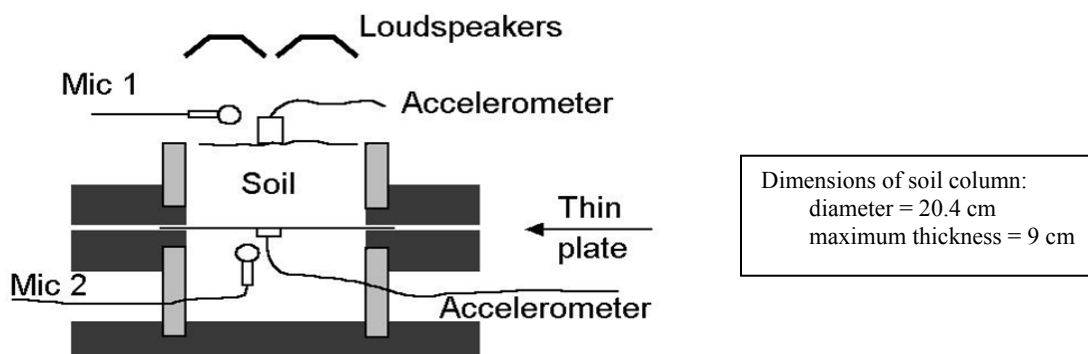

Figure 27 – Schematic of soil-plate oscillator with loudspeaker

2.2a. Vibrations of an Elastic Clamped Plate in the Absence of Soil Loading

In order to understand the coupled soil-plate oscillator model, one must first begin with a discussion of clamped plate vibrations independent of soil loading. The individual particles within the plate obey a two-dimensional equation of motion whose solution satisfies the wave equation. A thorough development and derivation of this idea is included in Appendix E. For the case of vibration with azimuthal symmetry, the displacement of particles at any radial location, $w(r)$, on a clamped plate is given by

$$w(r) = \frac{P}{\rho d \omega^2} \left[\frac{J_0(kr)I_1(ka) + I_0(kr)J_1(ka)}{J_0(ka)I_1(ka) + I_0(ka)J_1(ka)} - 1 \right]$$

Equation 39

where the wave number k is defined as follows

$$k = \left(\frac{12 \rho \omega^2 (1 - \sigma^2)}{E d^2} \right)^{1/4}$$

Equation 40

and the physical parameters of the plate are defined as

P = driving acoustic pressure

ρ = plate density

d = plate thickness

ω = natural resonant frequency of the clamped plate

a = clamped radius

σ = Poisson's ratio

E = Young's (elastic) modulus

The theoretical prediction for the lowest resonant frequency of vibration of the plate is given by $ka = 3.20$. Using Equation 40 one can show that

$$\omega_{res} = \frac{(3.20)^2 c_{long} d}{a^2 \sqrt{12(1 - \sigma^2)}}$$

Equation 41

where $c_{long} = \sqrt{E/\rho}$ and $f_{res} = \dfrac{\omega_{res}}{2\pi}$. σ is taken to be 1/3 as Poisson's ratio for the acrylic plate.

Then, given $f_{res} = 286$ Hz, $d = 3.2$ mm, and $a = 10.2$ cm, one can characterize the acoustic

properties of the plate material in terms of its longitudinal bar speed, c_{long}, which is computed to

be 19,000 m/s.

It is important to note that Equation 39 is the exact solution to a linearized wave equation

for the elastic plate. Similarly, the magnitude of the transverse velocity and acceleration of a

clamped plate are given by $\omega w(r)$ and $\omega^2 w(r)$, respectively. Experimental measurements of an

unloaded clamped plate exhibit a slight stiffening of the plate at relatively large amplitudes of

vibration. This leads to a small increase in the resonant frequency as drive amplitude increases as

shown in Figure 28.
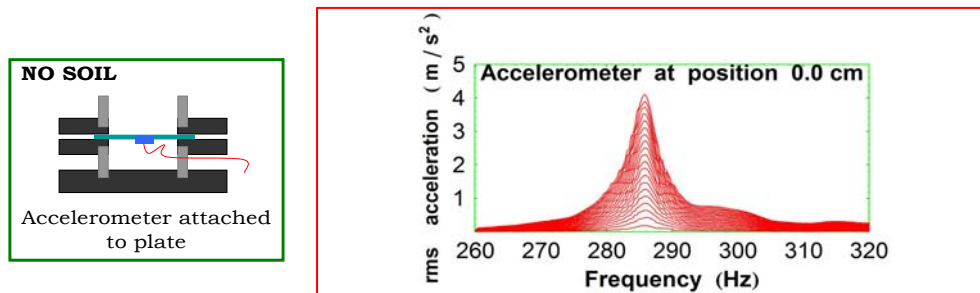
Figure 28 – Tuning curves of rms acceleration versus frequency for an unloaded clamped plate exhibiting a slight deviation from linear behavior.

2.2b. Comparison of the Soil-Mass Oscillator, Soil-Plate Oscillator, Buried Mine Simulant, and VS 1.6 Nonlinearities

As previously mentioned, soil is an inherently nonlinear medium. Therefore, it is

expected that a coupled soil-plate system will depart from the linear behavior observed in the

case of the unloaded clamped plate. It is important to quantify and compare the overall

nonlinearity of a system due to soil oscillations over a flexible plate with the soil oscillations

over a rigid boundary.

Figure 29 shows the soil-plate oscillator apparatus instrumented with a 1" thick aluminum plate (6" diameter), which is considered to be fairly rigid. The clamped aluminum plate is loaded with a 4 5/8" diameter soil column. The family of tuning curves and corresponding backbone curve obtained from the soil-plate oscillator when instrumented with the mass-loaded thick aluminum plate are shown in Figure 29.
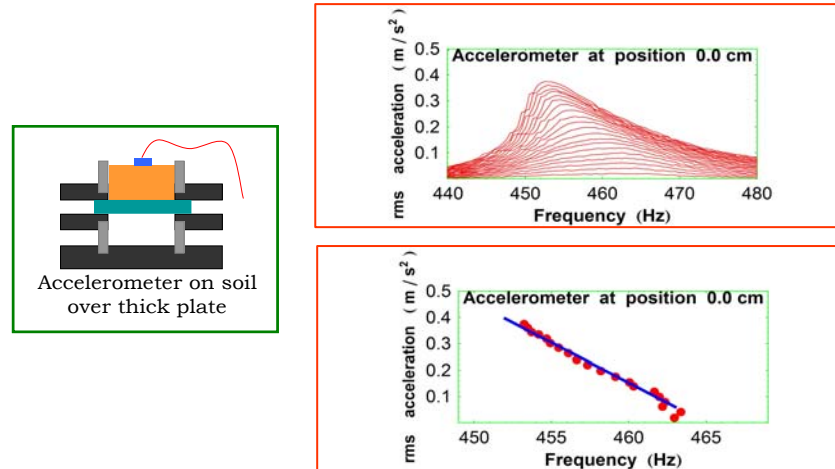

Figure 29 – Tuning curves and backbone curve from the soil-plate oscillator when instrumented with a thick, rigid aluminum plate and loaded with a 1" thick soil layer.

The slope of the backbone curve is a measure of the nonlinearity present in the system. The backbone curve (the locus of peak accelerations versus corresponding resonant frequency) is fit to a linear function such that

$$acceleration = \beta\left(\frac{f - f_0}{f_0}\right) + \alpha$$

Equation 42

where f_0 is the natural resonant frequency of the system when subjected to an external driving force of infinitesimal amplitude. A parameter of nonlinearity, β^{-1}, suitable to describe the detuning or softening is computed from a regression analysis so that

$$\beta^{-1} \equiv \frac{1}{(slope)f_0}$$

Equation 43

The results from Figure 29 show that the parameter of nonlinearity of soil alone is $\beta^{-1} = 0.070$ m/s^2.

When the relatively rigid, thick aluminum plate supporting the soil column is replaced by a flexible, 1/8" thick acrylic plate (6" diameter), the parameter of nonlinearity in the coupled soil-plate system is found to increase considerably. The tuning curve results from this experiment are shown in Figure 30. Here, β^{-1} is found to equal 0.128 m/s^2. The same masonry sand used earlier is now placed back in the SPO such that the soil column remains effectively unchanged from the rigid plate case. It must be concluded that the additional nonlinearity observed arises from some facet of the combined soil-plate system. The hypothesis that the interaction which occurs at the interface between the soil and the plate must be nonlinear is strongly supported.
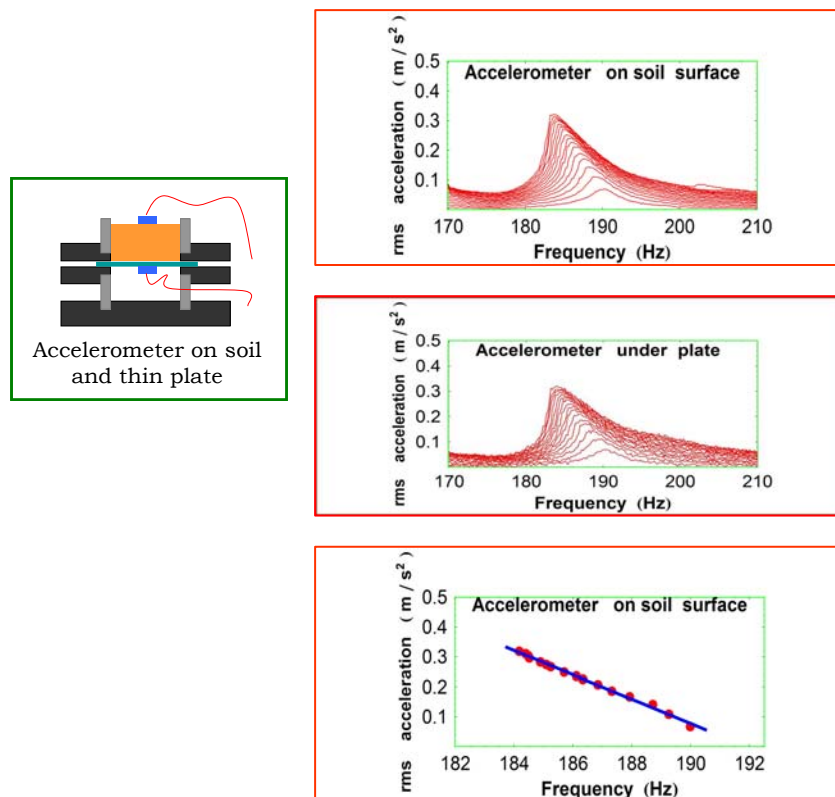
Figure 30 - Tuning curves and backbone curve from the soil-plate oscillator when instrumented with a thin, flexible acrylic plate and loaded with a 1" thick soil layer.

The nonlinearity of the soil-mass, soil-thick plate, and soil-thin plate systems are collected in Table 1.

Table 1 – Comparison of nonlinearity for the soil-mass, soil-thick plate, and soil-thin plate oscillators

Experiment	β^{-1}
soil-mass oscillator (loess soil)	0.022 m/s^2
soil-mass oscillator (masonry sand)	0.061 m/s^2
soil-thick plate oscillator (masonry sand)	0.070 m/s^2
soil-thin plate oscillator (masonry sand)	0.128 m/s^2

2.2c. Mesoscopic Elastic Behavior at Higher Amplitudes in the Soil-Plate Oscillator

At small drive amplitudes the soil-plate oscillator exhibits mesoscopic elastic behavior characterized by the presence of a linear backbone curve. However, the mesoscopic nonlinear model appears to break down at larger drive amplitudes. Experiments with masonry sand and the soil-plate oscillator are revisited using a modified soil-plate oscillator apparatus with a 0.030" thick clamped plate (8" diameter). The actual unclamped physical diameter of the plate is 8". This SPO is more compliant than the previous version which had a 0.090" thick plate (4 5/8" diameter). The results for the more compliant system are shown in Figure 31. The linear backbone behavior exists until the rms velocity nears 0.002 m/s. At this point there is a noticeable curvature to the backbone, indicating that what is happening is more complicated than just the mesoscopic nonlinear behavior of soil alone.
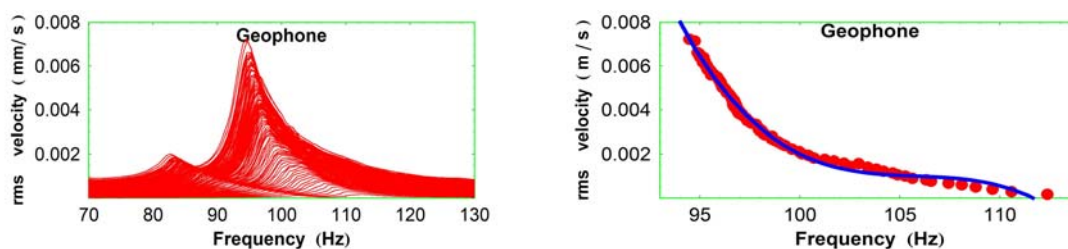
Figure 31 – Nonlinear tuning curves and nonlinear backbone curve from the soil-plate oscillator using dry, sifted masonry sand over a large range of drive amplitudes.

As a first approach to explaining this behavior, the elasto-slip theory of Iwan can be applied using a piecewise technique. There appear to be two relatively distinct linear regions above and below 100 Hz. In Figure 30 the plate is loaded with (392.6 ± 0.1) g of dry, sifted masonry sand, and, using Equation 37, the yield force is calculated for both regions. When f < 100 Hz, the analysis predicts that $F_y = 1.4N$. When f > 100 Hz, the yield force is predicted to be $F_y = 0.21N$

A second approach utilizes a model of bilinear hysteresis developed by Caughey.[7] Rather than envisioning a system of Jenkin's elements that only behave elastically up to a certain yield force (as with Iwan), the Caughey model can be imagined as a single spring whose elastic constant changes at a unique transition point. That is, if x_0 is the designated transition point for a particular spring-like element and A is the maximum amplitude of oscillation,

$F_{x_o^-} = -k_1 x, \quad 0 < x < x_0$ and $F_{x_o^+} = -k_2 x, \quad x_0 < x < A$, where $k_2 < k_1$. If $k_2 = 0$, the elastoplastic case of Iwan's model for the case where $\beta = 0$ is recovered. The force-deflection diagram for a single element in the bilinear hysteretic model is shown in Figure 32.
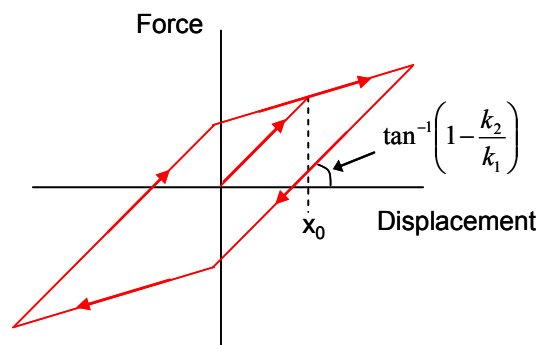
Figure 32 – Force-deflection diagram for a single bilinear-hysteretic element.

The equation of motion Caughey employs in his bilinear hysteresis model is

$$m\ddot{x} + kF(x, \mu, t) = P\cos\omega t$$

Equation 44

The $F(x,\mu,t)$ term is the hysteretic restoring force and simplifies to x in the case where μ goes to zero. Defining the following variables and making appropriate substitutions into Equation 44

$$\frac{k}{m} = \omega_0^2$$
$$\tau = \omega_0 t$$
$$\frac{P}{k} = x_s$$
$$\eta = \frac{\omega}{\omega_0}$$

Equation 45

the equation of motion can be rewritten as

$$\frac{d^2x}{d\tau^2} + F(x,\mu,\tau) = x_s \cos\eta\tau$$

Equation 46

In order to solve this second order nonlinear differential equation, Caughey uses a technique developed by Kryloff and Bogoliuboff[13] known as the method of slowly varying parameters where

$$x(\tau) = R\cos(\eta\tau + \phi)$$

Equation 47

$$(\eta\tau + \phi) = \theta$$

Equation 48

Here R and ϕ are defined to be the respective amplitude and relative phase in the oscillating response and are allowed to slowly vary in time. Equation 47 is differentiated twice and substituted into Equation 46. Caughey's analysis eventually leads to the following frequency response equation for the system

$$\eta^2 = \frac{C(R)}{R} \pm \left[\left(\frac{x_s}{R}\right)^2 - \left(\frac{S(R)}{R}\right)^2\right]^{\frac{1}{2}}$$

where

$$C(R) = \frac{1}{\pi}\int_0^{2\pi} F(R\cos\theta, \mu, t)\cos\theta \, d\theta$$

$$S(R) = \frac{1}{\pi}\int_0^{2\pi} F(R\cos\theta, \mu, t)\sin\theta \, d\theta$$

The maximum peak resonance is achieved at

$$\eta^2 = \frac{C(R)}{R}$$

which represents the backbone curve of the system. As the degree of bilinearity in the system increases, the curvature of the backbone becomes more pronounced. The measure of a systems bilinear nature is parameterized by the variable μ.

$$\mu = 1 - \frac{K_2}{K}$$

where K_1 and K_2 are the slopes of the force-displacement diagram before and after the yield point is reached, respectively. A plot of backbone curves for various values of μ is shown in Figure 33. For a fixed value of $\mu = 0.5$, a family of resonant tuning curves is pictured in Figure 34. Clearly, the Caughey model accurately replicates the curved behavior seen in the soil-plate oscillator.
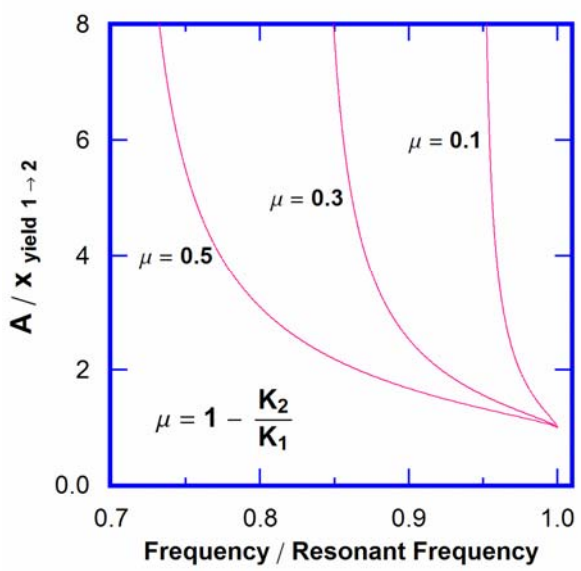
Figure 33 - Backbone curves from the Caughey model for various values of μ.
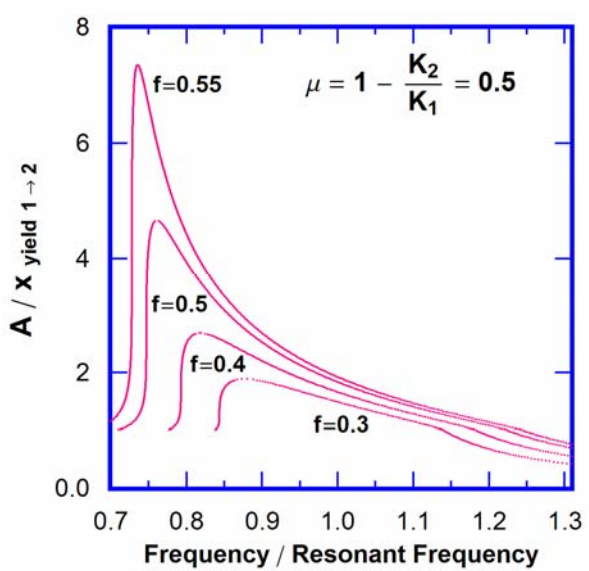
Figure 34 - Tuning curves predicted by the Iwan model for the case $\mu = 0.5$

To reiterate this last point, an experimental data set of resonant tuning curves is taken from the soil-mine simulant apparatus (Section 2.4). The buried simulant has a very thin, flexible plate much like the soil-plate oscillator. A normalized tuning curve, theoretically predicted curve ($\mu = 0.44$ and f = 0.42), and overlay of the two curves is shown in Figure 35.
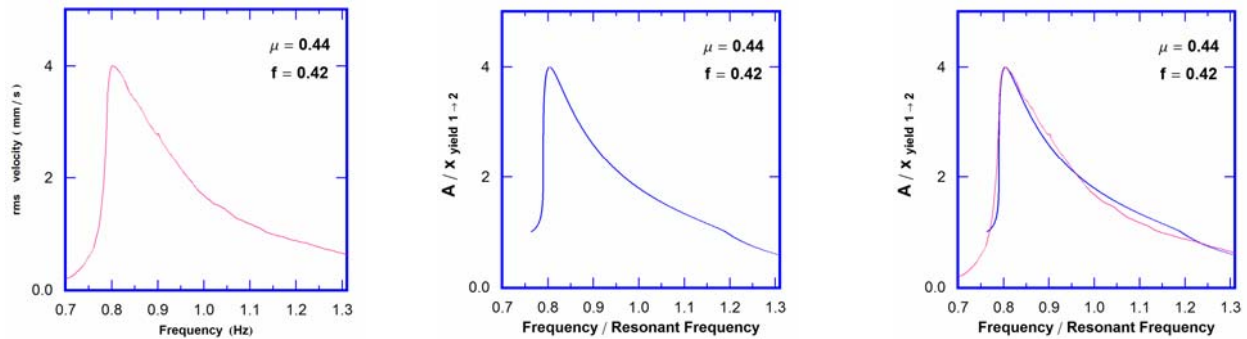
Figure 35 – Applying the Caughey model to experimental data. Experimental tuning curve (left), theoretically predicted tuning curve (middle), and overlay of experimental and theoretical tuning curves (right).

Applying the Caughey theory, the yield force for the soil-mine simulant system is determined to be $F_y \sim 6.1\,N$.

2.3 Electrodynamic Soil Plate Oscillator

2.3a. Measuring the Relationship between the Driving Force and the Vibration Response

A second variant of the soil-plate oscillator replaces the acoustic driving force with an electromagnetic one. An inductor coil mounted on a force gauge (PCB Piezotronics Model No. 208C01, sensitivity = 110.7 mV/N) is placed below the clamped plate and mounted inside the bottom flange to the base of the apparatus. Rare earth magnets are affixed to opposing sides of the clamped plate such that the plate is driven in a similar fashion to a loudspeaker. See Figure 36 and Figure 37.
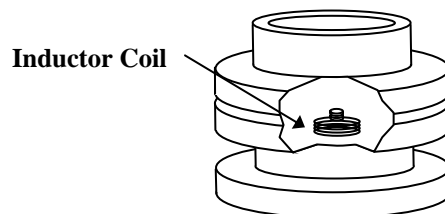
Figure 36 – Soil-plate oscillator instrumented with a dynamic force gauge, stationary magnetic coil, and moving powerful rare earth magnets
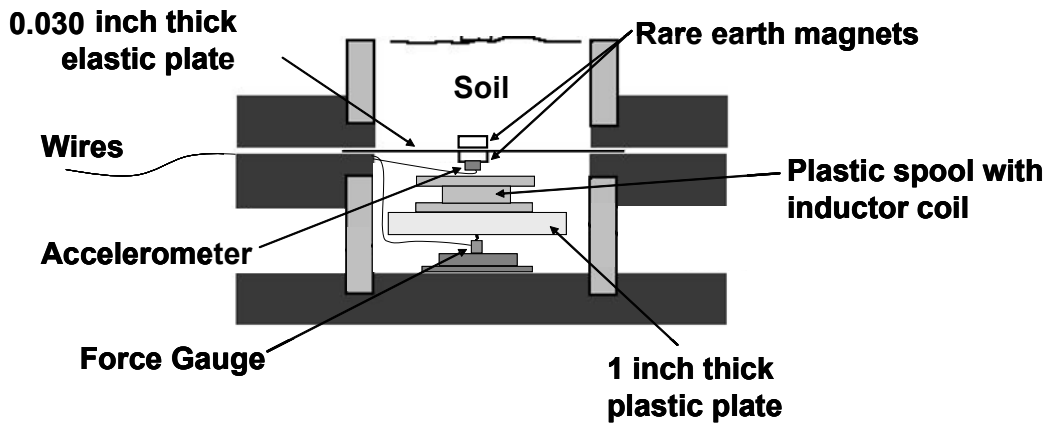
Figure 37 – Schematic of the soil-plate oscillator instrumented with a dynamic force gauge, stationary magnetic coil, and powerful rare earth magnets used to drive the plate.

Figure 38 shows a comparison of the applied driving force versus acceleration response of the elastic plate observed near resonance for the case of (a) no soil mass loading and (b) soil loading. In the case of no soil loading, the smooth Lissajou pattern is indicative of linear behavior. In contrast, the pointed Lissajou pattern in the case of soil loading signals that the behavior observed appears to be nonlinear.
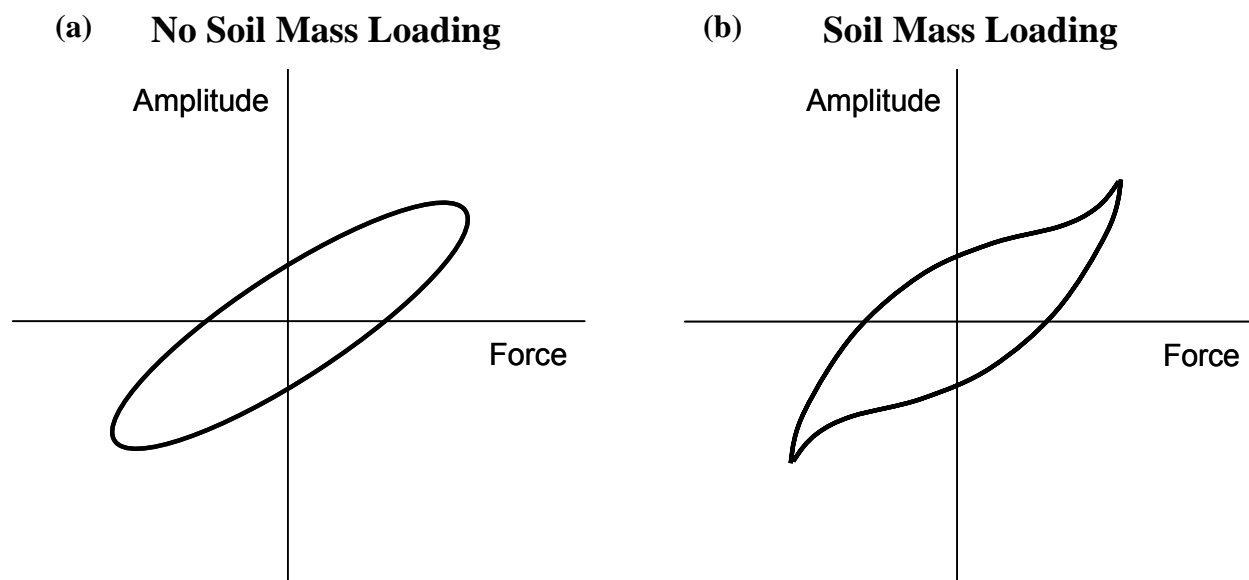
Figure 38 – Lissajou figures for the case with (a) no soil loading and (b) soil mass loading.

2.3b. Measuring the Dynamic Impedance of the Soil-Plate Oscillator as a Function of Amplitude

A smaller iron soil-plate oscillator (4 5/8 inch inner diameter) has also been configured in the electro-dynamic setup with a 400-turn Pasco electromagnetic coil. See Figure 39.
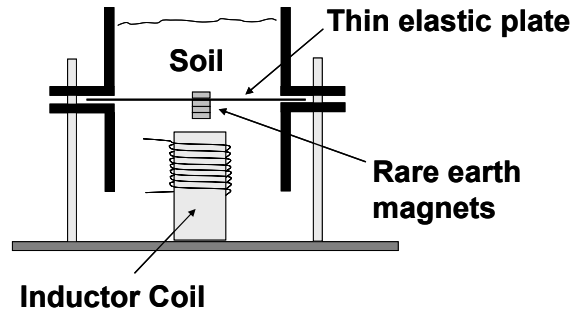
Figure 39 – Small soil-plate oscillator instrumented with a stationary Pasco 400-turn inductor coil and moving powerful rare earth magnets

This particular electro-dynamic setup allows for precise impedance curve measurements to be taken, from which the lumped mechanical acoustic parameters of the system can be measured. The electrical impedance of the electro-dynamic soil-plate oscillator is given by

$$Z_{Electrical} = R_E + j\omega L_E + Z_{motional} = R_E + j\omega L_E + \frac{(B\ell)^2}{Z_{mechanical}}$$

Equation 54

where R_E is the resistance of the wire in the coil, L_E is the inductance of the coil, $Z_{mechanical}$ is the impedance of the combined soil-plate oscillator, and B is the effective magnetic field reaction on the coil of effective length ℓ. Electrical measurements showed that $R_E \sim 0.22\,\Omega$ and $L_E \sim 3.0\,mH$ well below resonance. The complex mechanical impedance is defined to be

$$Z_{mechanical} = \frac{F}{u}$$

Equation 55

where F is the complex driving point force and u is the complex particle velocity at the driving point.
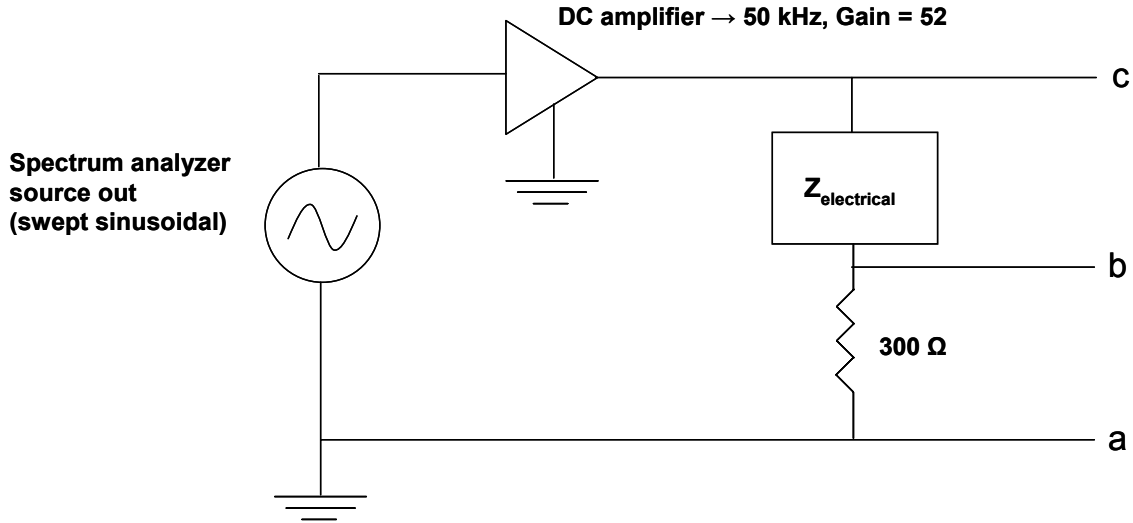
Figure 40 – Circuit diagram of the electro-dynamic soil-plate oscillator apparatus.

The circuit diagram in Figure 40 shows how the electrical impedance of the system is experimentally measured. The voltages V_{ab} and V_{bc} go to channels one and two, respectively, of the Agilent spectrum analyzer, which operates in swept sinusoidal mode. Simple circuit analysis shows that the electrical impedance can be computed from the ratio of complex voltages.

$$Z_{electrical} = (300\Omega)\left(\frac{V_{ab}}{V_{bc}}\right)$$

Equation 56

Figure 41 shows the experimental results obtained from measurements of the electrical impedance as a function of incrementally increased drive amplitude. Since the electro-mechanical coupling parameter $(B\ell)^2$ is independent of frequency, once the R_E and $j\omega L_E$ contributions from the coil are canceled, the mechanical impedance can be computed from

$$Z_{mechanical} = \frac{(B\ell)^2}{Z_{motional}}$$

Equation 57

The results from Figure 41 clearly show that the frequency of mechanical resonance decreases with increasing drive level. This is in agreement with the earlier soil-plate oscillator mechanical measurements of tuning curve acceleration versus frequency. The real part of motional

impedance corresponds to the amount of damping in the system. As drive amplitude increases, the effective damping of the system decreases, but the quality factor is seen to increase. The imaginary part of motional impedance is related to the mass-spring like behavior of the system. At higher frequencies, mass-like behavior dominates spring-like behavior. The opposite is true at lower frequencies. The experimental data shows a shift from mass-like to spring-like behavior as drive amplitude increases.
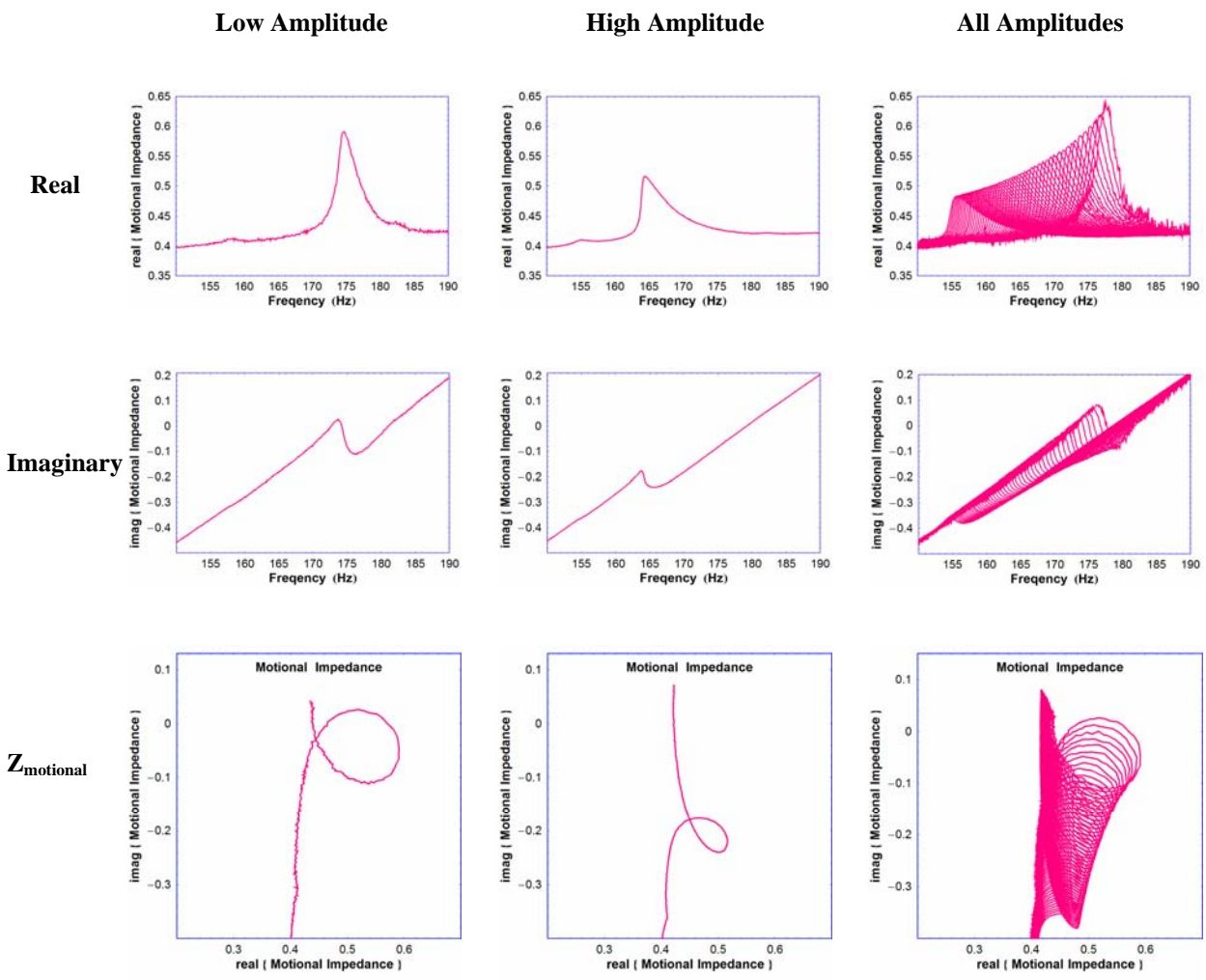
Figure 41 – Motional impedance plots from the electro-dynamic soil-plate oscillator

The footprint shape of the tuning curve is depicted from the motional impedance plots of the real versus imaginary parts of $Z_{motional}$, which progress from a circular loop (linear response) to a distorted loop (nonlinear response) as drive amplitude increases. $Z_{mechanical}$ near a mechanical resonance can be expressed as

$$Z_{mechanical} = b_{eff} + j\left(\omega M_{eff} - \frac{K_{eff}}{\omega} \right)$$

<div align="right">**Equation 58**</div>

Here b, M, and K are the effective damping constant, mass, and spring constant of the combined soil-plate oscillator system. However, a nonlinear mathematical model for the point mechanical impedance of the soil-plate oscillator is needed to further develop expressions for the amplitude dependence of the mechanical impedance near resonance.

2.4 Nonlinear Detection of a Buried Landmine Simulant

Having separately examined the nonlinear properties of soil and the soil-plate boundary, attention is now given to nonlinear detection of a buried landmine simulant. The mine simulant detection problem involves near-field scattering effects along with the challenges of understanding the system nonlinearity. Experiments are performed in an anechoic chamber facility. The drum-like mine simulant is shown in Figure 42. The simulant case is fabricated from a 6.4 mm thick (11 cm inner diameter, 12.3 cm outer diameter) acrylic tube that is 6 cm long. A thin, circular acrylic plate (0.76 mm thick) is fused to the "top" end of the tube to model the effects of a circular clamped elastic plate. A 6.4 mm thick "bottom" plate is fused to the opposite end of the tube.

Thin Acrylic Top Plate

Acrylic Mine Simulant:

Inner diameter = 11 cm
Height of casing = 6 cm
Wall thickness = 0.64 cm
Plate thickness = 0.076 cm
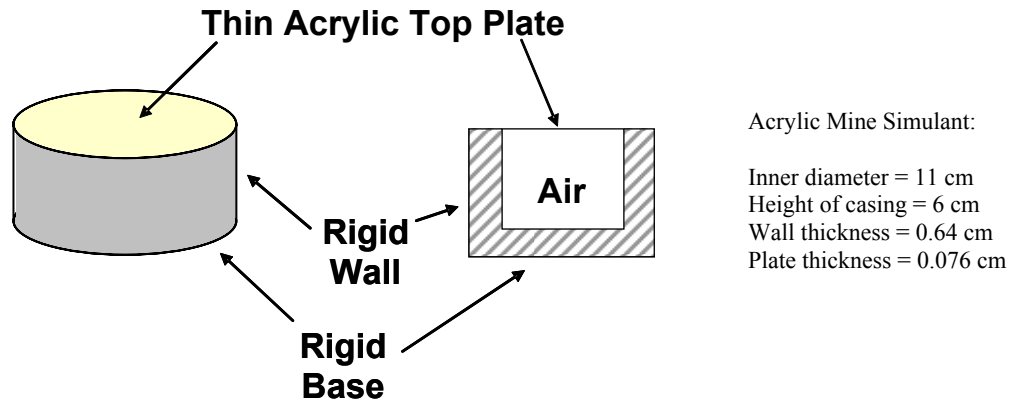
Figure 42 – Mine Simulant

The experimental setup involving the buried simulant is shown in Figure 43. As before, the Agilent spectrum analyzer is used to generate a swept sine source voltage. The signal is amplified to drive the loudspeakers, which generate an acoustic drive pressure. A laser Doppler vibrometer (LDV) in a forward-looking orientation is used to measure soil surface vibration. A microphone measures acoustic sound pressure. The LDV is mounted to a tripod inside the anechoic chamber using two Velmex UniSlide® rotary tables. The rotary tables are connected orthogonally so as to produce a biaxial sweeping capability. Each rotary table is controlled by a separate Velmex NF90 step motor controller. The entire experiment is remotely controlled using a LabVIEW® program written during a month-long development period in January 2007. The program is capable of automatically controlling the scan position of the LDV, operating the spectrum analyzer, and storing data directly to the computer's hard drive. Appendix F provides a more detailed description of the computer algorithm as well as some sample LabVIEW® programming code.
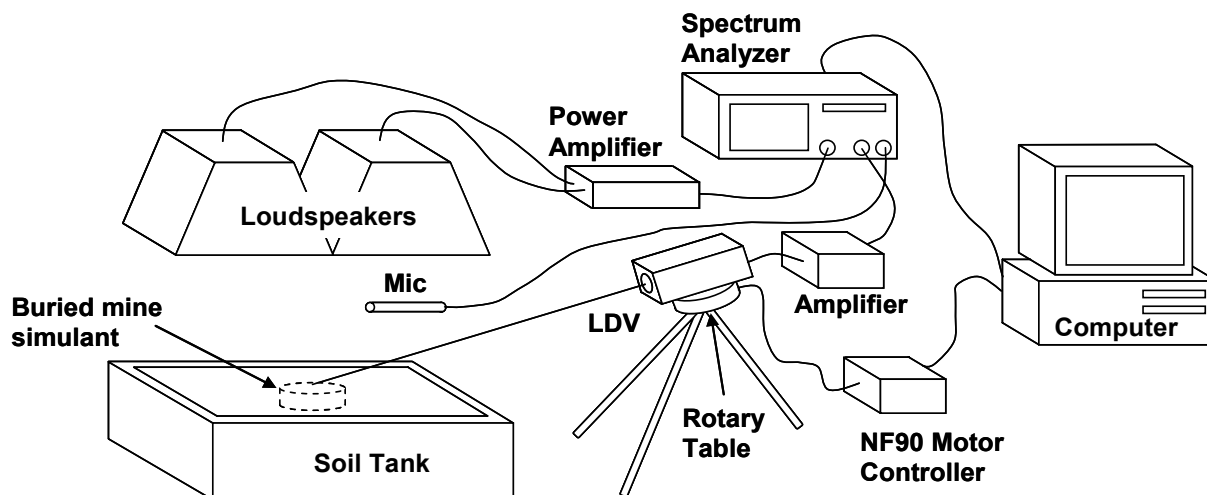
Figure 43 – Soil-Mine Simulant Oscillator Experimental Apparatus

2.4b. Comparison of the "On the Mine" versus "Off the Mine" Nonlinear Resonant Response for a Mine Simulant

The resonant characteristics of the soil surface will vary due to the natural layering of the

soil, inhomogeneities, and burial depth. For the experiments performed in the soil tank, the dry

sifted masonry sand is used to reduce the effects of layering and inhomogeneities. The low

frequency cut-off of resonant soil vibration modes in the tank is around 250 Hz.
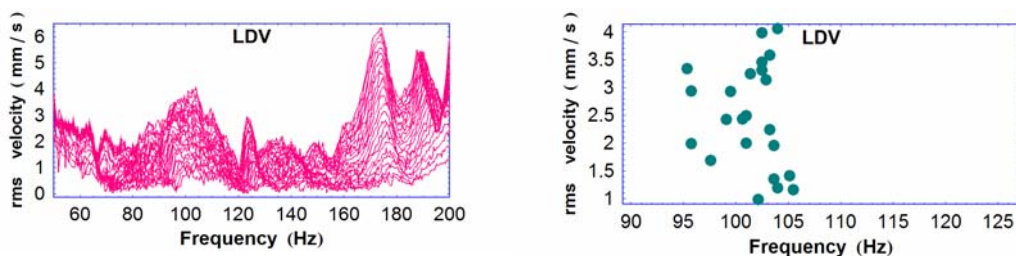
Figure 44 – Resonant tuning curves 10 cm away from the center of a mine simulant buried in masonry sand inside the anechoic chamber.
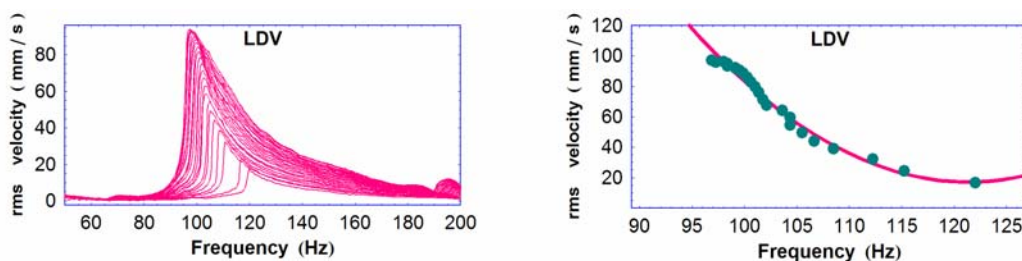
Figure 45 – Resonant tuning curves directly over the center of a mine simulant buried in masonry sand inside the anechoic chamber.

For an acrylic mine simulant (Figure 42) buried 2 cm deep, resonant tuning curve measurements were made at various scan positions across one radial axis of the simulant. The acoustic drive level was incremented linearly from 99.3 dB to 120.9 dB and a collection of 22 tuning curves was measured for each of the 31 scan locations. Tuning curves shown in Figure 44 and Figure 45 compare the responses between a location 10 cm away from the center of the buried mine simulant and one directly over the mine simulant, respectively. There is little appreciable resonant response "off target" and there is a great deal of scatter when attempting to determine a backbone curve. The tuning curves shown in Figure 45 exhibit a relatively strong response measured "on target." Here, the backbone curve shows considerable "softening" and resembles the bilinear hysteresis results derived in the Caughey model (Section 2.2c.). The greatly reduced nonlinear resonant behavior as one moves from an "on target" to an "off target" location seems to indicate that the observed nonlinearity involves the interaction of the soil-top plate interface.

2.4c. One-Dimensional Velocity Profiles

Tuning curves are measured at each scan position by incrementing the acoustic drive amplitude from lower to higher values. The process is repeated at each new scan position across the buried landmine simulant. For each discrete drive amplitude, a profile of peak vibration amplitude is plotted as a function of position. The single-peaked soil vibration response

indicates that the mine simulant is oscillating in its fundamental mode of vibration. For acoustic drive levels below 105 dB, the skirts of the profile show irregular behavior.
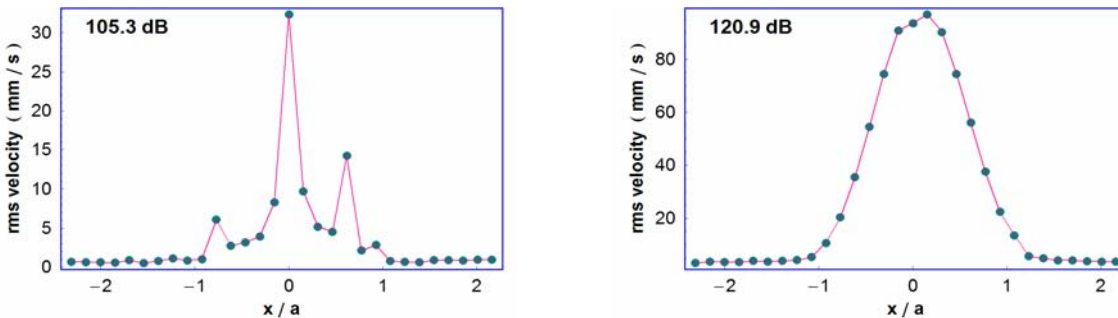
Figure 46 – Velocity profiles as a function of the mine's radius (a = 5.5 cm) for small and large acoustic drive levels.

Figure 46 displays plots of the system's velocity response at each given scan location across a radial axis of the mine. The radius of the mine simulant is a = 5.5 cm. The plotted velocities are *not* the peak amplitude responses from each scan position, though they correlate closely. The necessary velocity components from the tuning curve measurements taken at each location represent the amplitude response at a given drive level for the exact same reference frequency. More specifically, the frequency of the largest amplitude response per drive level when located directly over the buried simulant becomes the chosen reference frequency. The vibration amplitude at that frequency and drive level is extracted from the remainder of the locations to produce the profiles seen in Figure 46. The leftmost figure is obtained from a relatively low-level acoustic drive pressure. In contrast, the figure on the right is obtained from a significantly larger acoustic driving force.
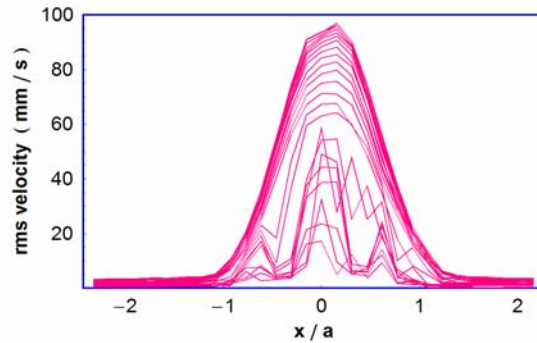
Figure 47 – Velocity profiles for all drive amplitudes referenced to the frequency of maximum resonance directly over the mine.

Velocity profiles for each discrete drive level (from 99.30 dB to 120.9 dB referenced to 20μPa) are superimposed in Figure 47. The profiles obtained from the larger drive levels clearly show that the simulant is oscillating in its fundamental mode of vibration. It is tempting perhaps to believe that the irregularities observed in the case of lower drive levels imply an interesting physical phenomenon or perhaps resonance in other than the fundamental mode. This is not the case, however – the multiple peaks observed result from resolution limitations of the measured frequency response. This assertion is verified by looking at a plot of peak resonant amplitude versus radial position for each drive level, as shown in Figure 48. Whereas the actual frequency of peak resonance may shift slightly from the peak resonant frequency directly over the mine, the plot of peak amplitudes ensures the clearest possible picture of the simulant's resonant response. It becomes clear that the simulant is in its fundamental vibration mode at all drive levels. However, this latter technique, while valuable for "on the mine" analysis, is not useful for "off the mine" locations. As there are no clearly identifiable maximum resonances when located "off target," it cannot be used to extend the velocity profile beyond the actual radius of the mine.
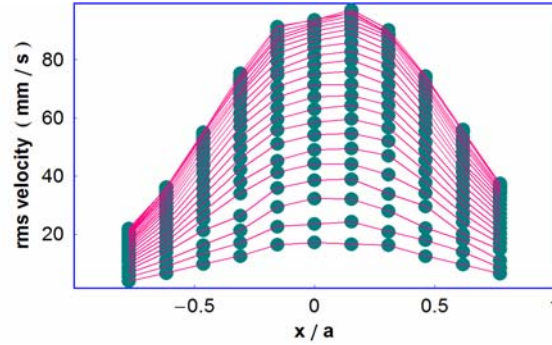
Figure 48 – Maximum velocity profiles as a function of mine radius (a = 5.5 cm)

2.4d. Two-Dimensional Velocity Profiles

A two-dimensional profile using a grid of 15 by 15 points is shown in Figure 49. The relative magnitude of soil particle velocity measurements is transferred into a contour plot in Figure 50. Each contour corresponds to a 10 mm/s increase in vibration velocity. The smooth surface plotted in Figure 51 is a Gaussian fit to the experimental data. The fitted function about the central peak is of the form

Equation 59

$$f(x, y) = \gamma e^{-\frac{x^2}{2\beta_x^2} - \frac{y^2}{2\beta_y^2}}$$

Additional two-dimensional profiles for linearly increasing acoustic pressure between 131.8 dB and 150.9 dB are shown in Appendix H. For the case of the sound pressure level equal to 150.9 dB, $\beta_x = 0.490a$, $\beta_y = 0.406a$, and $\gamma = 120.202$ mm/s.
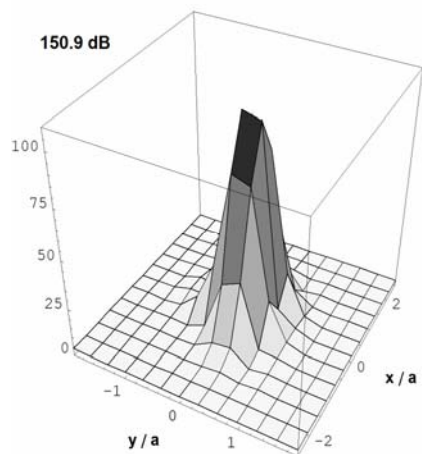
Figure 49 – Soil surface vibration velocity profile as a function of radial position from a buried simulant.
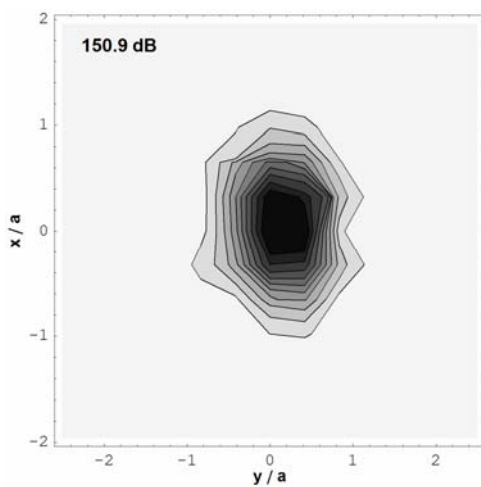
Figure 50 – Contour plots of soil surface vibrations.
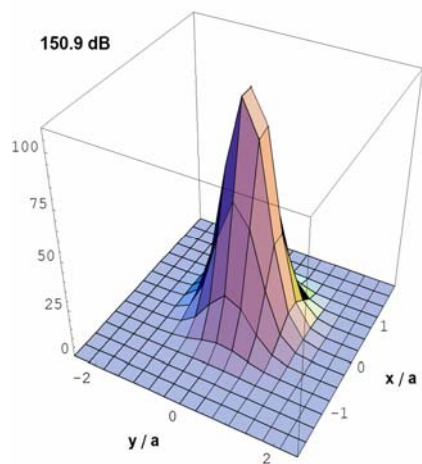
Figure 51 – Gaussian fits to the experimental soil surface vibration data collected in two-dimensions.

2.5 VS 1.6 Anti-tank Landmine

Figure 52 shows a plastic VS 1.6 anti-tank landmine. A cross-section view showing the detail of the top plate reveals a circumferential leaf-spring support of a plastic top plate, which does not have uniform thickness.
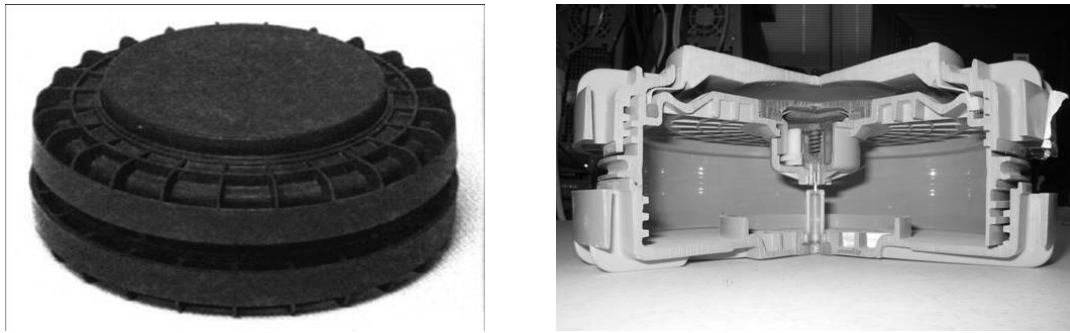
Figure 52 – VS 1.6 plastic anti-tank mine and cut-away view.

2.5a. Comparison of the "On the Mine" versus "Off the Mine" Nonlinear Resonant Response for a VS 1.6 Landmine

An inert VS 1.6 landmine is buried beneath a smooth, flat layer of soil supported by concrete soil tank on the concrete floor in the laboratory room. The experimental apparatus is shown in Figure 53. The same experiments performed using the buried mine simulant (sections 2.4b and 2.4c) are performed for the buried VS 1.6 landmine. Resonances involving the intricate shape of the actual landmine casing are not easy to predict from theory. The VS 1.6 has a compliant pressure plate, but its complex overall structure causes additional resonant peaks to appear in the resonant tuning curve experiments. The tuning curve experiments are performed over a bandwidth that is below the 300 Hz cut-off frequency for vibration modes in the large soil tank.
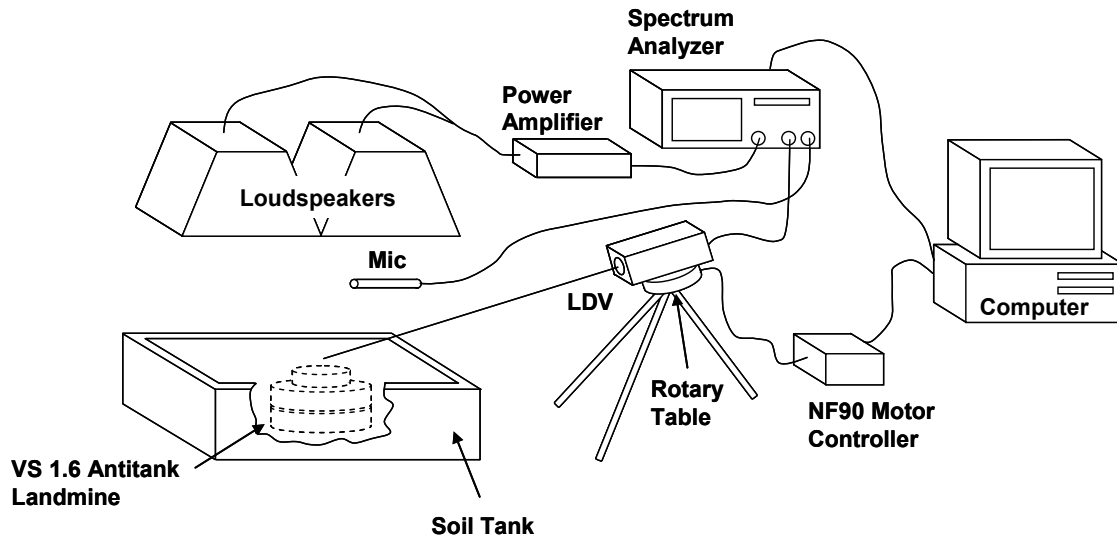
Figure 53 - Soil-Mine Oscillator Experimental Apparatus

The VS 1.6 exhibits aspects of both the elasto-slip (section 2.1d) and bilinear hysteresis models (section 2.2c) depending upon the range of drive amplitudes investigated. For sound pressure levels in the range 82.6 dB to 107.7 dB, the tuning curves for the VS 1.6 display linear backbone curves (shown in Figure 54). The vertical portion of the backbone curve that is measured at very low amplitudes indicates that $\beta \ll 1$ when applying the Iwan model.
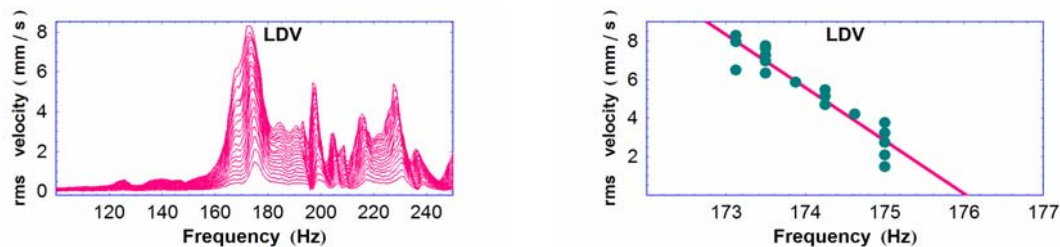
Figure 54 – Resonant tuning curves and backbone curve directly over a buried VS 1.6 landmine at relatively low drive levels.

In contrast, if the maximum limit of the drive level is increased to 113.6 dB, the resonant response of the VS 1.6 shows an upward curvature that resembles the backbone curve behavior predicted by Caughey's bilinear hysteretic model. Resonant tuning curves measured directly over the buried mine for larger drive amplitudes are shown in Figure 55.
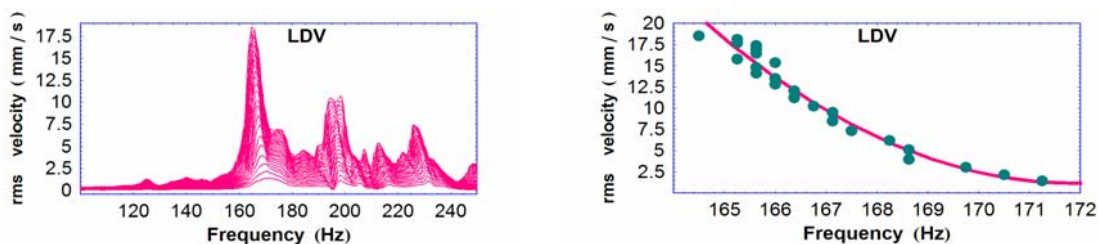
Figure 55 – Resonant tuning curves and backbone curve directly over a buried VS 1.6 landmine over a relatively larger range of drive levels than used in Figure 54.

2.5b. One-Dimensional Velocity Profiles

The automated scanning apparatus is used to create velocity profiles as a function of mine

radius for the buried VS 1.6 landmine. The velocity profiles are shown collectively in Figure 56.

Here, the frequency resolution limitations at low drive amplitudes appear to be less significant

than in the case of the simulant. The single-peaked shape of the velocity profile indicates that

the compliant pressure plate of the mine is oscillating in its fundamental mode of vibration.
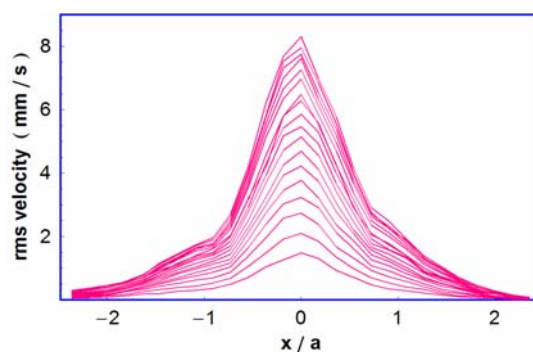
Figure 56 – Velocity profiles of a buried VS 1.6 anti-tank landmine as a function of mine radius.

2.5c. Effects of grazing angle upon experimental measurements.

Experiments to this point have been conducted with a relatively large grazing angle

(between 30 and 45 degrees depending upon scan location). As the grazing angle diminishes, so

does the strength of the signal response measured by the LDV. Measurements are possible

because of the rough surface back-scattering that occurs when the laser light is incident upon the

granular soil. Experiments reported here show that at some minimum grazing angle, the LDV

cannot properly detect the scattered signal. It is believed that the frequency modulation circuit in

the Polytec100 LDV may be dropping out of its own dynamic detection range. This might be due to the elongated laser spot size on the rough surface which causes a scattered speckle pattern and results in a noisy analog detection voltage.   This minimum grazing angle is experimentally determined to be 19 degrees. Figure 57 shows a bandwidth of frequencies containing the fundamental resonant frequency of the VS 1.6 mine itself. The laser spot is located directly over the center of the buried mine. For grazing angles greater than or equal to 19 degrees, there is a strong resonant response. Conversely, for grazing angles smaller than 19 degrees there is no measurable soil surface vibration response. The measured soil surface vibration for various angles of incidence is shown in Figure 57.

18 degrees

18.5 degrees

18.75 degrees

19 degrees

20 degrees
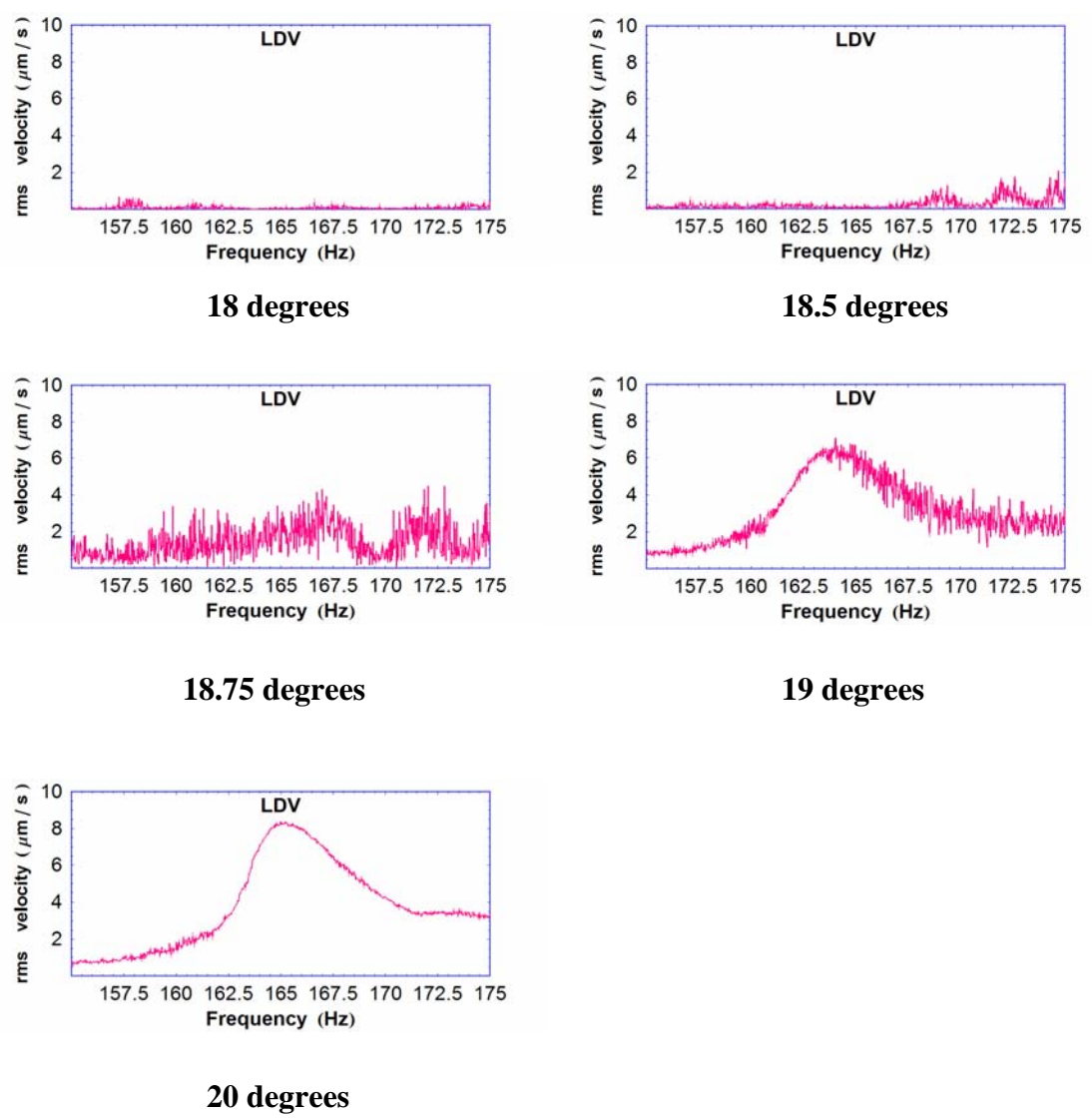
Figure 57 – Tuning curves measured directly over the buried mine using a forward-looking LDV for a variety of grazing angles.

Conclusions

Acoustic-to-seismic methods have shown tremendous promise in positively identifying

landmines. The nonlinear behavior that arises when a compliant buried landmine is excited is an

incredibly complex phenomenon. At present, the intricate physics concerning the interaction of

a granular media and the top plate of a landmine are not extremely well understood. The

experiments contained herein attempt to characterize the observed nonlinear behavior through a

variety of modeling and profiling techniques.

The soil-mass oscillator apparatus effectively enables one to measure the elastic

parameters of a soil medium by performing mass loading experiments and applying linear

acoustic theory. The stiffness of dry, sifted masonry sand is measured to be

$k_{eff} = (4.4 \pm 0.1) \times 10^6 \, \dfrac{N}{m}$, and the sound speed in the medium at $T = 20^o \, C$ is (149 ± 1) m/s.

When A/S techniques are employed, the masonry sand is shown to undergo softening. That is,

as the drive amplitude increases, the resonant frequency of the soil decreases. The linear nature

of this backbone curve identifies the system as potentially mesoscopic elastic.

The elasto-slip model of elastoplastic hysteresis presented by Iwan exhibits linear

backbone behavior and is used to model the Soil-Mass Oscillator. Iwan's model is based upon a

distribution of Jenkin's elements, a series-parallel arrangement of springs attached to slip-

dampers. Depending upon the bandwidth of the distribution of elements, a function of β, the

backbone curve will change shape slightly. For β = 1, the backbone curve is completely linear.

Applying the Iwan model to experimental data, the average yield force for the soil lattice

structure of the masonry sand over eleven trials is calculated to be 2.9 N with a standard

deviation of 0.42 N. Different soils have different lattice yield points. Loess soil is shown to yield at (5.9 ± 0.3) N.

A secondary model which has great potential value in studying the nonlinear soil-mine system is the Local Interaction Simulation Approach (LISA). LISA is a statistical formulation based upon a distribution of elements having unique bi-state protocols. The LISA model is shown to produce hysteresis loops in stress-strain diagrams very similar to those presented in the Iwan model. This fundamental similarity in regards to the hysteretic behavior of the model lends tremendous credence to the application of LISA to the nonlinear acoustic landmine detection problem. Further studies connecting the microscopic parameters of soil with the phenomenological equations of state employed by LISA are needed before the model can be directly applied.

The Soil Plate Oscillator apparatus allows the nonlinear behavior that develops at the soil-plate interface to be studied. Theory predicts that vibrations of a clamped plate should be linear. Empirical data from the oscillator in the absence of soil mass loading actually exhibited a slight stiffening effect.

A comparison of the overall nonlinearity of the soil-mass oscillator and soil-plate by regression analyses of resonant tuning curves. The soil-mass oscillator loaded with loess soil is the least nonlinear of the systems studied. The soil-thin plate oscillator loaded with masonry sand is the most nonlinear of those studied.

At large drive amplitudes, the resonant tuning curve behavior appears to depart from the linear backbone predictions of both the Iwan and LISA models. A bilinear model of hysteresis developed by Caughey seems to provide a more accurate description of the complicated

nonlinear behavior. Fitting Caughey's theoretical predictions to empirical data, the lattice yield force is computed to be approximately 6.1 N.

A variant upon the acoustically driven soil-plate oscillator, the electro-dynamic soil-plate oscillator enables extremely accurate measurements of motional impedance to be obtained. At very low drive amplitudes, the circular Lissajou patterns signal relatively linear behavior. As the drive amplitude increases and nonlinearity is introduced into the system, the Lissajou patterns become distorted. The downward shift in resonant frequency that occurs as drive amplitude increases corresponds to the behavior observed in the soil-mass and soil-plate oscillators. Further, the decrease in the effective resistance of the system and increase in the quality factor of the oscillation as drive amplitude grows is in accordance with expected behavior of nonlinear mesoscopic elastic systems. A great deal of future study can be undertaken with the electro-dynamic soil-plate oscillator.

The design and implementation of an automated LabVIEW® control system was instrumental in generating soil surface vibration profiles of a buried acrylic mine simulant and an inert VS 1.6 plastic anti-tank mine. In both cases, the nonlinear behavior observed "on-target" greatly surpassed the negligible responses seen "off-target." At large drive amplitudes, both the mine simulant and VS 1.6 exhibited the curved backbones similar to those seen in the Caughey model of bilinear hysteresis. Low amplitude driving of the VS 1.6 showed linear backbone behavior as predicted by Iwan.

One-dimensional velocity profiles of soil surface vibration as a function of scan position indicate that both the mine simulant and VS 1.6 landmine oscillate in their fundamental mode of vibration. The mine simulant was profiled in two dimensions. The resulting velocity profile is fit to a Gaussian.

Lastly, the increased noise caused by speckle and backscatter of laser light from a granular medium establishes a minimum grazing angle beyond which landmine detection cannot occur. For the experimental setup described here, the grazing angle is determined to be 19 degrees.

Potential for future study in the area of nonlinear acoustic landmine detection is very promising. The models presented herein verify the existence of nonlinear mesoscopic elastic behavior in the soil-mine system, and they provide a solid foundation for more complex modeling techniques. A breakthrough connection between microscopic features and mesoscopic elastic parameters could potentially lend a predictive value to the LISA model. One of the greatest shortcomings at present is the time requirement for signal processing.   While nonlinear acoustic landmine detection techniques are extremely reliable, they are also quite slow. Technological improvements could greatly improve data collection rates and make this detection technique a reality.

Appendix A - Experimental Equipment

A1. Electronic Equipment

The Agilent 35670A Dynamic Spectrum Analyzer is a dual channel electronic instrument and has a bandwidth of 100 kHz per channel. It can be operated with a high frequency resolution (better than 0.1 Hz if needed), and its 90 dB dynamic range makes it an extremely versatile instrument in applications involving spectral analysis. In the swept sinusoidal mode, the instrument takes the average of many Fast Fourier Transforms (FFTs) for each sweep location (typically 5 cycles per point) that synchronously corresponds to the output frequency of the analyzer. The sweep rate, number of points per sweep, and the resolution of the instrument are easily configured and changed for a variety of experimental setups.

In the swept sinusoid mode, the spectrum analyzer is responsible for generating a constant amplitude sinusoidal tone that changes its frequency linearly from the beginning to the the end of the designated frequency band. Simultaneously, the analyzer records the FFT of the input time varying voltages to channels one and two in a narrow bandwidth centered about the source out frequency.

The source output was connected to a pair of 21 cm diameter loudspeaker through two separate AIWA stereo integrated power amplifiers (model no. SA-A6OU) for the mine simulant experiments. For the VS 1.6 experiments, two 12 inch subwoofer speakers were driven using CE2000 Crown Audio Power Amplifiers. Typically, the vibration transducer device (see below) was connected to channel one, and the acoustic pressure was measured by a microphone connected to channel two. Both channels were displayed as separate traces of voltage versus frequency on the front panel display of the spectrum analyzer.

A2. Vibration Measurement Devices

A2i. Piezoelectric Accelerometer

Small Endevco accelerometers with nominal sensitivity 0.300 pC/(m/s^2) were used to

make contact vibration measurements. Each accelerometer was connected to an Endevco charge

amplifier, which converts the alternating charge stored on the piezoelectric crystal to an

alternating voltage with relatively low output impedance. A miniature 2 gram B&K

accelerometer (3 cm diameter and 3 cm tall) along with a B&K charge amplifier was also used.

The transducer in each of these accelerometers is a compression sensitive piezoelectric

crystal affixed to a stationary mass (Figure 58). As the accelerometer is subjected to longitudinal

compression, it is compressed against the mass and produces electric signals that correspond to

the magnitude of compression. The Endevco accelerometers have minimal transverse sensitivity

(0.5 – 2.0%). Consequently, they are less sensitive to rocking motions. This characteristic

makes them particularly useful in experiments where ambient vibrations or non-orthogonal

motion may be masking the desired surface vibrations.
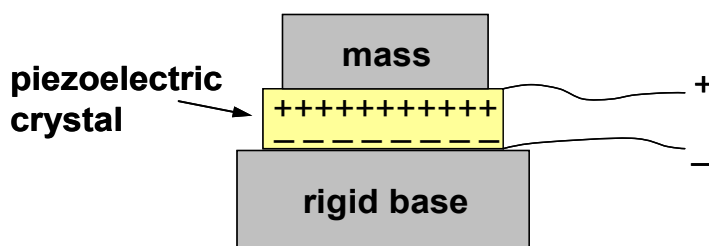
Figure 58 – Piezoelectric accelerometer

A2ii. Geophone

The SM-11 geophone is designed to detect seismic vibrations in the frequency range

between 80 Hz and 500 Hz. It is also used as a contact vibration measurement device. As the

geophone vibrates, the movement of a magnet mounted on two leaf springs inside a stationary

inductor coil (Figure 59) induces an electric current in the coil. The induced electromotive force

is proportional to the particle velocity of vibration. The output impedance of the geophone is

relatively low, so it is capable of driving a voltage signal along a long coaxial cable connected to a high impedance load.
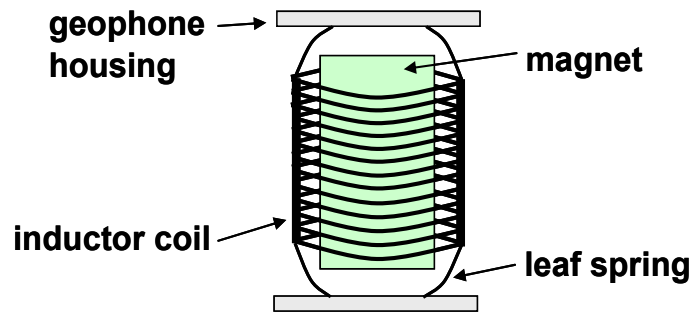
Figure 59 – Geophone

A2iii. Laser Doppler Vibrometer (LDV)

The Polytec PDV-100 laser vibrometer is used to remotely measure soil surface vibrations. Since there is no physical contact between the LDV and the soil, the LDV has the added benefit of being able to detect soil surface vibrations without mass loading. The sensitivity of the LDV varies within different bandwidths of operation. The particle velocity vibration at the soil surface causes a slight Doppler shift in the reflected laser beam. An interferometer inside the LDV converts the Doppler shift into an equivalent voltage which is proportional to the velocity of the reflected surface (considering normal incidence).

If the LDV is mounted in a forward-looking orientation, one must account for the fact that the component of particle velocity along the direction of the laser beam decreases with angle. The normal component of the particle velocity decreases by a factor of $\sin\theta$ as the grazing angle θ decreases. Only the shift that occurs in the direction of the laser beam contributes to the Doppler effect. See Figure 60.
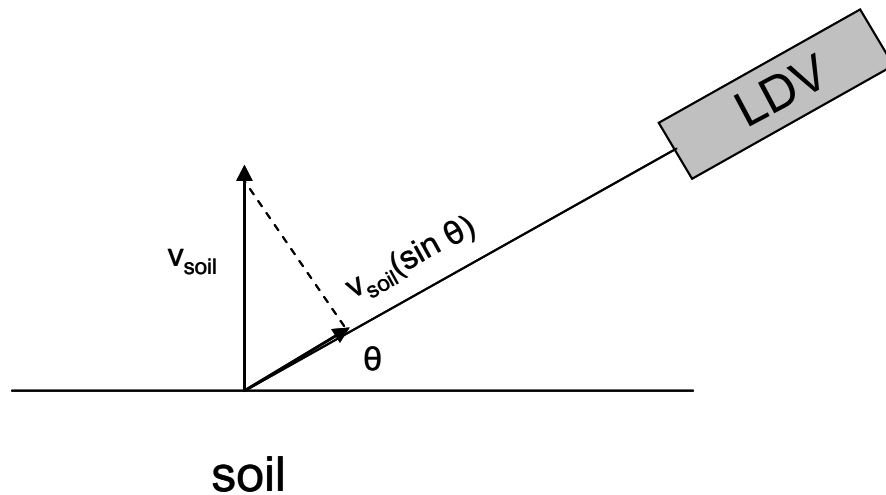
Figure 60 – Effect of grazing angle on the laser Doppler vibrometer

It is not the intensity of the LDV signal diminished by scattering that causes the

frequency modulated (FM) detection to become noisy. The LDV's incident beam undergoes

light scattering from the granular medium that introduces a speckle noise interference pattern in

the scattered waves. The problems involving the demodulation of laser light due to back-

scattering from a granular rough surface (introducing noise in the FM detection system otherwise

known as speckle noise) has been addressed in the specific context of landmine detection by

Goggans *et al.*[14]

Appendix B - Linear versus Nonlinear Behavior

Whenever a system excited by a harmonic force with a single "primary" frequency component generates an oscillation response with frequency components other than the primary, the system is said to exhibit nonlinear behavior. This behavior is called distortion and can be commonly observed when one overdrives the loudspeakers on a stereo system. The differences between linear and nonlinear behavior can be illustrated by comparing the oscillations of a mass suspended by a spring with the oscillations of a mass suspended by an elastic band. The mass on the spring exhibits linear behavior as the spring force varies linearly with position. A plot of the displacement amplitude versus time will exhibit pure sinusoidal behavior. The mass on the elastic band is a nonlinear system because the restoring force is not a linear function of its position. At each crest the oscillating mass will "jump," thus exhibiting an amplitude versus time response that will not show pure sinusoidal behavior.

The complexity of the nonlinear response relative to the linear response can be observed by comparing the Fast Fourier Transforms (FFT) of both systems. Mathematical Fourier analysis shows that periodic functions, which are a superposition of harmonic tones of varying amplitude, can be decomposed into their components. In the case of the linear signal, the output frequency spectrum exhibits only one frequency. In the nonlinear system, the output frequency spectrum is a superposition of several tones. See Figure 61 and Figure 62.
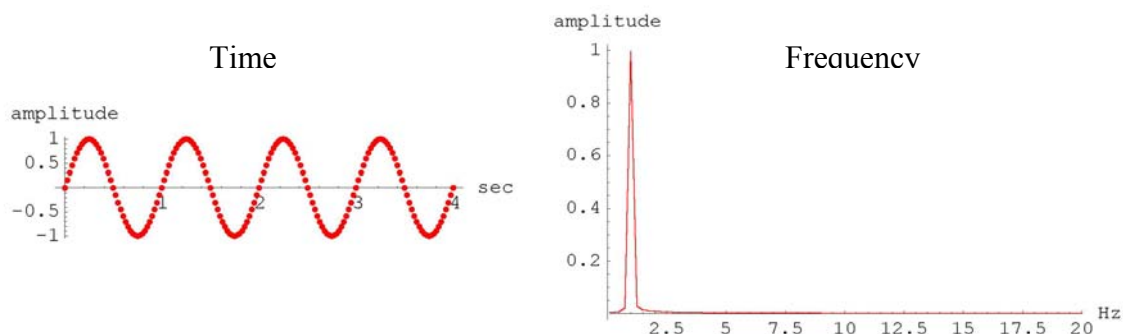
Figure 61 - A linear oscillator has a sinusoidal displacement amplitude. The oscillation is not distorted so that a single spike is observed in the Fourier spectrum.
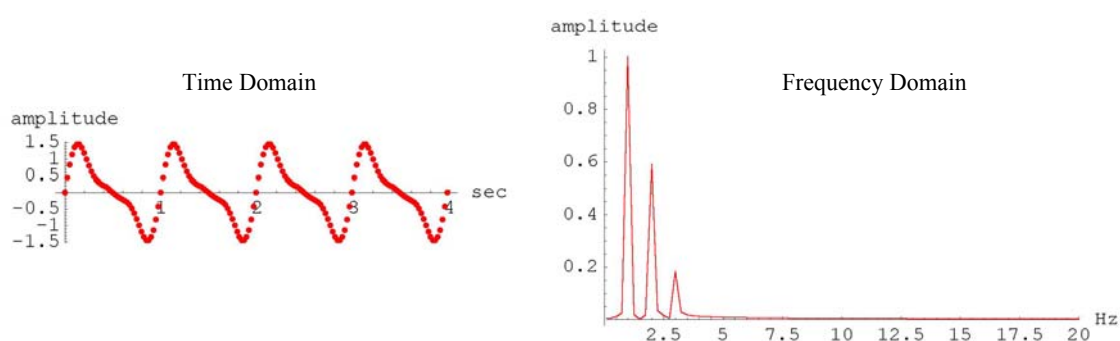
Figure 62 - The displacement amplitude of a nonlinear oscillator deviates from sinusoidal behavior. The oscillation exhibits distortion so that several spikes (frequency components) are observed in the Fourier spectrum.

The soil-mine system is nonlinear. In particular, it is the soil-mine interface that exhibits the very strong nonlinear behavior that is observed. Thus, while linear acoustic methods have been used as an effective technology for detection schemes, nonlinear acoustic mine detection improve upon linear acoustic detection methods by increasing the "on the mine" versus "off the mine" vibration amplitude contrast ratio and eliminate certain types of "false alarms."

Appendix C – Soil-mass oscillator tuning curves, backbone curves, spring constants and Iwan-model yield forces

Figure C-1
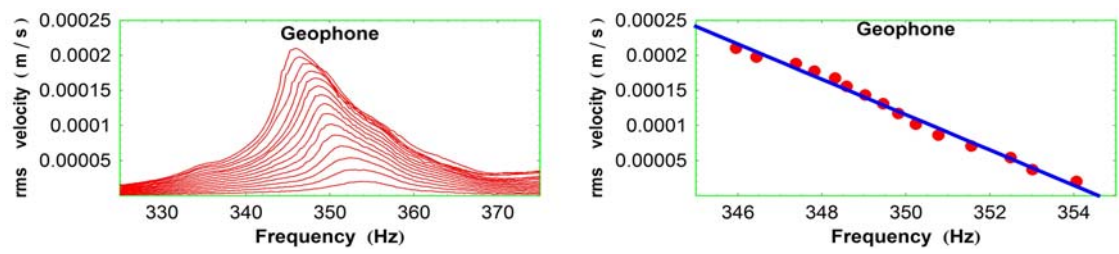
Figure C-2
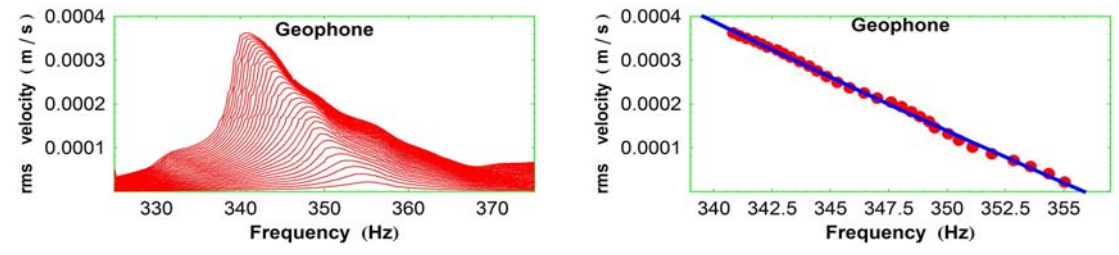
Figure C-3
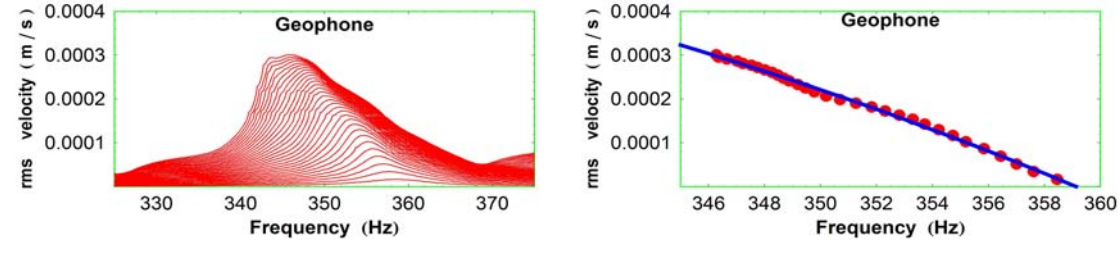
Figure C-4
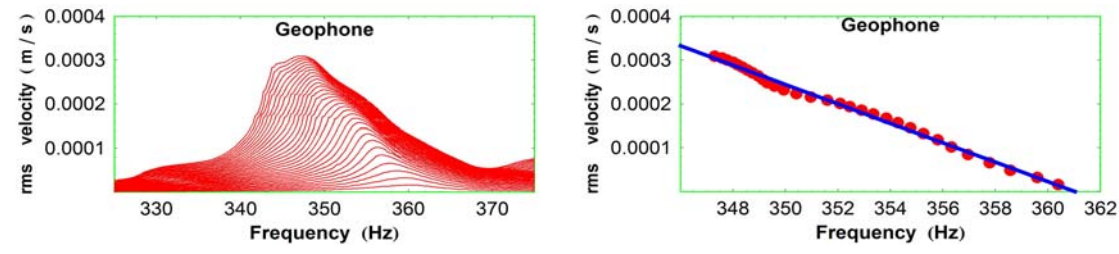
Figure C-5
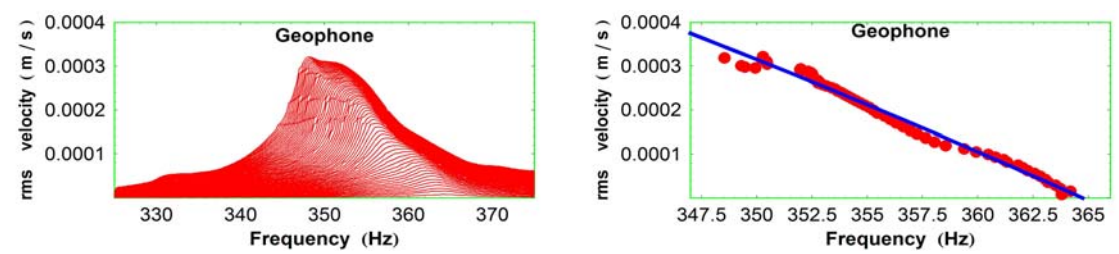
Figure C-6
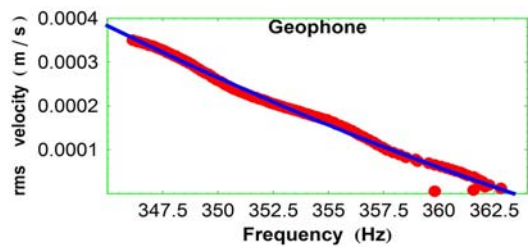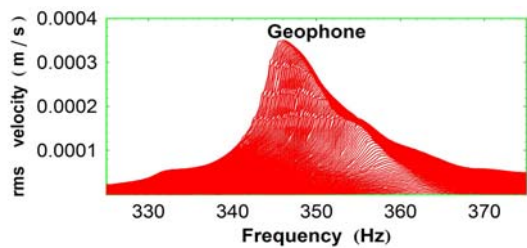
Figure C-7
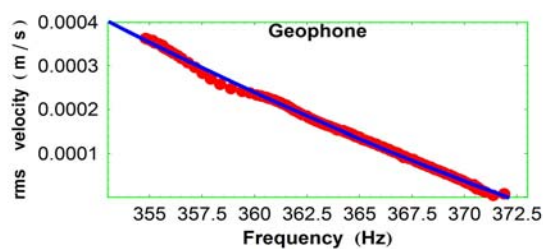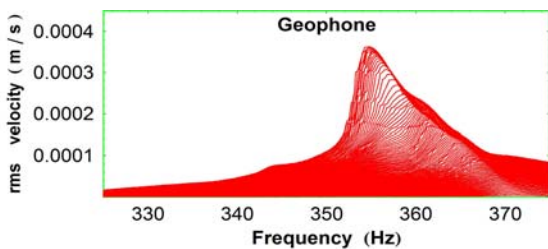
Figure C-8
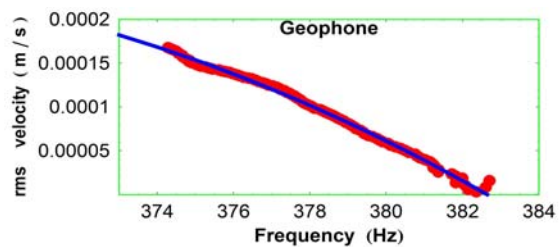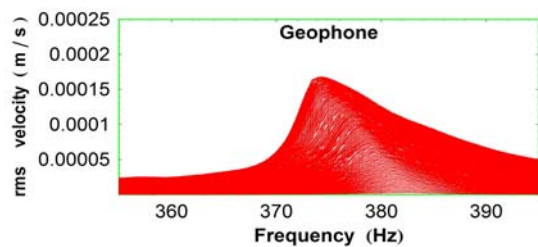
Figure C-9
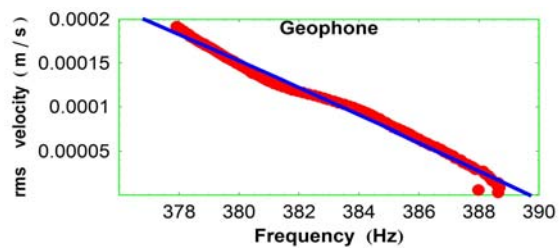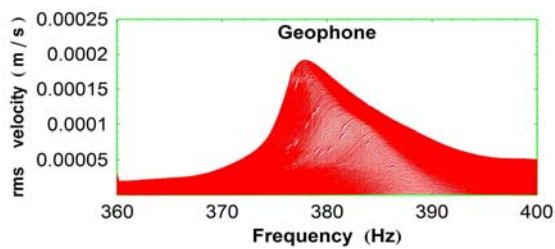
Figure C-10
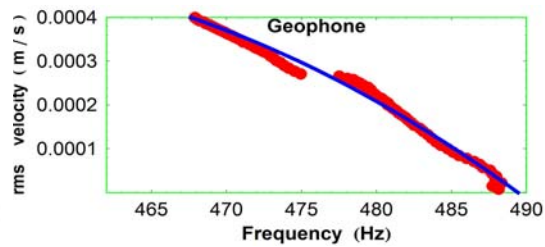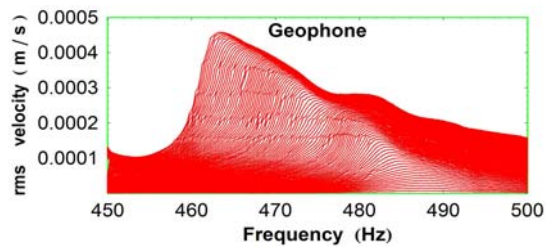
Table 2 – Sound speed equations, spring constants, and yield forces for the different nonlinear acoustic landmine detection experimental apparatuses

Figure	Sound Speed Equation	Spring Constant (10^6 N/m)	Yield Force (N)
C-1	u = (8.9 ± 0.3) mm/s – (25.2 ± 0.7) μm*f	6.0 ± 0.1	3.0 ± 0.1
C-2	u = (8.73 ± 0.08) mm/s – (24.5 ± 0.2) μm *f	6.0 ± 0.1	3.02 ± 0.05
C-3	u = (8.2 ± 0.1) mm/s – (22.8 ± 0.3) μm *f	6.1 ± 0.1	2.84 ± 0.06
C-4	u = (8.0 ± 0.1) mm/s – (22.1 ± 0.3) μm *f	6.1 ± 0.1	2.77 ± 0.06
C-5	u = (7.8 ± 0.1) mm/s – (21.3 ± 0.4) μm *f	6.3 ± 0.1	2.75 ± 0.07
C-6	u = (7.56 ± 0.06) mm/s – (20.8 ± 0.2) μm *f	6.2 ± 0.1	2.66 ± 0.05
C-7	u = (7.78 ± 0.05) mm/s – (20.9 ± 0.1) μm *f	6.6 ± 0.1	2.84 ± 0.05
C-8	u = (7.42 ± 0.07) mm/s – (19.4 ± 0.2) μm *f	7.0 ± 0.1	2.72 ± 0.05
C-9	u = (6.07 ± 0.06) mm/s – (15.6 ± 0.2) μm *f	7.2 ± 0.1	2.26 ± 0.04
C-10	u = (8.3 ± 0.1) mm/s – (16.8 ± 0.3) mm *f	11.4 ± 0.1	3.96 ± 0.08

Appendix D - Presiach-Mayergoyz Formalism

The Preisach-Mayergoyz (PM) formalism was first developed in the context of ferromagnetism and later extended to any phenomenological situation which can be described by an input-output equation of state. That is, the equation of state must contain a transfer function that converts any given input to a corresponding output. For example,

$$B = \rho(A)$$

where ρ is the transfer function converting A into B.
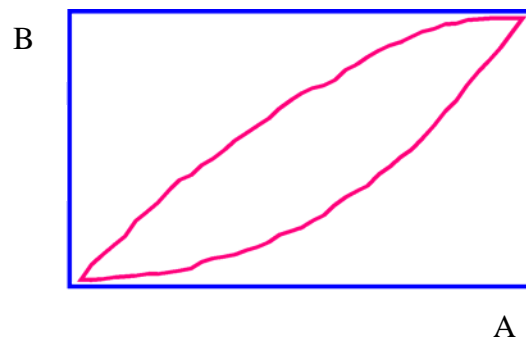
Figure 63 – Generic hysteresis loop

If A and B both vary in time, a plot of B versus A will yield a hysteresis loop like that seen in Figure 63. By varying the complexity of ρ, the PM formalism can be used to reproduce every possible hysteretic curve.
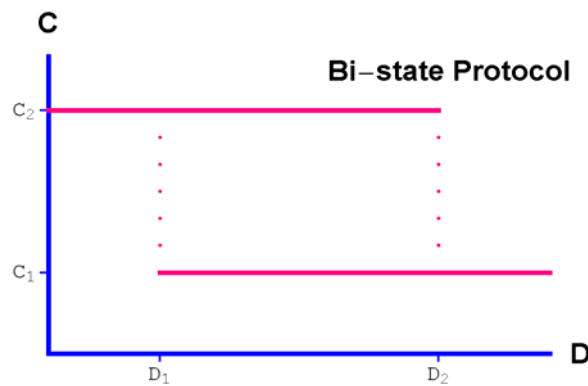
Figure 64 – Generic bi-state protocol

The constraints upon the equation of state required by the PM formalism mandate a bi-state protocol as shown in Figure 64. Depending on the value of an externally applied control variable, D, any particular subcomponent will be in one of two states: the active state, C_2, or the inactive state, C_1. While every subcomponent in a sample must obey the same general bi-state protocol, it is not necessary that they each be governed by the same threshold values, D_1 and D_2. That is, each subcomponent may be triggered on or off by different values of the external control component. These "on-off" values define the protocol for a specific subcomponent and are plotted as ordered pairs in a PM-space (see Figure 65). Since $D_1 < D_2$ the possible states are actually restricted to a half-space.
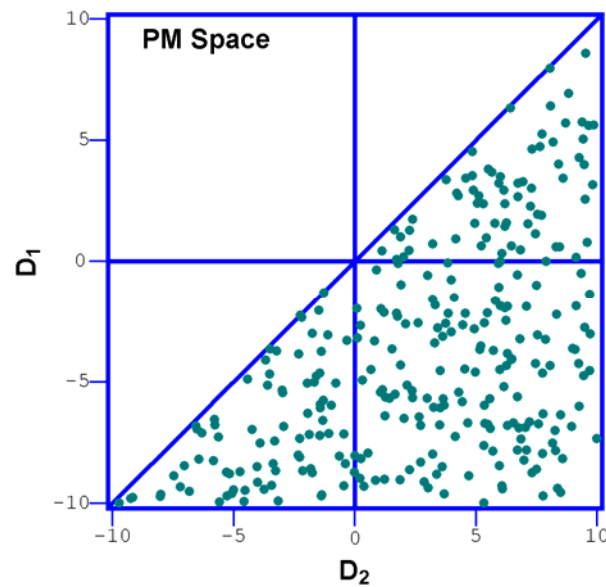
Figure 65 – Random distribution in a generic Presiach-Mayergoyz space

Macroscopic behavior results from the aggregate behavior of each subcomponent in response to an external control. In the PM formalism, it is assumed that the universal control uniformly influences every subcomponent within a sample. As each subcomponent has a unique protocol, whether or not it is active depends upon both the value of the control as well as the

history of the system. For a random sample, such as that depicted in Figure 65, the initial states of each subcomponent are unknown.

As D changes, the number of active elements changes. This evolution is depicted graphically in the PM space, as shown in Figure 66. Increasing the magnitude of the control D corresponds to positive movement along the horizontal axis, as shown in Figure 66a. At an arbitrary value D_{max}, all the subcomponents to the left of the vertical line have been driven into the C_1 state. The states of those subcomponents to the right of D_{max} remain unknown. If D_{max} is pushed to the rightmost value of the PM space as in Figure 66b, then all the subcomponents are driven into state C_2. Having conditioned the sample in this manner, if D is reduced (represented by a negative movement along the vertical axis) only those components above D_{max} are returned to the C_1 state. Thus, it is apparent that a conditioned sample oscillating between two values of D will only have a triangular active region as shown in Figure 66c. The subcomponents within this region will change state depending upon the value of the varying control, while those outside the triangle remain constantly in one of the two possible states. Oscillations between different values of the control will produce differently sized active regions (Figure 66d).
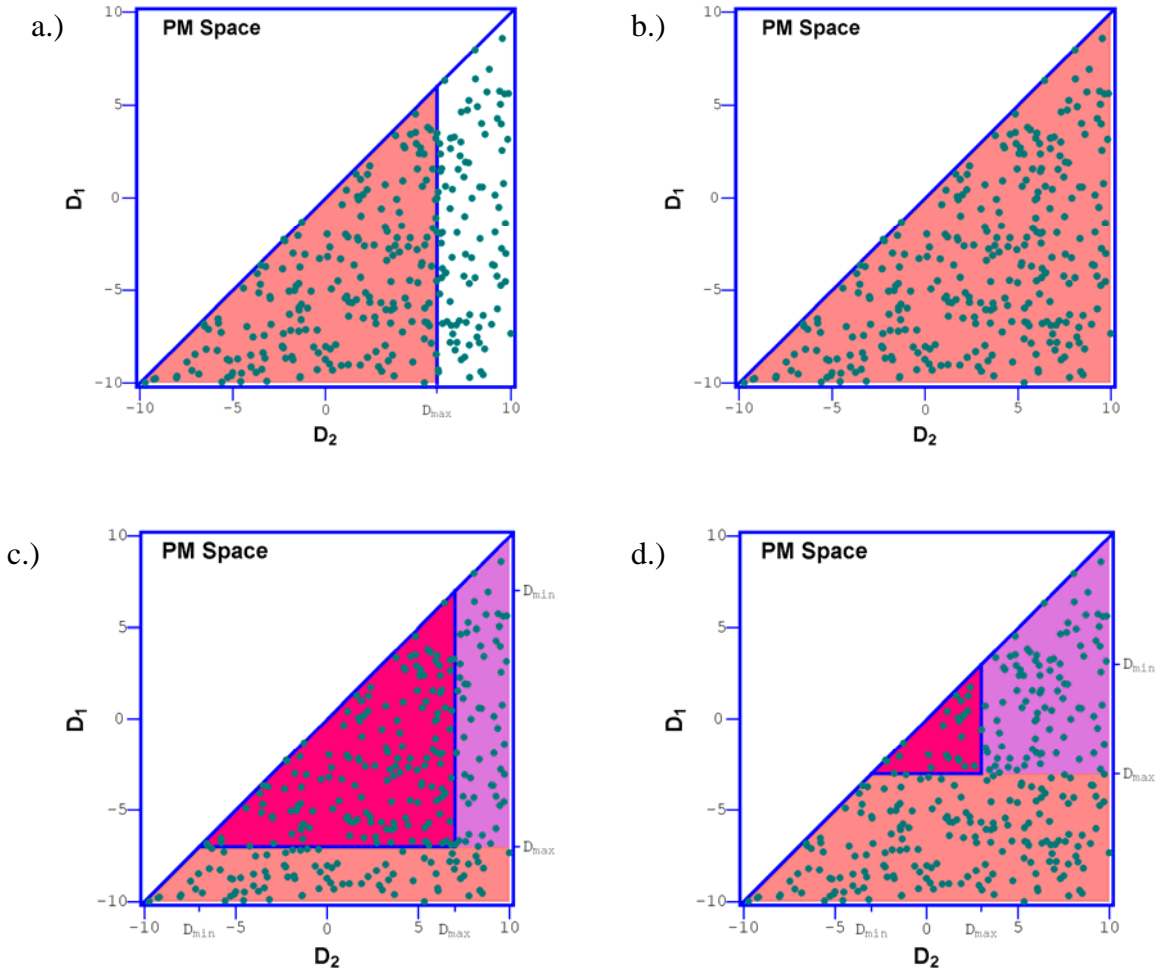
Figure 66 – Evolution of a random PM space. a.) The control variable *D* is changed to an arbitrary value *D*_{max}. b.) The sample is fully conditioned. c.) The values enclosed by the triangle are in the active region as *D* oscillates between *D*_{min} and *D*_{max}. d.) A smaller range of *D* yields a smaller active region.

For a ferromagnetic sample, such as that depicted in Figure 67, the control component is an externally applied magnetic field, H. The bi-state condition for any given subcomponent in a sample is the magnetization, M, and is shown in Figure 68. Magnetization is the dipole moment density in a sample, so M for any particular subcomponent can be thought of as either spin up or spin down ($M_\uparrow$ and $M_\downarrow$, respectively).
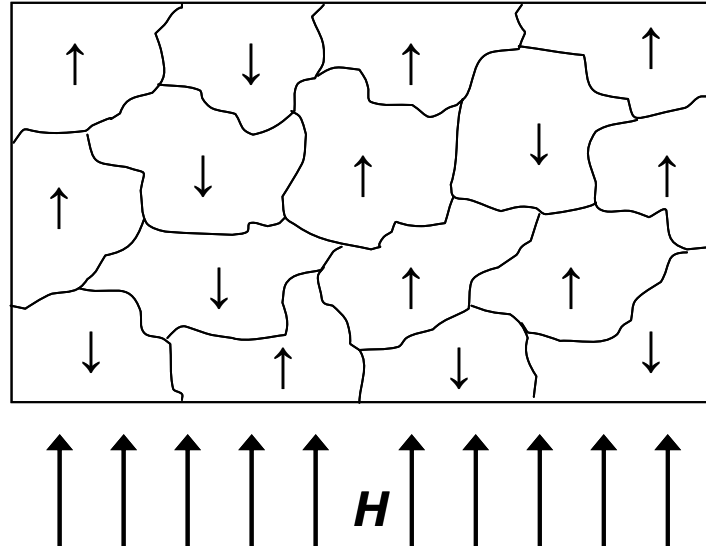
Figure 67 – Ferromagnetic specimen subjected to an external *H*-field.
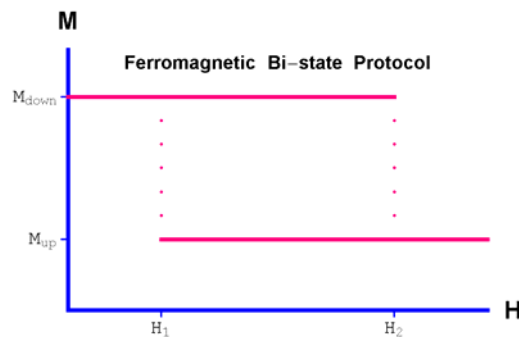
Figure 68 – Ferromagnetic bi-state protocol

The motivation for the ferromagnetic bi-state protocol arises from internal energy considerations.   Internal energy is defined as

Equation 60

$$U_M = -\vec{M} \bullet \vec{H}$$

which is a double-welled potential because *M* has two possible states (up or down). In Figure 69a potential curve is depicted for an arbitrary *H*. Despite being double-valued, the magnetization will behave so as to ensure that the overall potential energy resides in the lower of the two ground states.
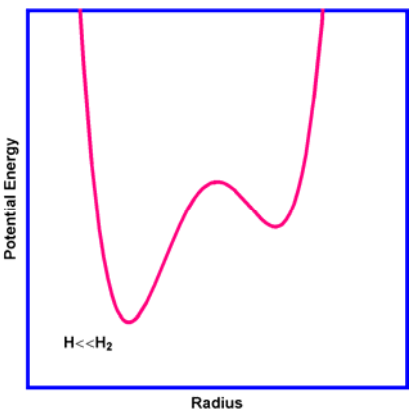
Figure 69- Double-well potential for a ferromagnetic domain when *H* is much less than the threshold value.

Each *H* will yield a different potential, but as *H* approaches a threshold value, the potential wells become progressively shallower. When *H* finally passes through its threshold, the potential will become instantaneously single-valued and will then return to its double-valued condition. After the transition, though, the original state will no longer be the lowest energy ground state. Thus, the subcomponent is forced to change from one state to the next. This progression is shown in Figure 70.
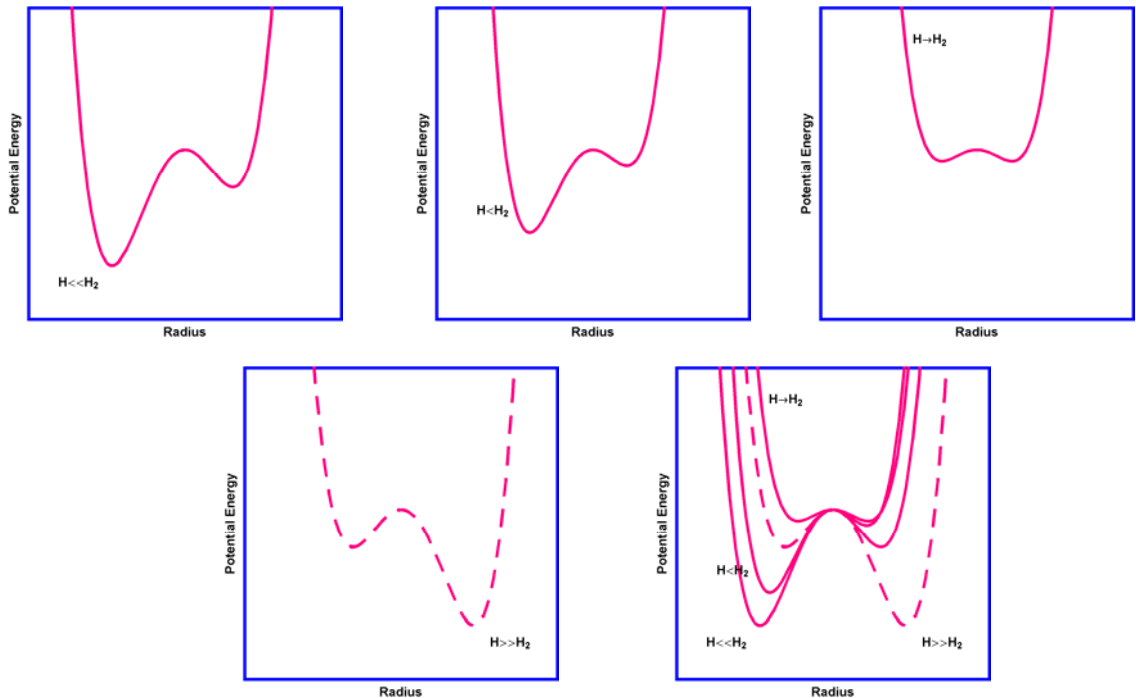
Figure 70 – Potential wells for varying values of *H*.

Energy considerations resulting from the externally applied H-field are the primary cause of state transitions, but they are not the only possible transition mechanism. It is also possible for such transitions to be induced thermally. It is certainly more probable for a subcomponent to exist in the lowest energy ground state, but thermal effects can cause a jump from a lower energy state to a higher one. As H approaches the threshold value, the probability of thermally induced transitions rises even further because the barrier potential and the energy differential between the wells both decrease. This probabilistic effect is depicted by the arrows in Figure 71.
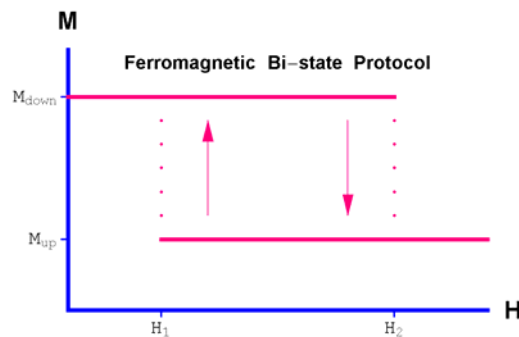
Figure 71 – Ferromagnetic bi-state protocol with thermally induced transitions

In summary, from its birth as a tool used to explain hysteresis effects in ferromagnets, the PM space has evolved into a statistical formulation capable of describing the macroscopic hysteretic behavior of any system using a distribution of constituent bi-state protocols. The phenomenological mesoscopic elastic behavior observed in geomaterials has been effectively simulated by Scalerandi *et al.*[6]

Appendix E - Wave Propagation on a Clamped Plate

An acoustic pressure wave causes longitudinal displacement of particles as it propagates through a medium. If a sound wave is normally incident upon a solid lattice structure that is constrained by some set of boundary conditions, the molecules in the solid can be thought of as moving transversely with respect to the boundaries as they are acoustically excited.

To model this situation in a 1-D case, the classic transverse wave on a string problem is considered as shown in Figure 72.
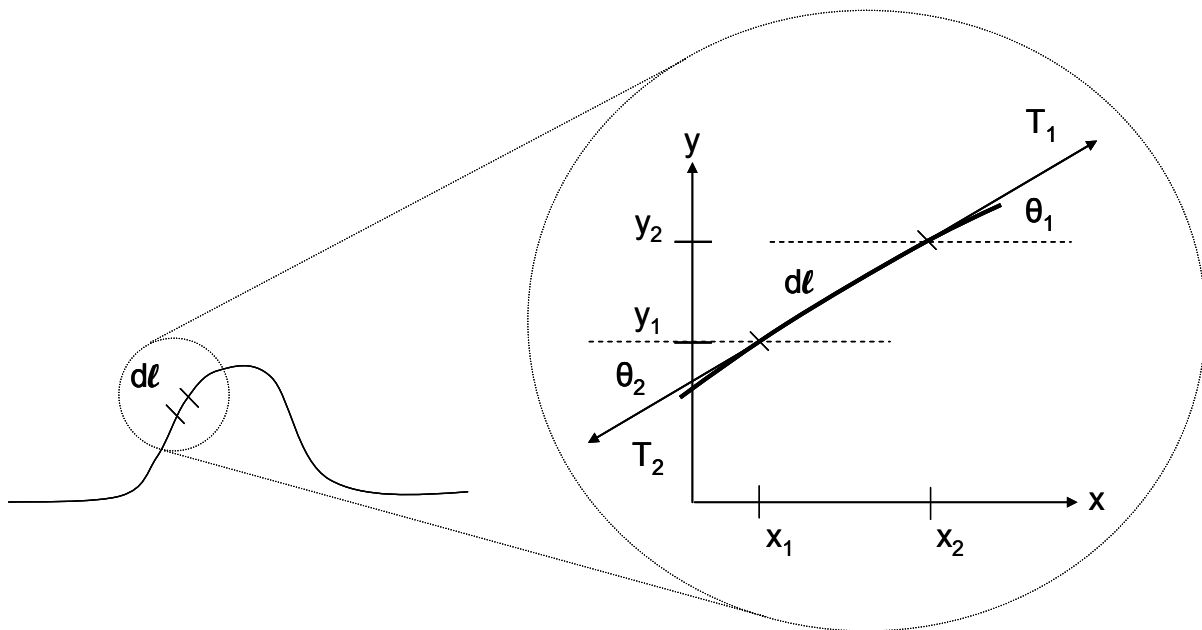
Figure 72 – Wave pulse on a string.

For simplicity's sake, the following approximations are made:

$$dy << dx \quad \therefore \quad mass_{d\ell} = m_{d\ell} = \mu(d\ell) \approx \mu(dx)$$

$$T_1 \approx T_2 \approx T$$

$$\sin \theta \approx \theta$$

$$\tan \theta \approx \frac{dy}{dx}$$

According to Newton's second law,

$$\Sigma F_y = m_{d\ell} a_y$$

$$T_2 \sin \theta_2 - T_1 \sin \theta_2 = m_{d\ell} \frac{d^2 y}{dt^2}$$

$$T_2 \theta_2 - T_1 \theta_2 \cong \mu (x_2 - x_1) \frac{d^2 y}{dt^2}$$

$$T \left(\frac{\theta_2 - \theta_1}{x_2 - x_1} \right) = \mu \frac{d^2 y}{dt^2}$$

$$T \frac{d\theta}{dx} = \mu \frac{d^2 y}{dt^2}$$

$$T \frac{d}{dx} \left(\frac{dy}{dx} \right) = \mu \frac{d^2 y}{dt^2}$$

$$\frac{d^2 y}{dx^2} - \frac{\mu}{T} \frac{d^2 y}{dt^2} = 0$$

Equation 61

Noting the following definition for the speed of a traveling wave

$$c \equiv \sqrt{\frac{T}{\mu}}$$

Equation 61 takes the well-known form of the wave equation

$$\frac{d^2 y}{dx^2} - \frac{1}{c^2} \frac{d^2 y}{dt^2} = 0$$

Equation 62

whose general solution containing waves traveling in both the *+x* and *-x* directions is

$$y(x,t) = f(x + ct) + g(x - ct)$$

Equation 63

Advancing on to the 2-D case, the string can be replaced by a membrane and linear tension per

unit length becomes surface tension per unit length, $\tilde{T}$.
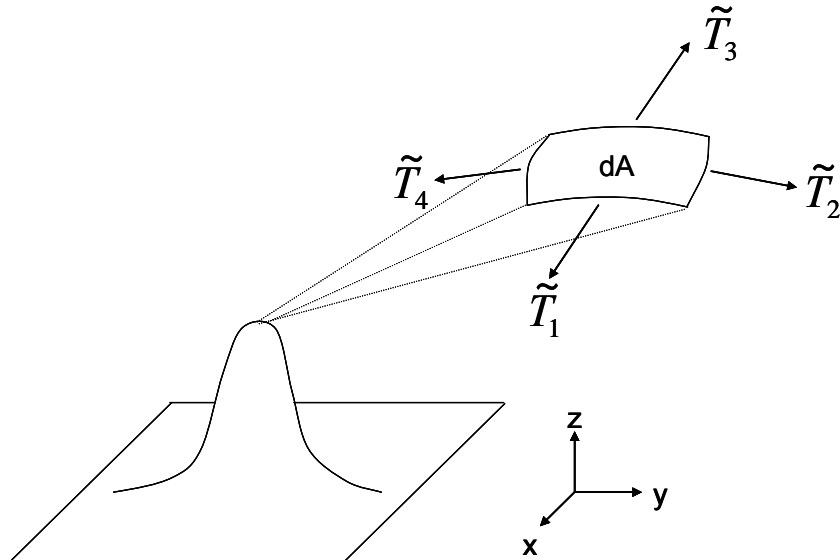
Figure 73 – Wave pulse on a membrane.

Again, because the surface area patch is assumed to infinitesimally small, the following

approximations holds true

$$mass_{dA} = m_{dA} = \sigma dx dy \approx \sigma \Delta x \Delta y$$

$$\tilde{T}_1 = \tilde{T}_2 = \tilde{T}_3 = \tilde{T}_4 \approx \tilde{T}$$

The normal direction is now defined by the z-axis. Application of Newton's second law in this

coordinate plane yields

$$\Sigma F_x = m_{dA} a_z$$

$$\left(\tilde{T}_2\theta_2 - \tilde{T}_1\theta_1\right)(\Delta x) + \left(\tilde{T}_4\theta_4 - \tilde{T}_3\theta_3\right)(\Delta y) = m_{dA}\frac{\partial^2 z}{\partial t^2}$$

$$\tilde{T}\left(\theta_2 - \theta_1\right)(\Delta x) + \tilde{T}\left(\theta_4 - \theta_3\right)(\Delta y) = m_{dA}\frac{\partial^2 z}{\partial t^2}$$

$$\tilde{T}\left(\theta_2 - \theta_1\right)(\Delta x) + \tilde{T}\left(\theta_4 - \theta_3\right)(\Delta y) = \left(\sigma \Delta x \Delta y\right)\frac{\partial^2 z}{\partial t^2}$$

$$\tilde{T}\left(\frac{\theta_2 - \theta_1}{\Delta y}\right) + \tilde{T}\left(\frac{\theta_4 - \theta_3}{\Delta x}\right) = \sigma \frac{\partial^2 z}{\partial t^2}$$

$$\tilde{T}\frac{\partial \theta}{\partial y} + \tilde{T}\frac{\partial \theta}{\partial x} = \sigma \frac{\partial^2 z}{\partial t^2}$$

$$\tilde{T}\frac{\partial}{\partial y}\left(\frac{\partial z}{\partial y}\right) + \tilde{T}\frac{\partial}{\partial x}\left(\frac{\partial z}{\partial x}\right) = \sigma \frac{\partial^2 z}{\partial t^2}$$

$$\tilde{T}\left(\frac{\partial^2 z}{\partial y} + \frac{\partial^2 z}{\partial x}\right) = \sigma \frac{\partial^2 z}{\partial t^2}$$

$$\tilde{T}\nabla^2 z = \sigma \frac{\partial^2 z}{\partial t^2}$$

$$\nabla^2 z - \frac{\sigma}{\tilde{T}}\frac{\partial^2 z}{\partial t^2} = 0$$

Equation 64

For the 2-D case the sound speed in the medium takes on the following definition

$$c \equiv \sqrt{\frac{\tilde{T}}{\sigma}}$$

and the familiar 2-D wave equation results

$$\nabla^2 z - \frac{1}{c^2}\frac{\partial^2 z}{\partial t^2} = 0$$

Equation 65

The wave on a membrane problem becomes slightly more complex if an external driving force is introduced into the system.
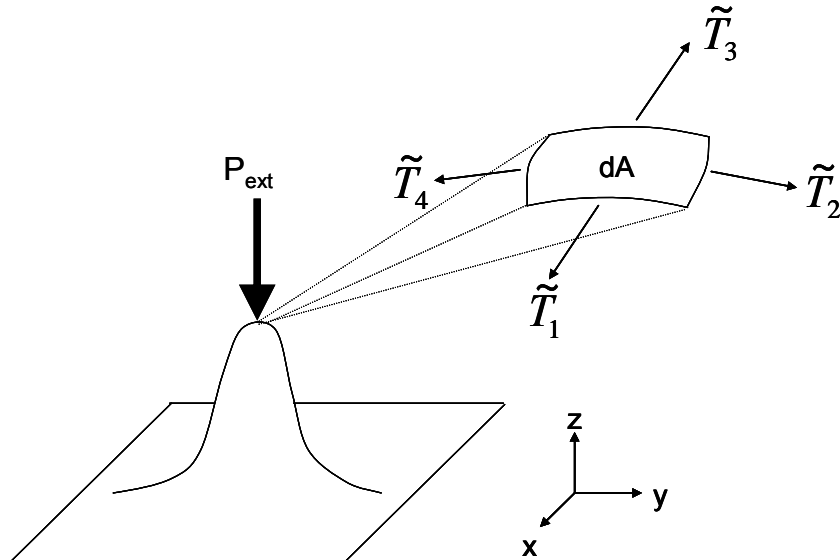
Figure 74 – Wave pulse on a membrane subjected to an external driving force.

Newton's second law must now account for this additional force, which is assumed to be normally incident upon the membrane.

$$\Sigma F_z = \Sigma F_{z,no\ pressure} + Pdxdy = m_{dA}a_z$$

Reworking the problem with this slight perturbation produces a new wave equation

$$\nabla^2 z - \frac{\sigma}{\tilde{T}} \frac{\partial^2 z}{\partial t^2} = -\frac{P}{\tilde{T}}$$

If the membrane is assumed to be circular in nature and the external force acts at the center of the membrane, then the wave equation will be devoid of angular dependence. Expanding the gradient in polar coordinates while neglecting angular dependence clearly shows that the solution to the wave equation will be solely a function of the radial distance from the center of the membrane, r.

$$\left(\frac{\partial^2}{\partial r^2} + \frac{1}{r}\frac{\partial}{\partial r} \right) z - \frac{\sigma}{\tilde{T}} \frac{\partial^2 z}{\partial t^2} = -\frac{P}{\tilde{T}}$$

Developing the actual wave equation with the classical methods used above for a thin, circular, elastic clamped plate is considerably more daunting than either of the previous examples.
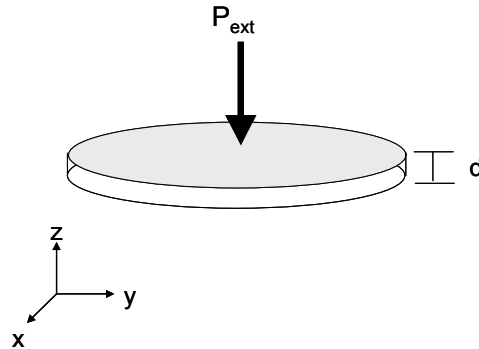
Figure 75 – Clamped plate subjected to external driving force

However, the equation for a clamped plate transducer as seen in Figure 75 is derived by Mason[15] to be

$$\frac{Ed^3}{12\left(1-\sigma^2\right)}\nabla^4 w - P + d\rho\frac{\partial^2 w}{\partial t^2} = 0$$

Equation 66

$P = P_0 e^{j\omega t} = \text{driving acoustic pressure}$

$\rho = \text{plate density}$

$d = \text{plate thickness}$

$\omega = \text{natural resonant frequency of the clamped plate}$

$\sigma = \text{Poisson's ratio}$

$E = \text{Young's (elastic) modulus}$

$k = \left(\frac{12\rho\omega^2\left(1-\sigma^2\right)}{Ed^2}\right)^{1/4} = \text{wave number}$

Noting the definition for k, it can be shown that Equation 66 can be algebraically manipulated to yield

$$\nabla^2 \nabla^2 w - k^4 w - P\left[\frac{12\left(1-\sigma^2\right)}{Ed^3}\right] = 0$$

The first two terms of Equation 67 are a difference of squares, so

$$\left[\left(\nabla^2 + k^2\right)\left(\nabla^2 - k^2\right)\right]w - P\left[\frac{12\left(1-\sigma^2\right)}{Ed^3}\right] = 0$$

Rewriting the gradient terms of Equation 68 in radial form and neglecting angular dependence because the plate is assumed to circularly clamped

$$\left[\left(\frac{\partial^2}{\partial r^2} + \frac{1}{r}\frac{\partial}{\partial r} + k^2\right)\left(\frac{\partial^2}{\partial r^2} + \frac{1}{r}\frac{\partial}{\partial r} - k^2\right)\right]w - P\left[\frac{12\left(1-\sigma^2\right)}{Ed^3}\right] = 0$$

In this treatment, the plate is driven by a uniform pressure and is assumed to have circular symmetry. Thus, it is expected that the solution to the wave equation should be a linear combination of real and imaginary zeroth order Bessel functions of the first and second kind.

$$w_{\text{hom}\,ogenous} = AJ_0(kr) + BJ_0(jkr) + CY_0(kr) + DY_0(jkr)$$

However, $Y_0(kr)$ and $Y_0(jkr)$ become infinite as r approaches zero, so physical constraints demand that C and D equal zero for the circular plate. Note that if the circular plate were actually annular this constraint would not exist. The homogenous solution for the circular plate then becomes

$$w_{\text{hom}\,ogenous} = AJ_0(kr) + BJ_0(jkr)$$

$$w_{\text{hom}\,ogenous} = AJ_0(kr) + BI_0(kr), \quad I_0(kr) \equiv J_0(jkr)$$

If Equation 68, the equation of motion, is in fact true, then there must also exist a constant particular solution.

$$w_{particular} = \xi$$

$$\left[\left(\nabla^2 + k^2\right)\left(\nabla^2 - k^2\right)\right]\xi = P\left[\frac{12\left(1-\sigma^2\right)}{Ed^3}\right]$$

$$-k^4\xi = P\left[\frac{12\left(1-\sigma^2\right)}{Ed^3}\right]$$

$$\xi = -P\left[\frac{12\left(1-\sigma^2\right)}{Ed^3 k^4}\right]$$

$$\xi = -P\left[\frac{12\left(1-\sigma^2\right)}{Ed^3 k}\right]\left[\frac{1}{\left(\frac{12\rho\omega^2\left(1-\sigma^2\right)}{Ed^2}\right)}\right]$$

$$\xi = -\frac{P}{\rho d\omega^2}$$

Equation 70

The general solution of the equation of motion is a linear combination of the homogenous and particular solutions.

$$w = w_{general} = w_{\hom ogenous} + w_{particular}$$

$$w = AJ_0(kr) + BI_0(kr) - \frac{P}{\rho d\omega^2}$$

Equation 71

Since the plate is circularly clamped, it must obey the following boundary conditions when r is equal to the clamped radius, a.

$$w(r = a) = 0$$

$$\left.\frac{\partial w}{\partial r}\right|_{r=a} = 0$$

Applying the first condition to Equation 71

$$w(r = a) = AJ_0(ka) + BI_0(ka) - \frac{P}{\rho d\omega^2} = 0$$

<div align="right">**Equation 72**</div>

In order to apply the second boundary condition, it must be recalled that

$$\frac{\partial}{\partial r} J_n(r) = -J_{n+1}(r)$$

$$\frac{\partial}{\partial r} I_n(r) = I_{n+1}(r)$$

Invoking the second boundary condition,

$$\frac{\partial w}{\partial r} = -AJ_1(kr) + BI_1(kr)$$

$$\left.\frac{\partial w}{\partial r}\right|_{r=a} = -AJ_1(ka) + BI_1(ka) = 0$$

<div align="right">**Equation 73**</div>

Equation 72 and Equation 73 now form a system of equations that can be used to determine the coefficients A and B.

$$A = \left[\frac{I_1(ka)}{J_0(ka)I_0(ka) + J_1(ka)I_0(ka)}\right]\left(\frac{P}{\rho d\omega^2}\right)$$

<div align="right">**Equation 74**</div>

$$B = \left[\frac{J_1(ka)}{J_0(ka)I_0(ka) + J_1(ka)I_0(ka)}\right]\left(\frac{P}{\rho d\omega^2}\right)$$

<div align="right">**Equation 75**</div>

The general solution for a clamped plate is then

$$w = \left[\frac{J_0(ka)I_1(ka)}{J_0(ka)I_0(ka) + J_1(ka)I_0(ka)} \right]\left(\frac{P}{\rho d\omega^2} \right) + \left[\frac{J_1(ka)I_0(kr)}{J_0(ka)I_0(ka) + J_1(ka)I_0(ka)} \right]\left(\frac{P}{\rho d\omega^2} \right) - \frac{P}{\rho d\omega^2}$$

$$w(r) = \frac{P}{\rho d\omega^2}\left[\left(\frac{J_0(ka)I_1(ka) + J_1(ka)I_0(kr)}{J_0(ka)I_0(ka) + J_1(ka)I_0(ka)} \right) - 1 \right]$$

Equation 76

The lowest resonant frequency of this oscillating plate occurs when $ka = 3.20$. A plot of this

single peaked mode shape is shown in standard acoustics texts.

Appendix F - Automated Detection Algorithms and LabVIEW®

The integration of an external control system into the experimental setup was realized for the first time in the buried-simulant setup with far-reaching benefits. In addition to being a pragmatic necessity for actual mine clearance operations, the self-sustaining nature of the setup has enabled prolonged, high-resolution data sets to be gathered. A self-designed LabVIEW® program regulates the entire experimental process. The host personal computer is connected to the Agilent spectrum analyzer via an IEEE 488.2 National Instruments card and HP-GPIB cable. The flow of information over the GPIB interface is two-way – control commands are sent to the spectrum analyzer and data is saved directly to the host computer's hard drive. The movement commands that physically enable the scanning procedure are sent to the two NF90 motor controllers via RS-232 serial ports.

The LabVIEW® interface for conducting a two-dimensional profile of a buried mine or mine simulant is shown in Figure 76 on the following page. The front panel requires a variety of user inputs. These include:

- start frequency of the sweep (*Start Frequency (Hz)*)
- stop frequency of the sweep (*Stop Frequency (Hz)*)
- initial source level (*Source Level (mV)*)
- magnitude by which to increase the source level (*Amplitude Increment (mV)*)
- number of sweeps to perform at each scan position (*Sweeps per Location*)
- the dimensions of the grid to be scanned (*Initial X-axis Motor Index* and *Initial Y-axis Motor Index*)
- the number of scan positions in each direction (*X-axis Increments* and *Y-axis Increments*)

The actual LabVIEW® code is graphical in nature. Sample code which conducts a single frequency sweep and saves the tuning curves to file is shown in Figure 77.
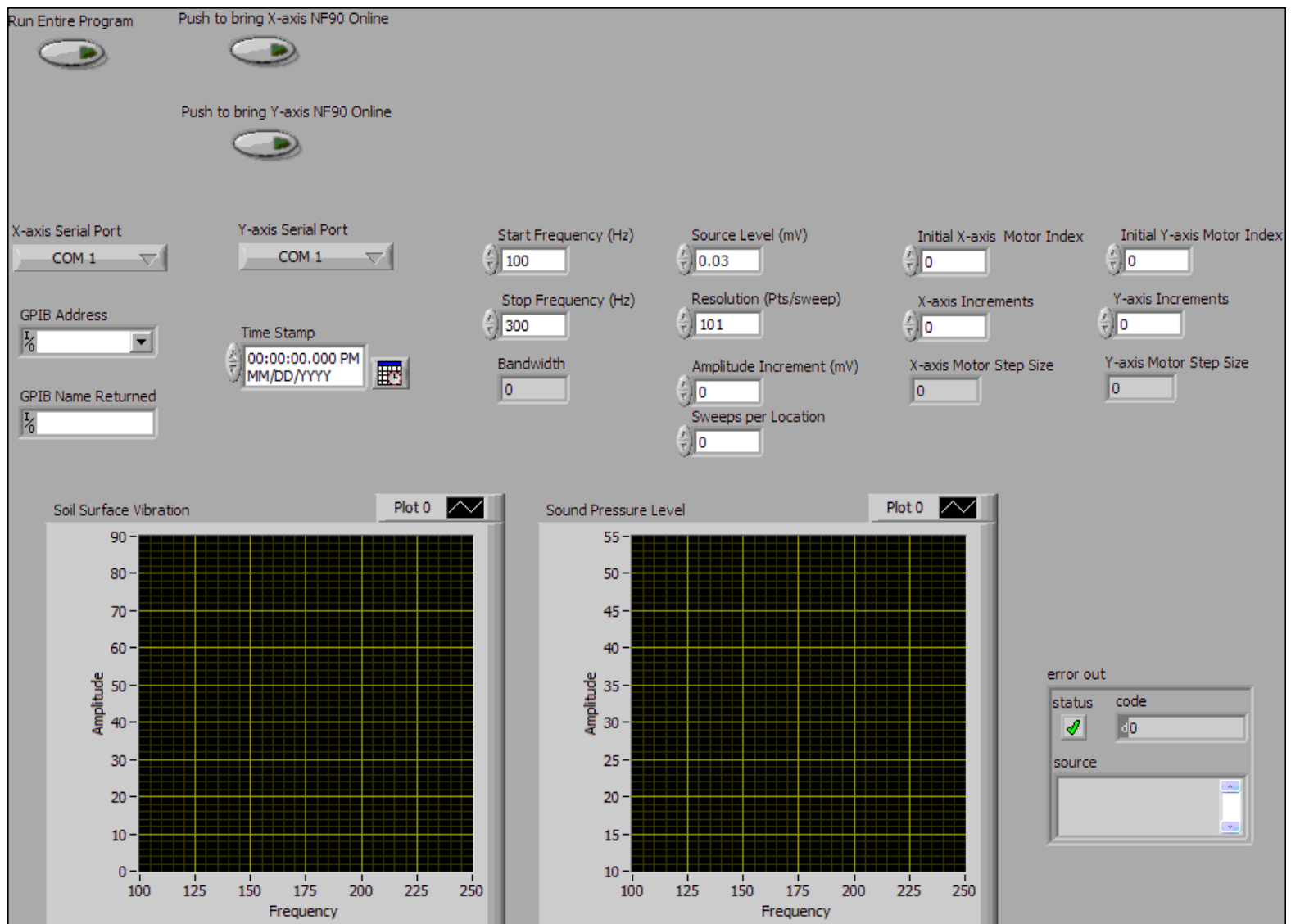
Figure 76 – LabVIEW® front panel for the 2-D mine sweeping experiment
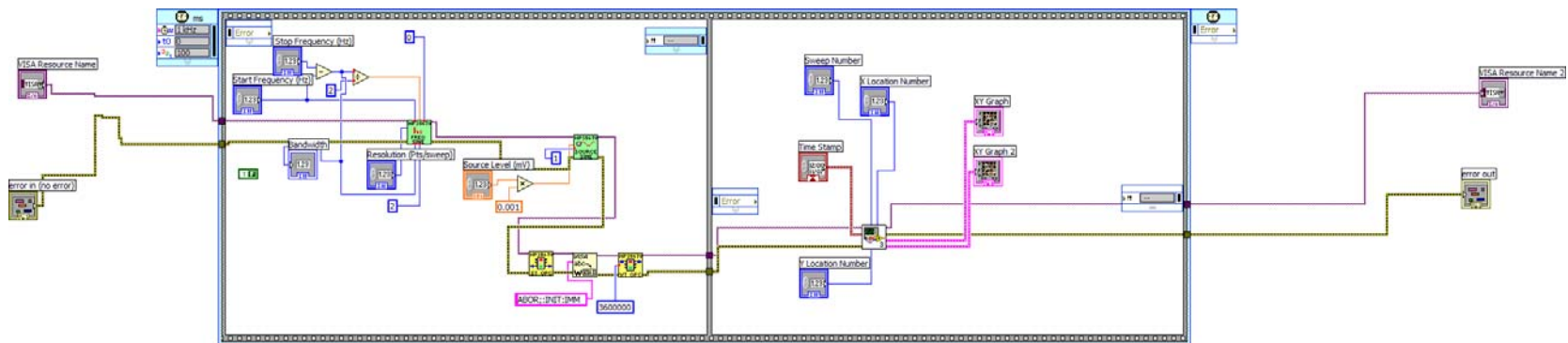
Figure 77 – LabVIEW® circuit diagram to conduct a frequency sweep and save the tuning curve to file.

The graphical programming environment of LabVIEW® is relatively difficult to present in its entirety, as each virtual instrument is often a multi-layered combination of several sub-virtual instruments. The general algorithm for conducting a nonlinear scan of the buried mine simulant is given in Figure 78.
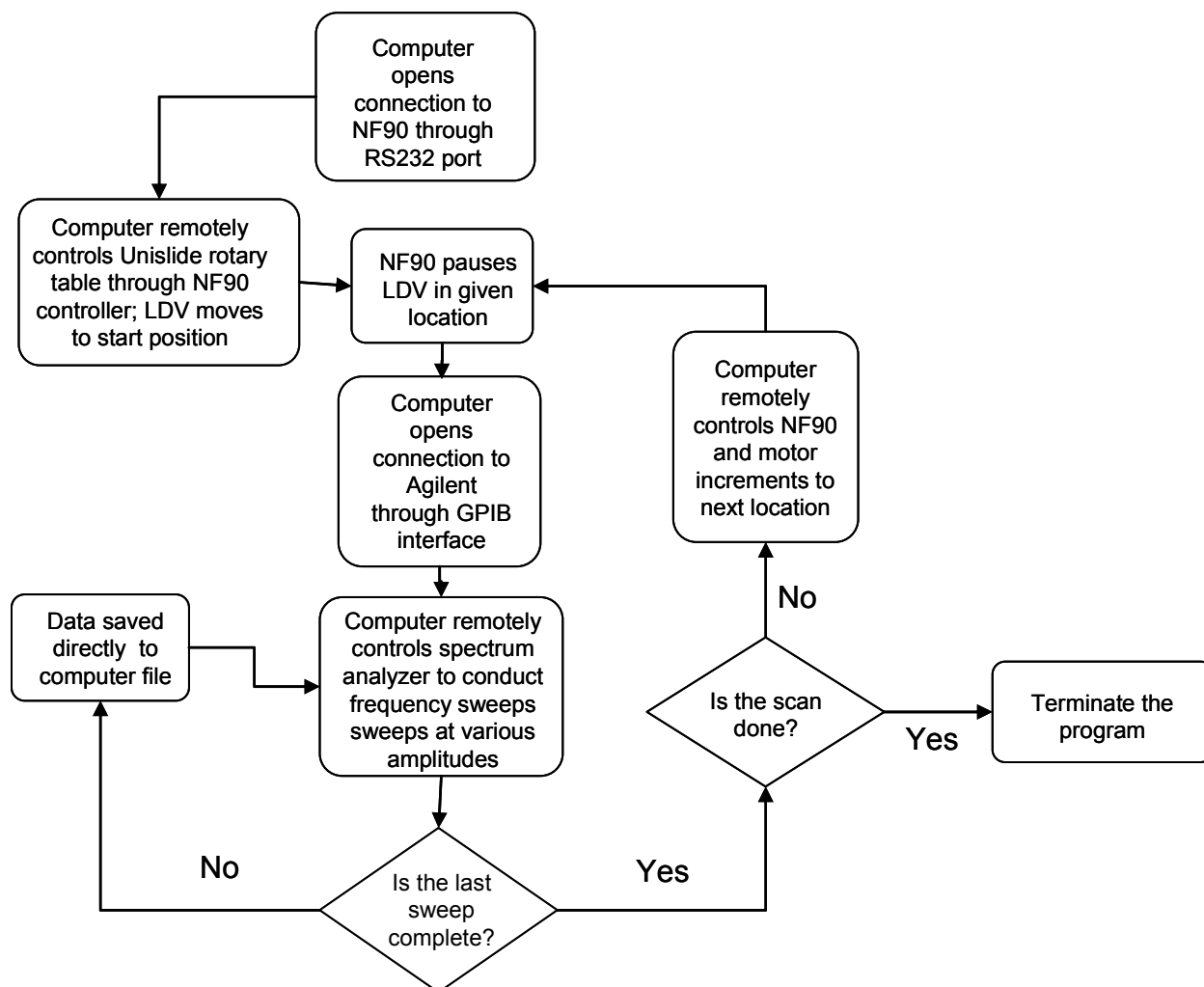
Figure 78 – Flowchart of LDV motor control and Agilent spectrum analyzer algorithm for an automated scan across a soil box.

Appendix G - Buried Acrylic Simulant: Resonant Tuning Curves and Backbone Curves

Figure G-1 $x = -15\,cm$
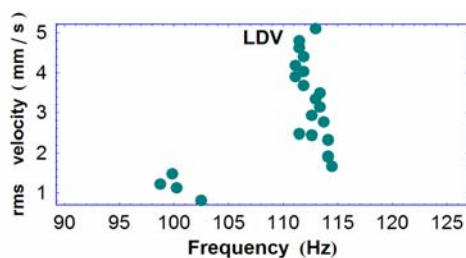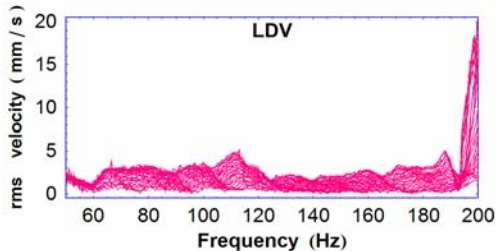
Figure G-2 $x = -14\,cm$
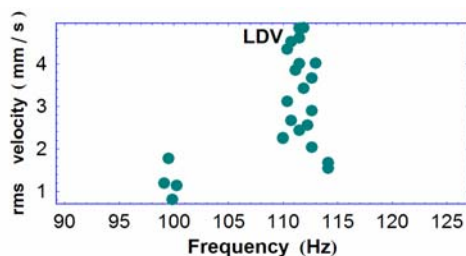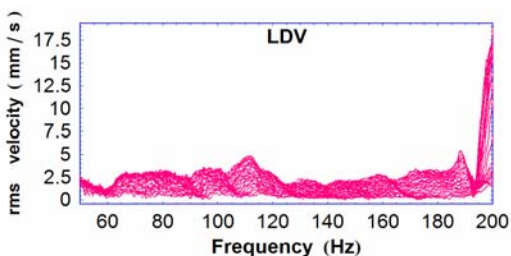
Figure G-3 $x = -13\,cm$
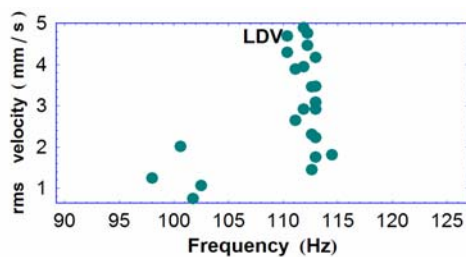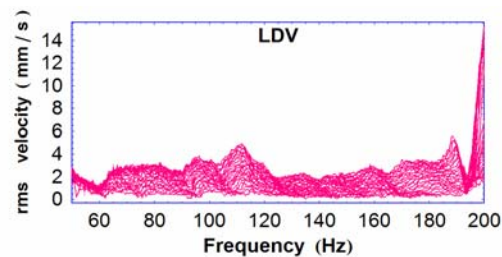
Figure G-4 $x = -12\,cm$
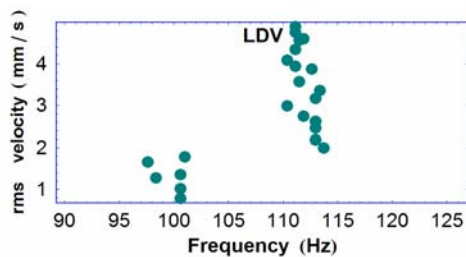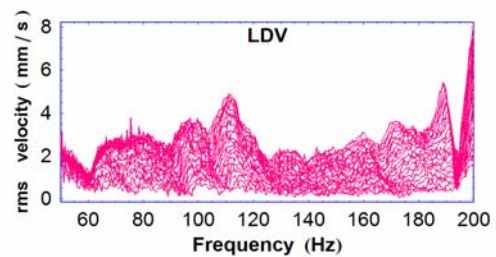
Figure G-5 $x = -11\,cm$
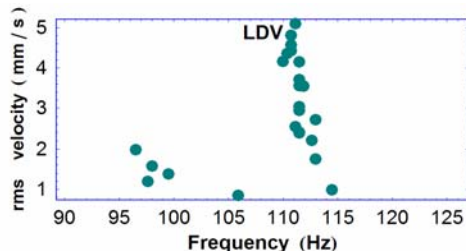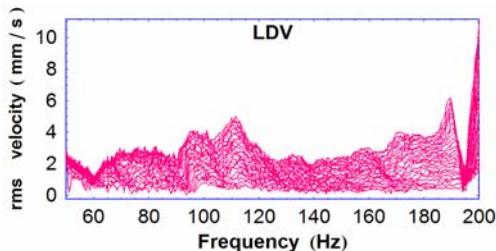
Figure G-6　　　　　　　　$x = -10\ cm$
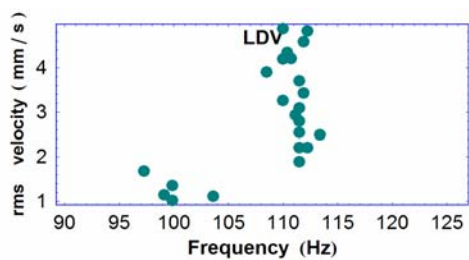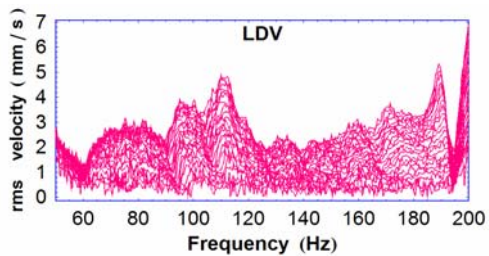
Figure G-7　　　　　　　　$x = -9\ cm$
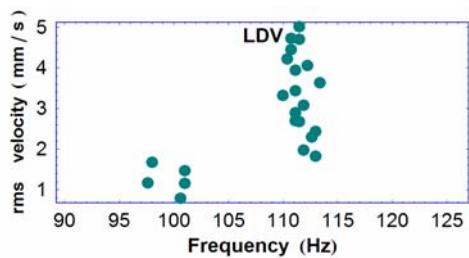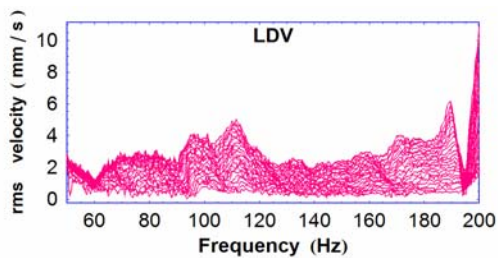
Figure G-8　　　　　　　　$x = -8\ cm$
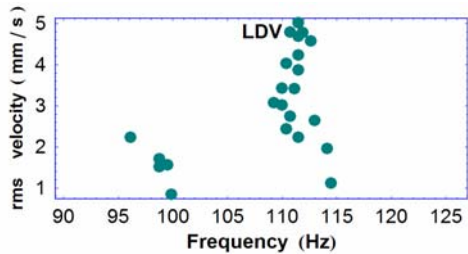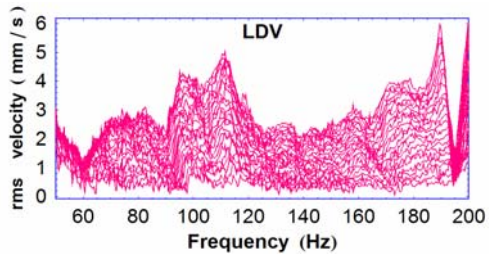
Figure G-9　　　　　　　　$x = -7\ cm$
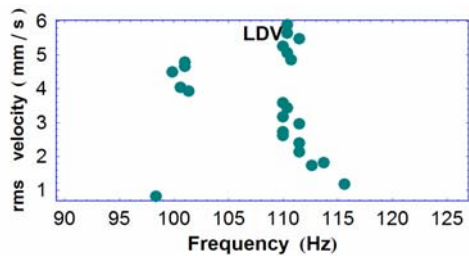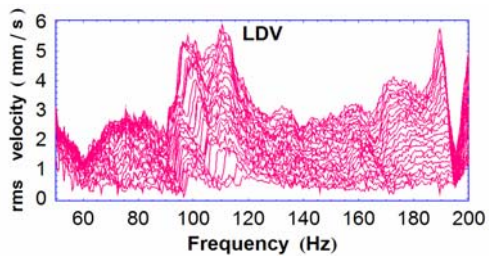
Figure G-10　　　　　　　$x = -6\ cm$
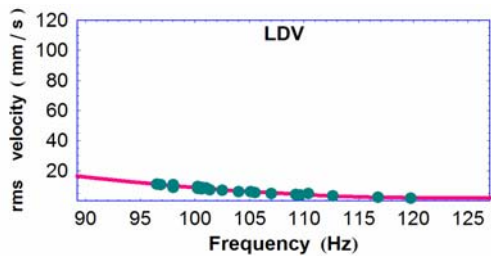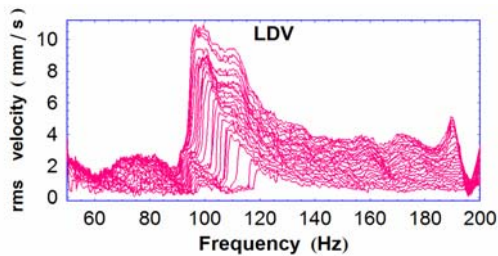
Figure G-11 $x = -5\,cm$
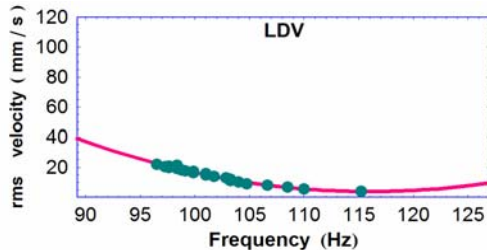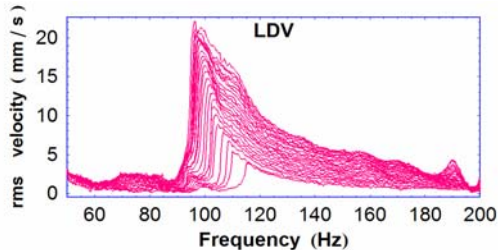
Figure G-12 $x = -4\,cm$
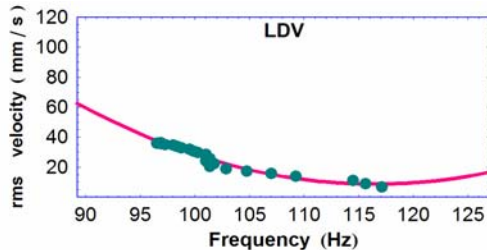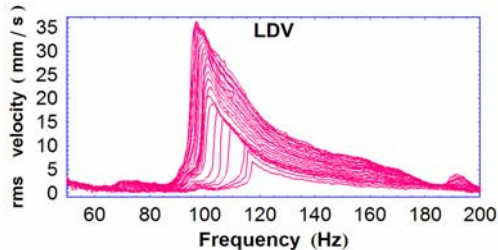
Figure G-13 $x = -3\,cm$
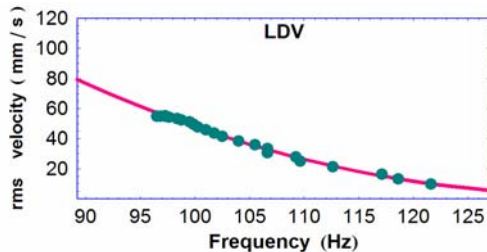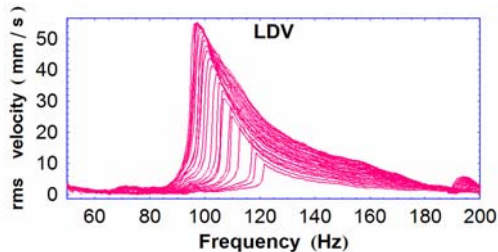
Figure G-14 $x = -2\,cm$
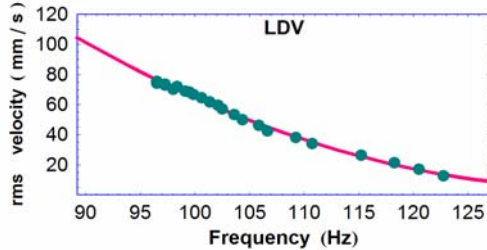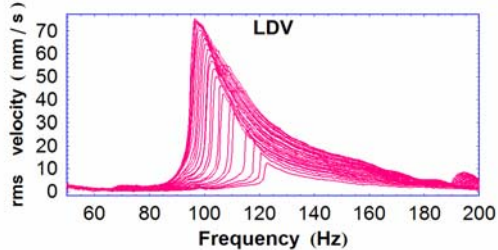
Figure G-15 $x = -1\,cm$
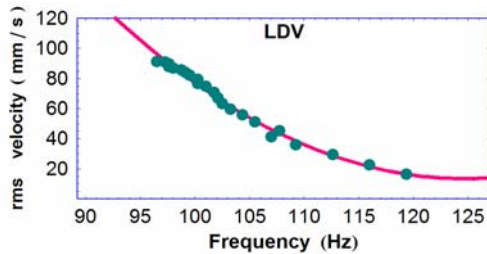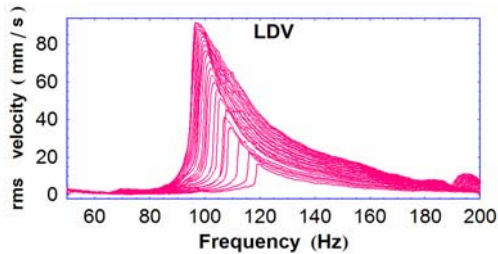
Figure G-16 $x = 0\ cm$
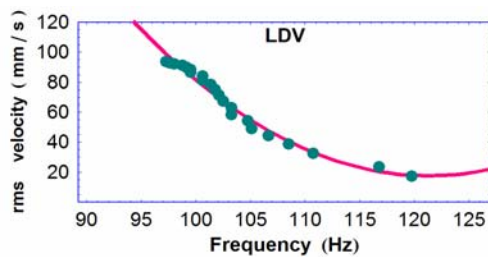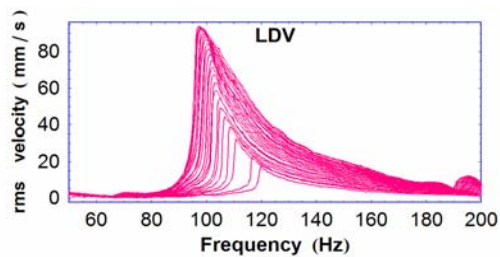
Figure G-17 $x = 1\ cm$
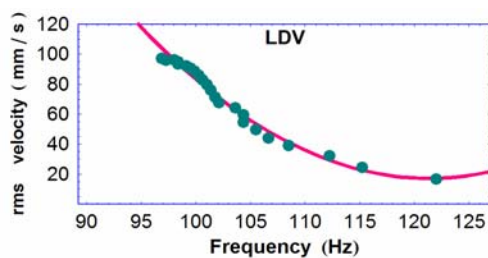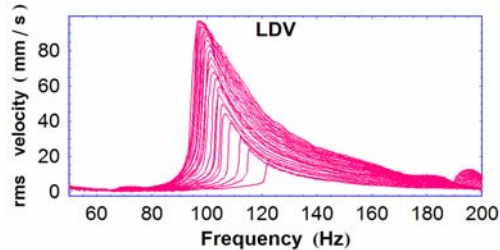
Figure G-18 $x = 2\ cm$
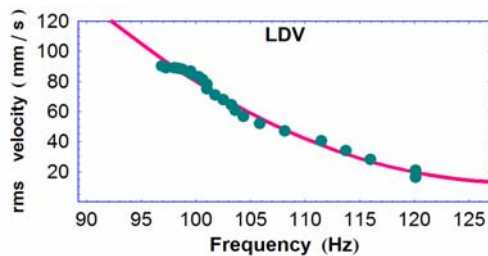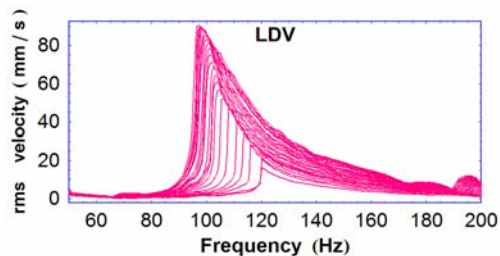
Figure G-19 $x = 3\ cm$
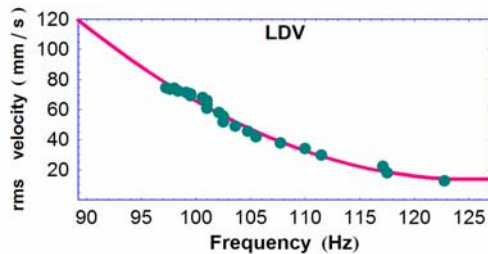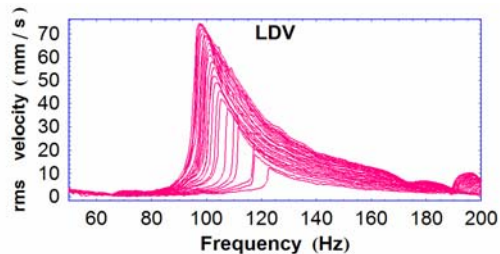
Figure G-20 $x = 4\ cm$
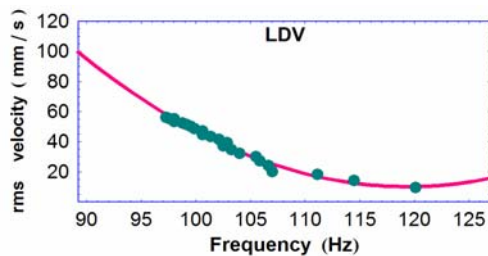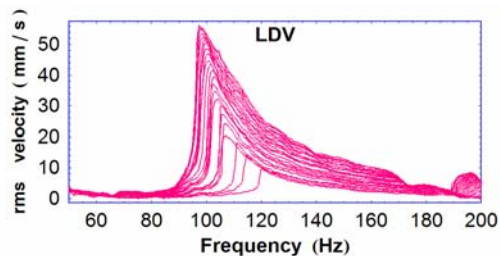
Figure G-21 $x = 5\ cm$
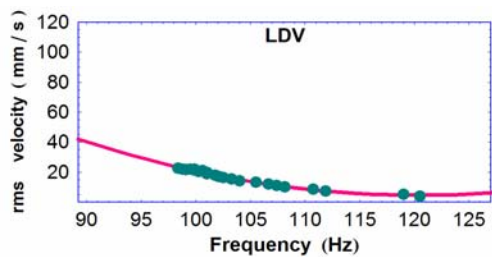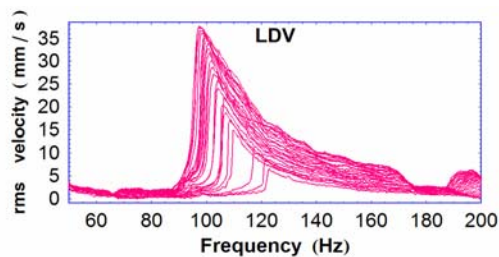
Figure G-22 $x = 6\ cm$
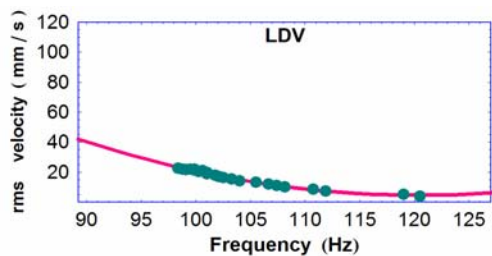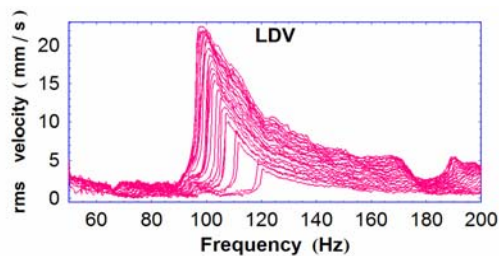
Figure G-23 $x = 7\ cm$
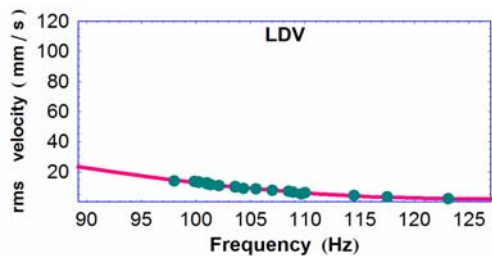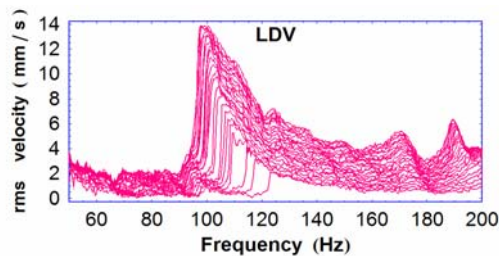
Figure G-24 $x = 8\ cm$
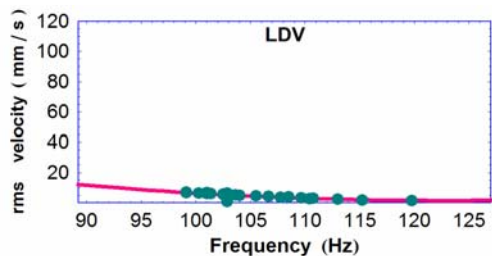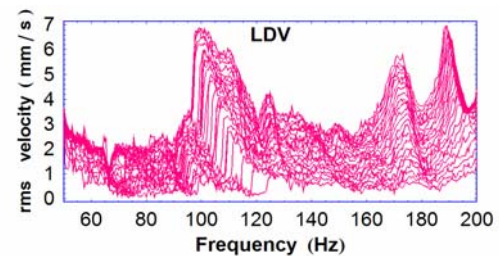
Figure G-25 $x = 9\ cm$
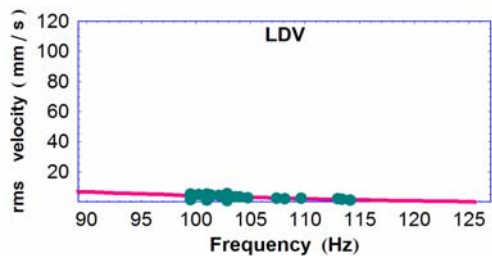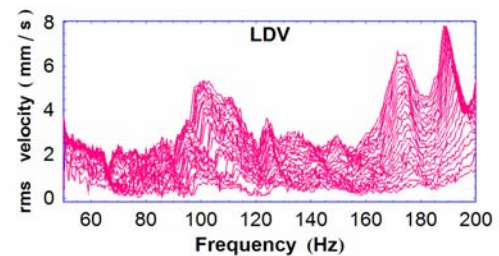
Figure G-26 $x = 10\,cm$
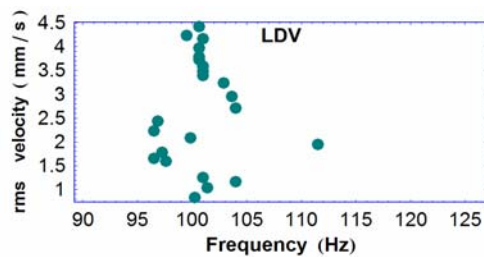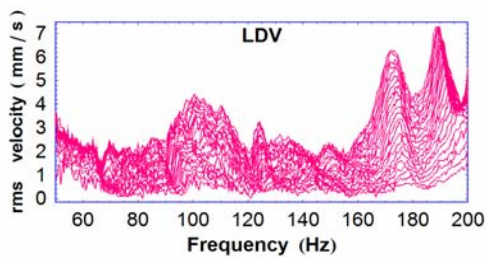
Figure G-27 $x = 11\,cm$
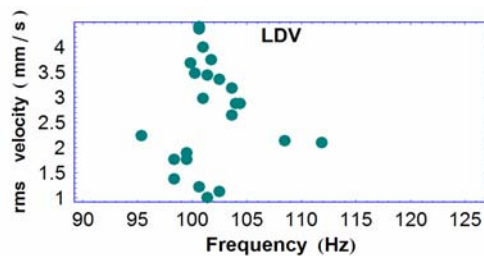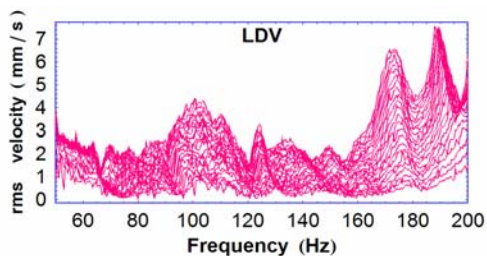
Figure G-28 $x = 12\,cm$
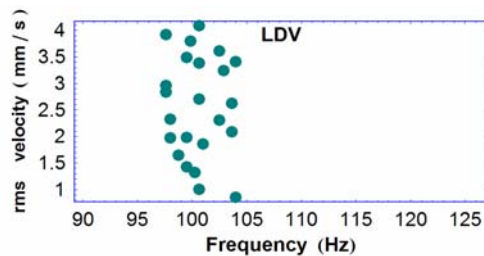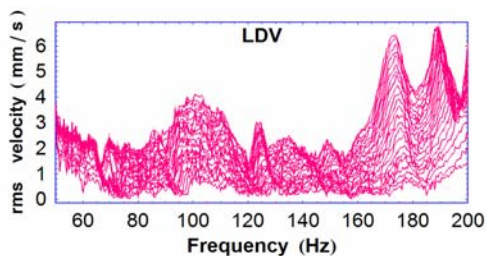
Figure G-29 $x = 13\,cm$
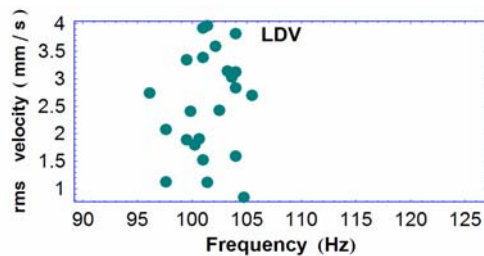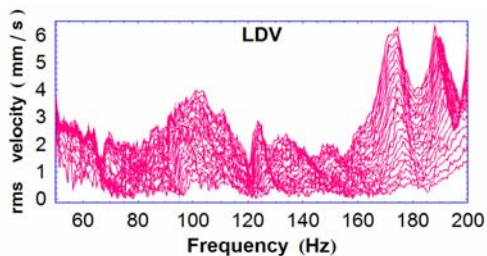
Figure G-30 $x = 14\,cm$
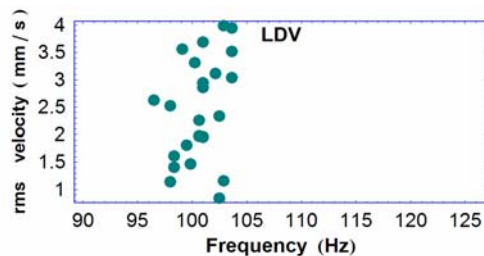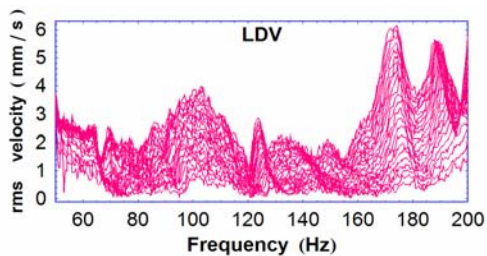
Figure G-31

$$x = 15\,cm$$
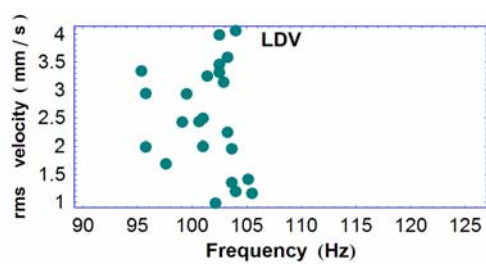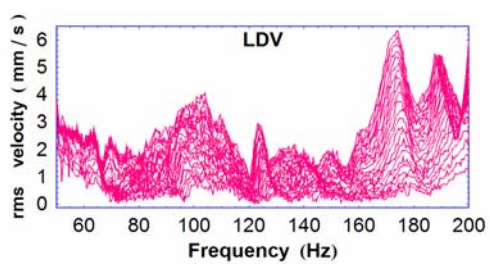
Appendix H – Two-Dimensional Soil Surface Vibration Profiles

Figure H-1
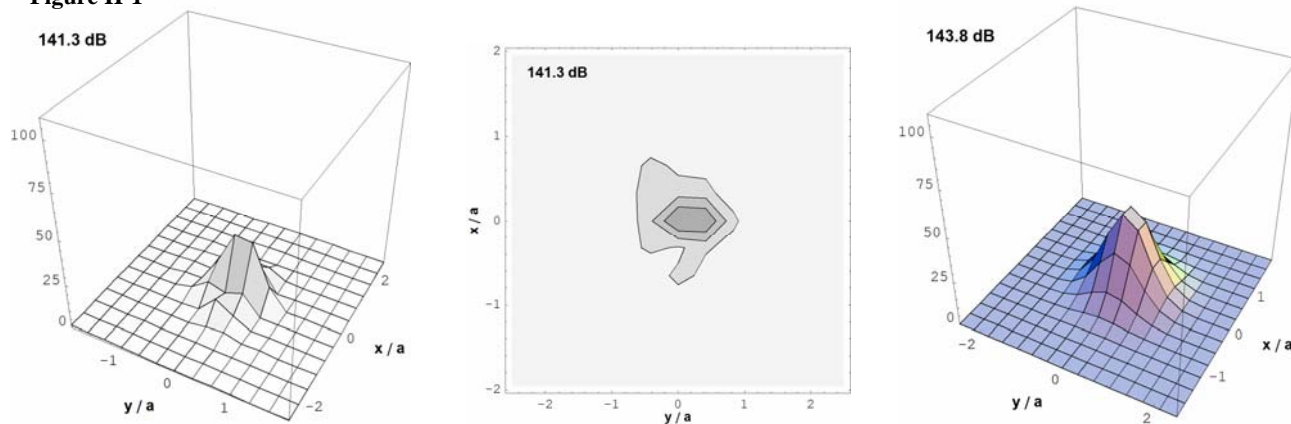
Figure H-2

Figure H-3

Figure H-4

147.4 dB

147.4 dB

147.4 dB

Figure H-5

148.7 dB

148.7 dB

148.7 dB

Figure H-6

149.9 dB

149.9 dB

149.9 dB
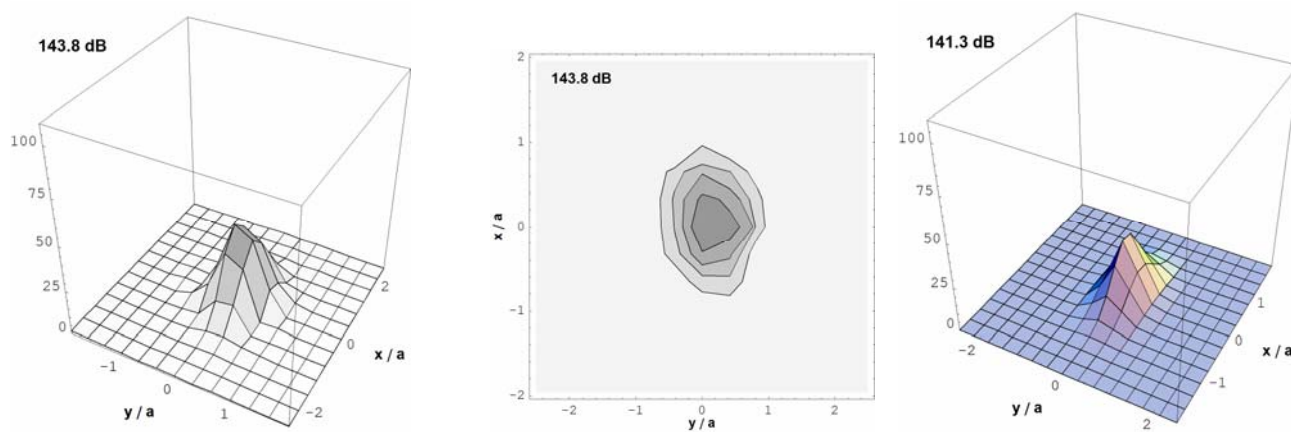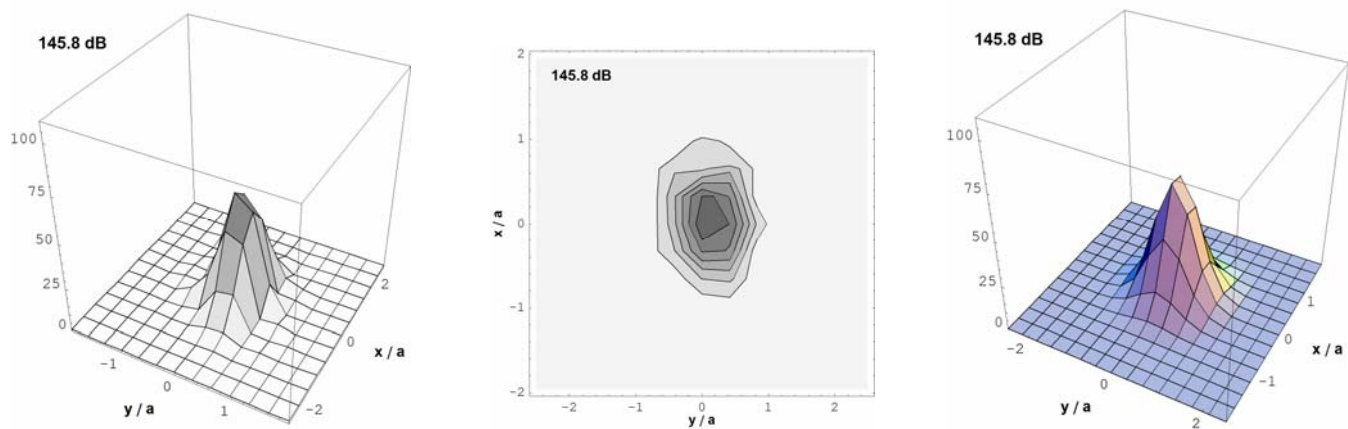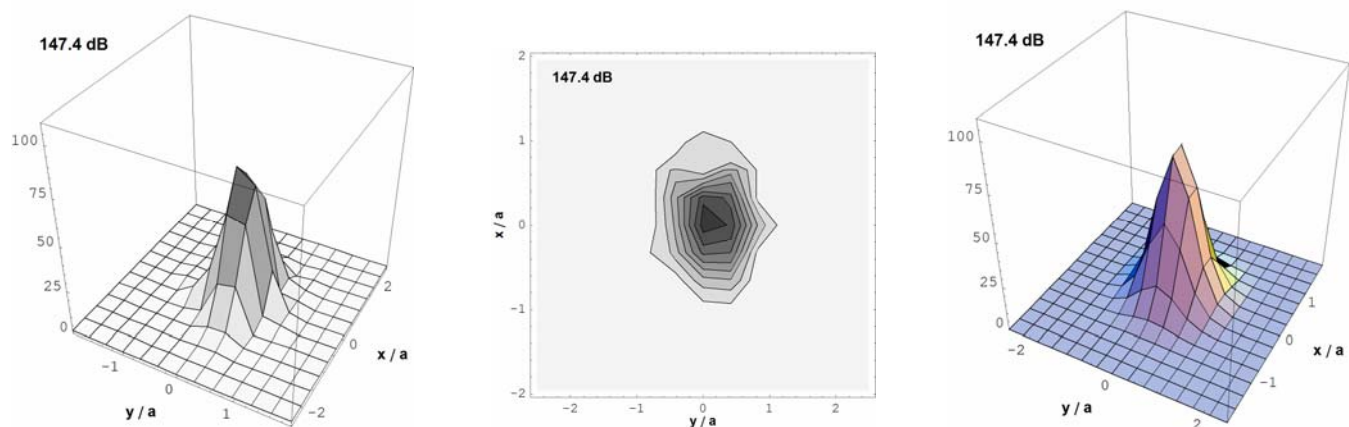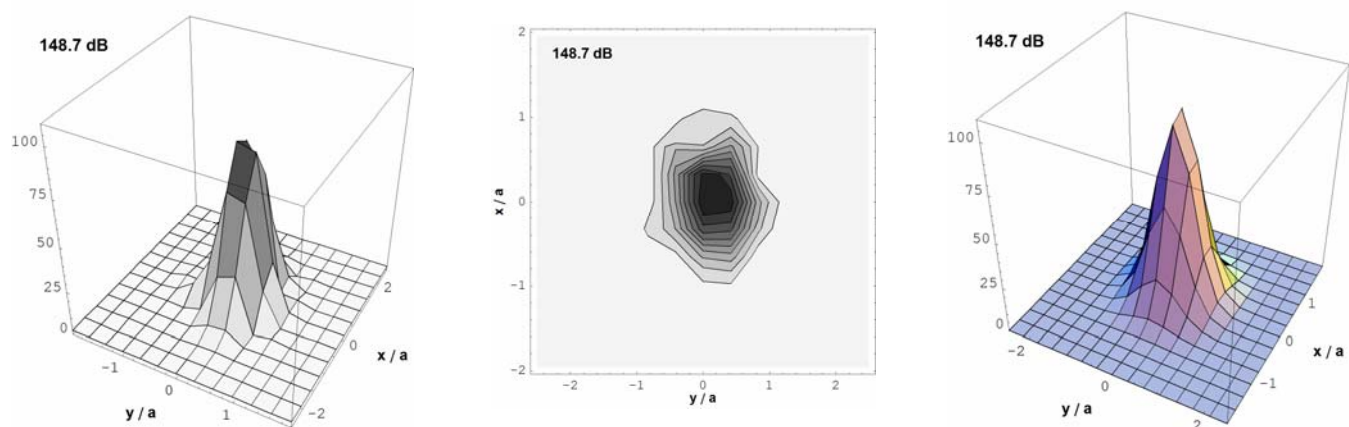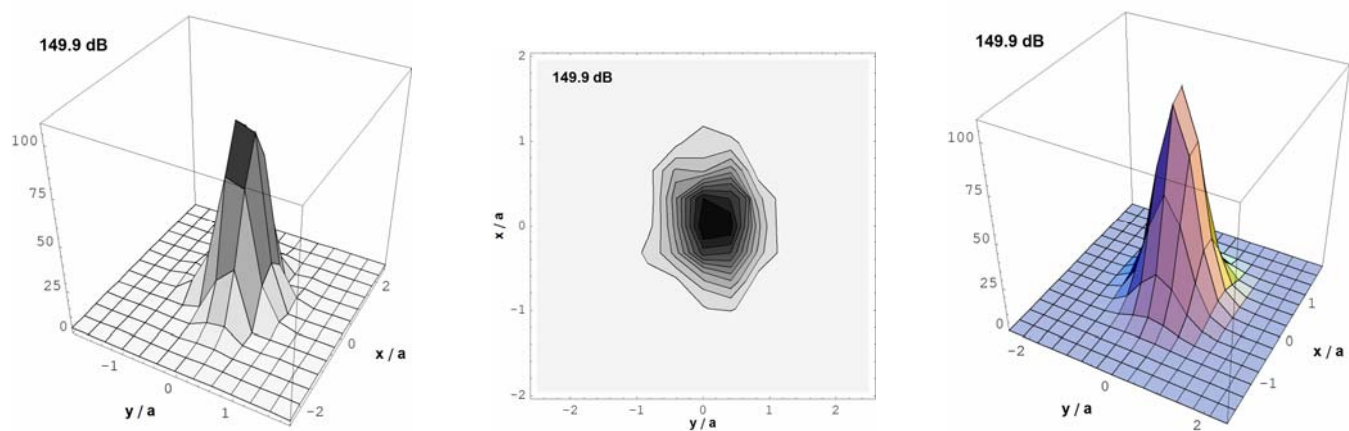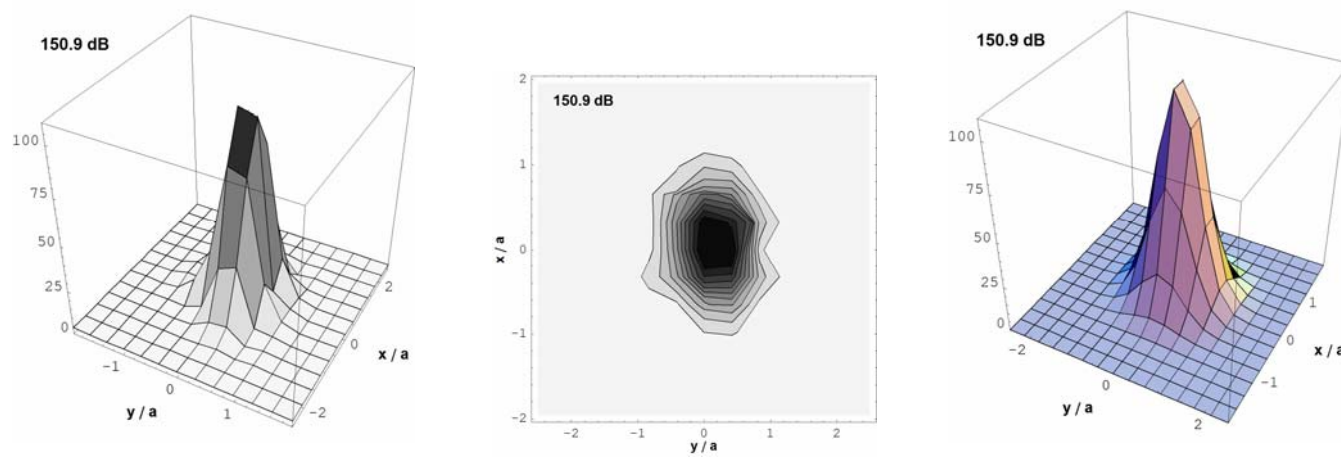
Figure H-7

Appendix I – Buried VS 1.6 Anti-tank Landmine: Resonant Tuning Curves and Backbone Curves

Figure I-1
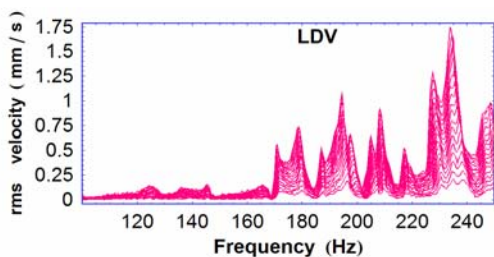
$x = -30.5\,cm$
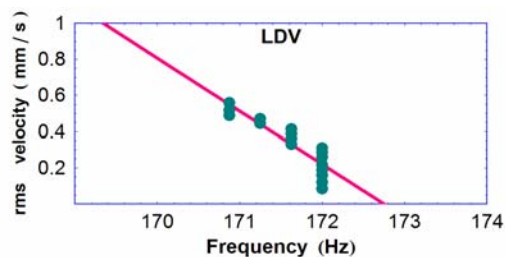
Figure I-2
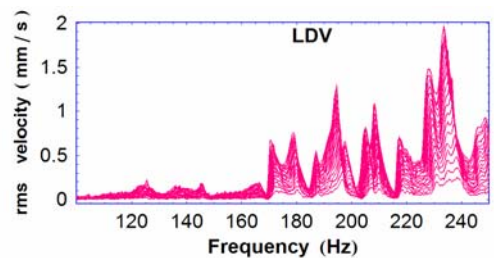
$x = -28.0\,cm$
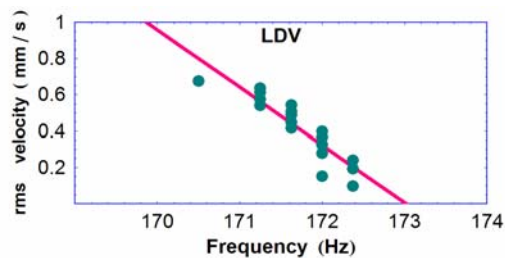
Figure I-3
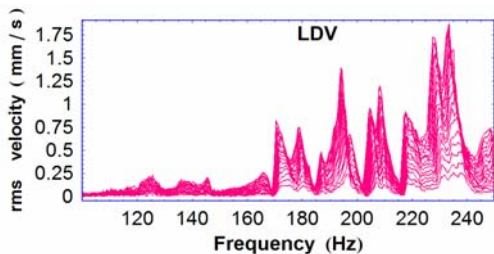
$x = -25.4\,cm$
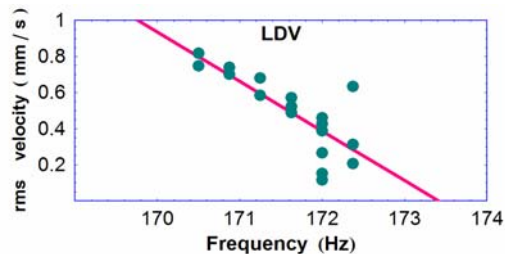
Figure I-4
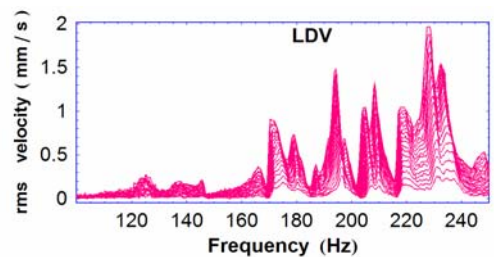
$x = -22.9\,cm$
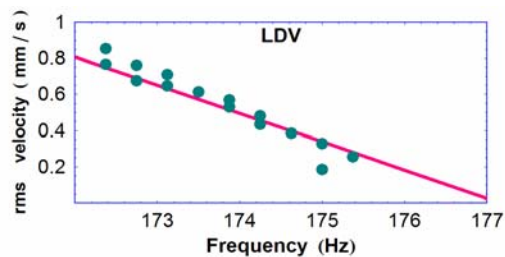
Figure I-5
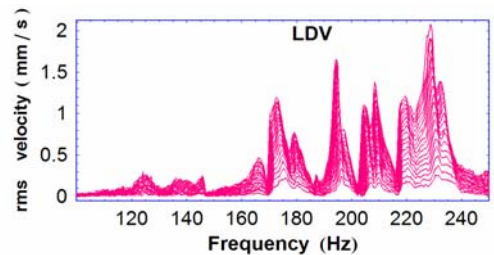
$x = -20.3\,cm$
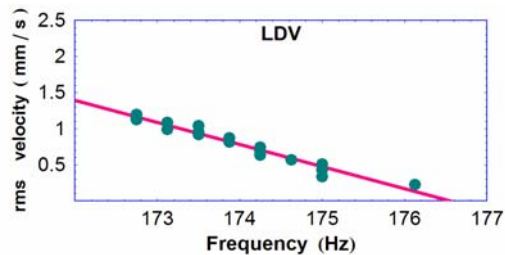
Figure I-6
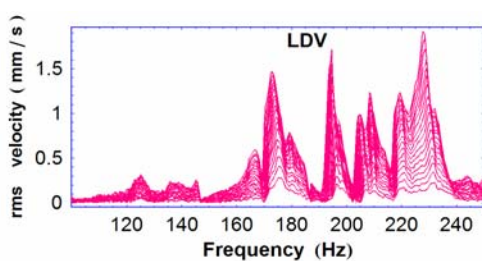
$x=-17.8\,cm$
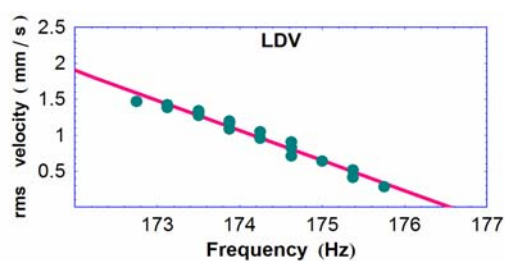
Figure I-7
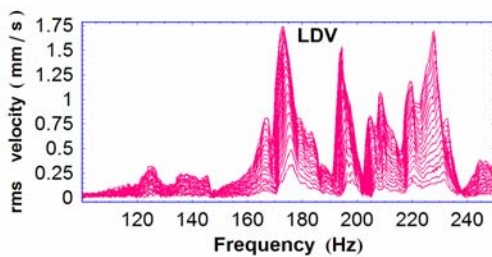
$x=-15.2\,cm$
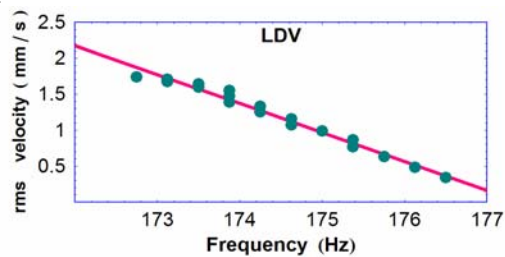
Figure I-8
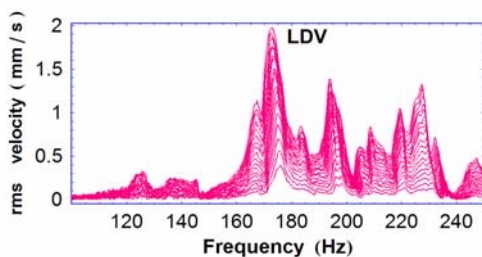
$x=-12.7\,cm$
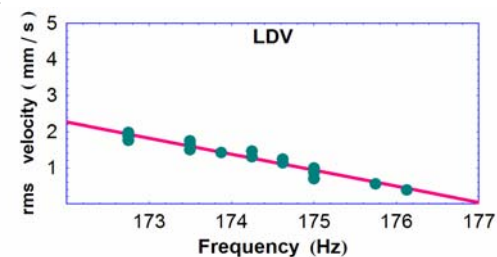
Figure I-9
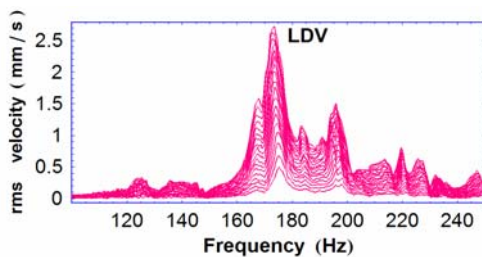
$x=-10.2\,cm$
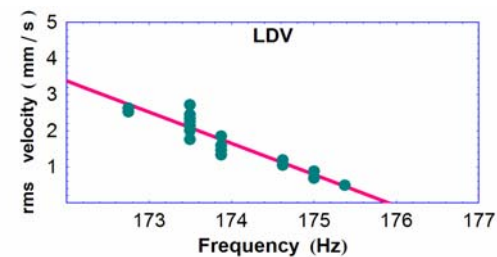
Figure I-10
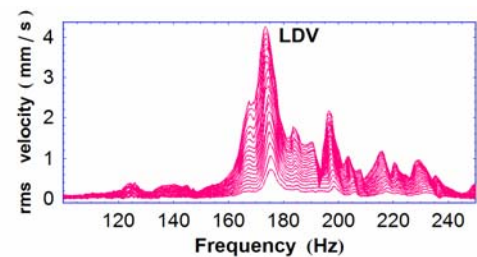
$x=-7.6\,cm$
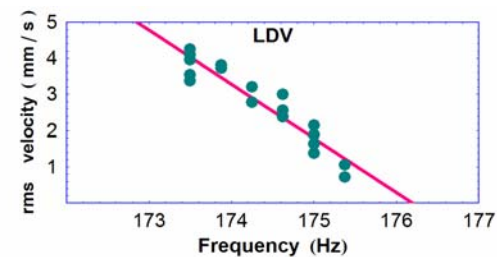
Figure I-11
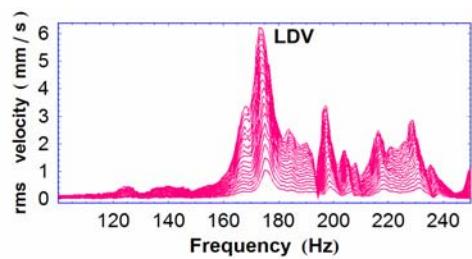
$x=x=-5.1\,cm$
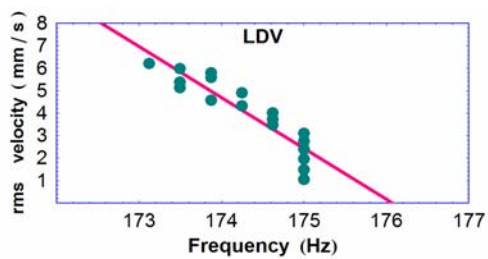
Figure I-12
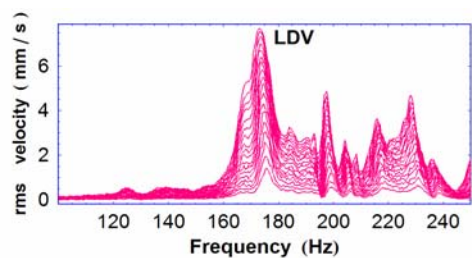
$x=x=-2.5\,cm$
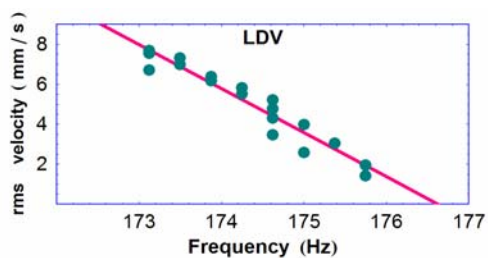
Figure I-13
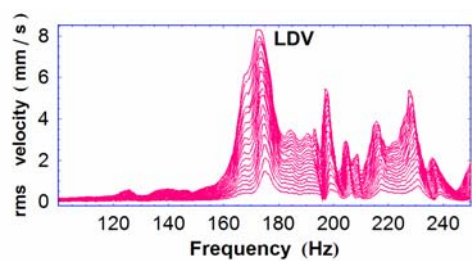
$x=0.0\,cm$
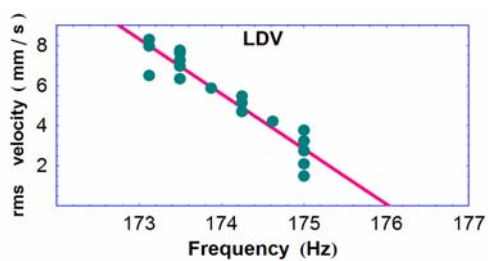
Figure I-14
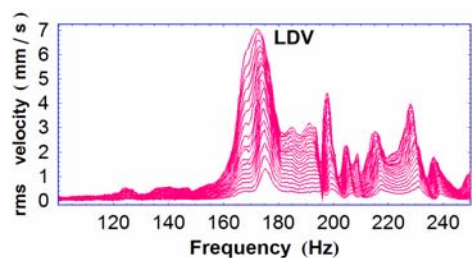
$x=2.5\,cm$
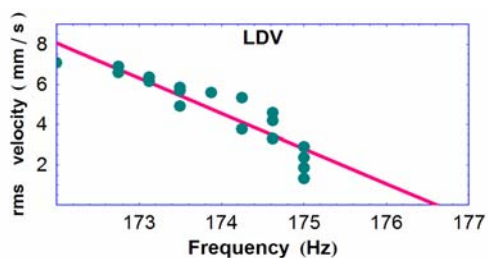
Figure I-15
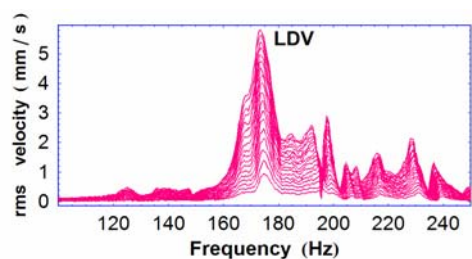
$x=5.1\,cm$
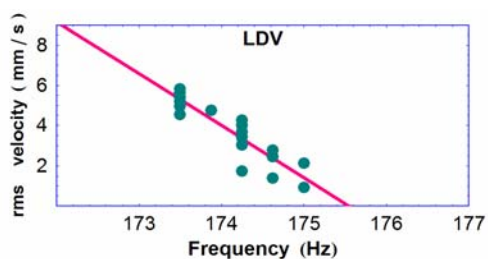
Figure I-16
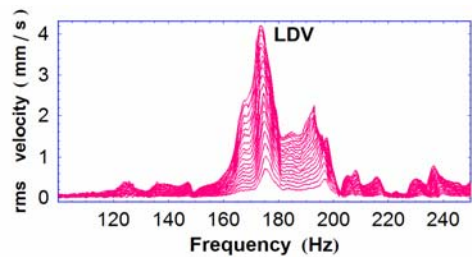
$x = 7.6\,cm$
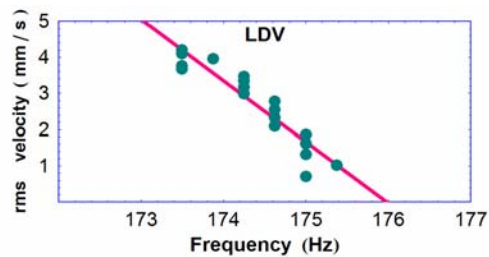
Figure I-17
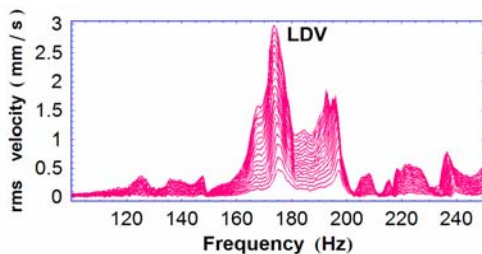
$x = 10.2\,cm$
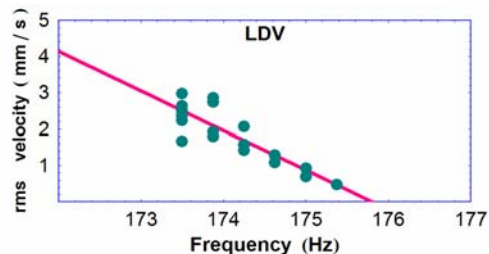
Figure I-18
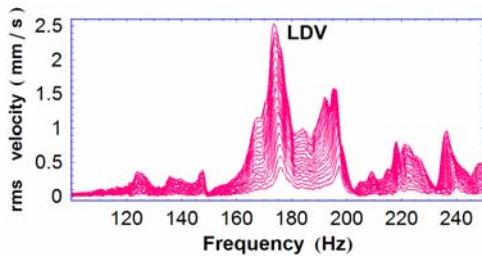
$x = 12.7\,cm$
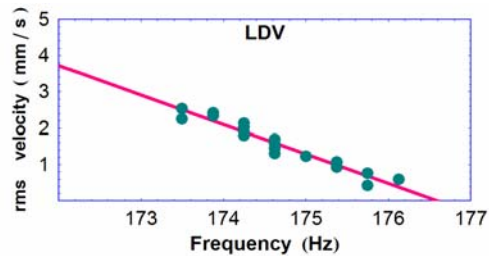
Figure I-19
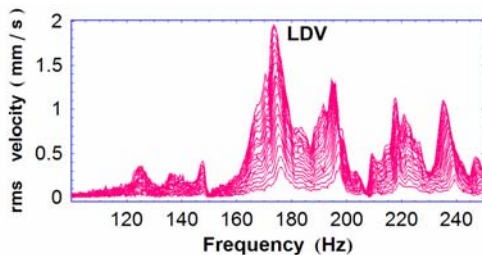
$x = 15.2\,cm$
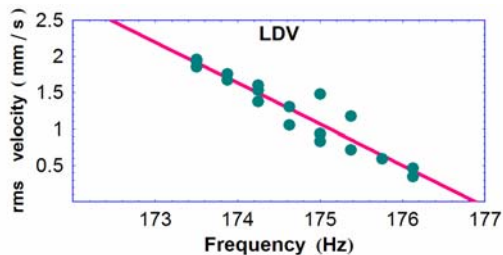
Figure I-20
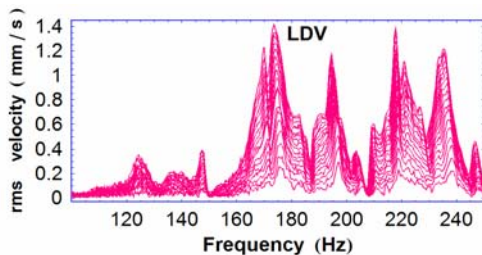
$x = 17.8\,cm$
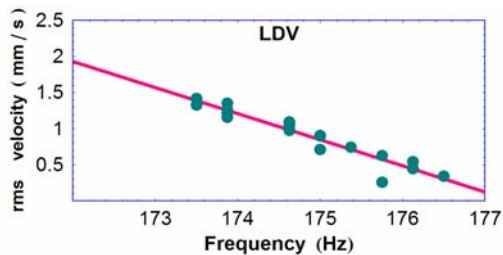
Figure I-21 $x = 20.3\,cm$
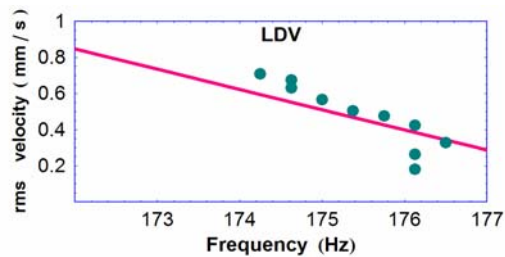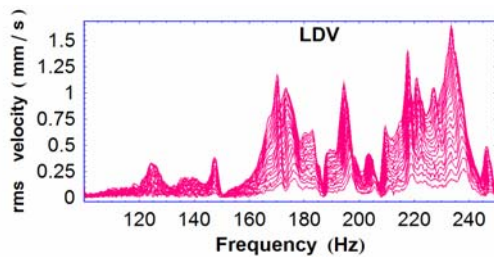
Figure I-22 $x = 22.9\,cm$
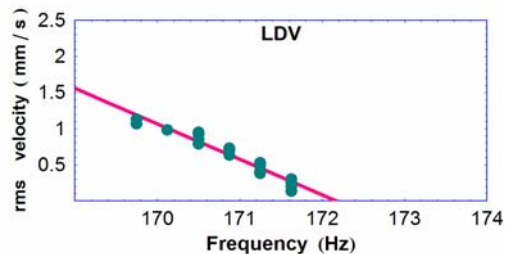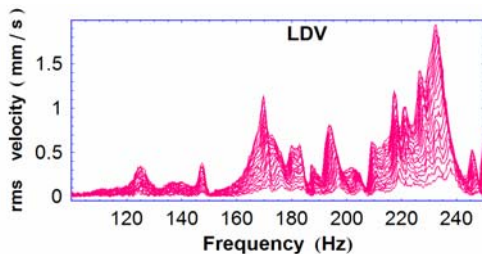

Figure I-23 $x = 25.4\,cm$
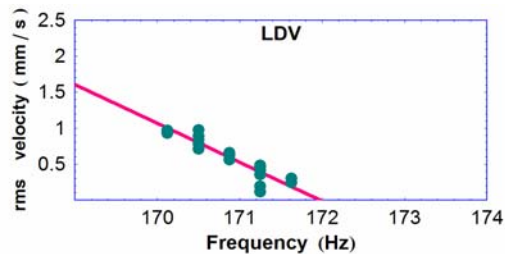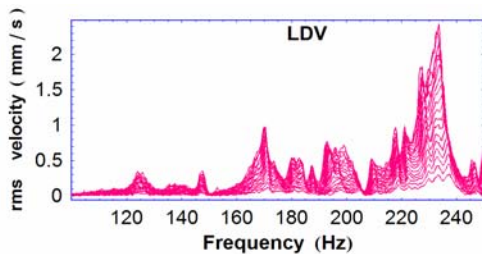
Figure I-24 $x = 27.9\,cm$
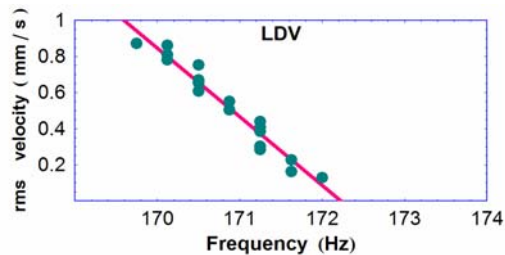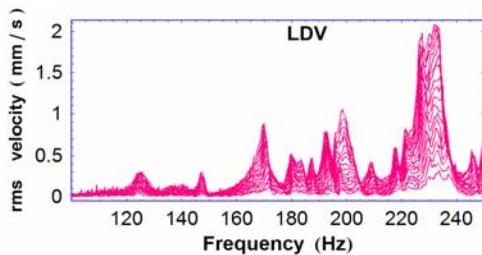
Figure I-25 $x = 30.5\,cm$
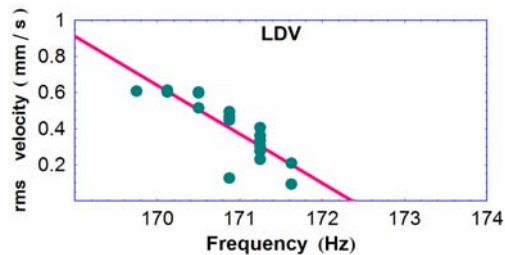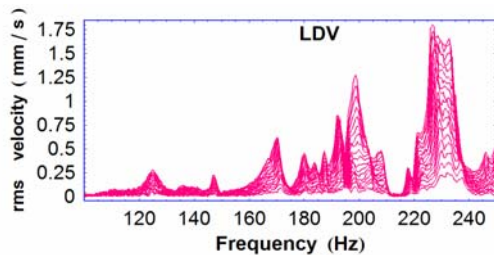
Bibliography

Benthar, M., El Aqra, H., El Guerjouma, R., Griffa, M., and Scalerandi, M., "Hysteretic elasticity in damaged concrete: Quantitative analysis of slow and fast dynamics," Phys. Rev. B, **73**, 014116 (2006).

Bolton, M.D., and Wilson, J.M.R, "An experimental and theoretical comparison between static and dynamic torsional soil tests," Geotechnique, **39**, No. 4, 585-599 (1989).

Capecchi, D., and Vestroni, F., "Steady-State Dynamic Analysis of Hysteretic Systems," J. Eng. Mech., **111**, No. 12, 1515-1531 (1985).

Caughey, T.K., "Random excitation of a System with Bilinear Hysteresis," J. Appl. Mech.: Trans. AMSE (1960).

Delsanto, P.P., Johnson, P.A., Scalerandi, M., and TenCate, J.A., "LISA simulations of time-reversed acoustic and elastic wave experiments," J. Phys. D: Appl. Phys., **39**, 3145-3152 (2002).

Freidlin, M.I., Mayergoyz, I.D., and Pfeiffer, R., "Noise in hysteretic systems and stochastic processes on graphs," Phys. Rev. E, **62**, No. 2, 1850-1855 (2000).

Gliozzi, A.S., Griffa, M., and Scalerandi, M., "Efficiency of time-reversed acoustics for nonlinear damage detection in solids," J. Acoust. Soc. Am., **120**, No. 5, 2506-2517 (2006).

Gliozzi, A.S., Nobili, M., and Scalerandi, M., "Modelling localized nonlinear damage and analysis of its influence on resonance frequencies," J. Phys. D: Appl. Phys., **39**, 3895-3903 (2006).

Guyer, R.A., McCall, K.R., Boitnott, G.N., Hilbert Jr., L.B., and Plona, T.J., "Quantitative implementation of Preisach-Mayergoyz space to find static and dynamic elastic moduli in rock," J. Geophys. Res., **102** (B3), 5281-5293 (1997).

Guyer, R.A., McCall, K.R., and Van Den Abeele, K., "Slow elastic dynamics in a resonant bar of rock," Geophys. Res. Lett., **25**, No. 10, 1585-1588 (1998).

Hirsekorn, S., "Spectral Analysis of a PM Space in the Simulation of Nonlinear Ultrasonic Wave Propagation," WCU 2003, Paris, September 7-10, 2003.

Iwan, W.D., "On a Class of Models for the Yielding Behavior of Continuous and Composite Systems," J. Appl. Mech.: Trans. ASME (1967).

Iwan, W.D., "The Steady-State Response of a Two-Degree-of-Freedom Bilinear Hysteretic Model," J. Appl. Mech.: Trans. AMSE (1965).

Iwan, W.D., "The Steady-State Response of the Double Bilinear Hysteretic Model," J. Appl. Mech.: Trans. AMSE (1965).

Johnson, P., and Sutin, A., "Slow dynamics and anomalous nonlinear fast dynamics in diverse solids," J. Acoust. Soc. Am., **117**, No. 1, 124-130 (2005).

Korman, M.S., and Sabatier, J.M., "Nonlinear acoustic techniques for landmine detection," J. Acoust. Soc. Am., **116**, No. 6, 3354-3369 (2004)

Korman, M.S., Sabatier, J.M., Pauls, K.E., and Genis, S.A., "Nonlinear acoustic landmine detection: Comparison of off-target soil background and on-target soil-mine nonlinear effects," in *Detection and Remediation Technologies for Mines and Minelike Targets XI*, Proc. of SPIE, **6217**, 62170Y (2006).

Lacarbonara, W., and Vestroni, F., "Nonclassical Responses of Oscillators with Hysteresis," Nonlinear Dynamics, **32**, 235-258 (2003).

Liu, C., and Nagel, S.R., "Sound in Sand," Phys. Rev. Lett., **68**, No. 15, 2301-2305 (1992).

Moussatov, A., Castagnède, B., and Gusev, V., "Frequency up-conversion and frequency down-conversion of acoustic waves in damaged materials," Phys. Lett. A, **301**, 281-290 (2002).

Nazarov, V.E., Radostin, A.V., Ostrovsky, L.A., and Soustova, I.A., "Wave Processes in Media with Hysteretic Nonlinearity: Part 2," Acoust. Phys., **49**, No. 4, 444-448 (2003).

Nobili, M. and Scalerandi, M., "Temperature effects on the elastic properties of hysteretic elastic media: Modeling and simulations," Phys. Rev. B, **69**, 104105 (2004).

Ostrovsky, L.A, "Wave interaction in acoustic resonators with and without hysteresis," J. Acoust. Soc. Am., **116**, No. 6, 3348-3353 (2004).

Pyke, R., "Nonlinear Soil Models for Irregular Cyclic Loadings," J. Geotech. Eng. Div., **105**, No. GT6, 715-726 (1979).

Scalerandi, M., Delsanto, P.P., and Johnson, P.A., "Stress induced conditioning and thermal relaxation in the simulation of quasi-static compression experiments," J. Phys. D: Appl. Phys., **36**, 288-293 (2003).

Snowdon, J.C., "Forced Vibration of Internally Damped Circular and Annular Plates with Clamped Boundaries," J. Acoust. Soc. Am., **50**, No. 3, 846-858 (1971).

Snowdon, J.C., "Forced Vibration of Internally Damped Circular Plates with Supported and Free Boundaries," J. Acoust. Soc. Am., **47**, No. 3, 882-891 (1970).

Sutin, A., Johnson, P., TenCate, J., Sarvazyan, A., "Time reversal acousto-seismic method for landmine detection," in *Detection and Remediation Technologies for Mines and Minelike Targets X*, Proc. of SPIE, **5794**, 706-716 (2005).

Vakhnenko, O.O., Vakhnenko, V.O., and Shankland, T.J., "Soft-ratchet modeling of end-point memory in the nonlinear resonant response of sedimentary rocks," Phys. Rev. B, **71**, 174103 (2005).

Vakhnenko, O.O., Vakhnenko, V.O., Shankland, T.J., and TenCate, J.A., "Strain-induced kinetics of intergrain defects as the mechanism of slow dynamics in the nonlinear resonant response of humid sandstone bars," Phys. Rev. E, **70**, 015602(R) (2004).

Van Den Abeele, K., Sutin, A., Carmeliet, J., and Johnson, P.A., "Micro-damage diagnostics using nonlinear elastic wave spectroscopy (NEWS)," NDT&E International, **34**, 239-248 (2001).

Vogl, G.W., and Nayfeh, A.H., "A reduced-order model for electrically actuated clamped circular plates," J. Micromech. Microeng., **15**, 684-690 (2005).

Whiteman, I.R., "A Mathematical Model Depicting the Stress-Strain Diagram and the Hysteresis Loop," J. Appl. Mech.: Trans. ASME, 95-100 (1959).

Wong, C.W., Ni, Y.Q., and Lau, S.L., "Steady-State Oscillation of Hysteretic Differential Model. I: Response Analysis," J. Eng. Mech., **120**, No. 11, 2271-2298 (1994).

Wong, C.W., Ni, Y.Q., and Ko, J.M., "Steady-State Oscillation of Hysteretic Differential Model. II: Performance Analysis," J. Eng. Mech., **120**, No. 11, 2299-2325 (1994).

References

[1] International Campaign to Ban Landmines. *Landmine Monitor Report 2005: Toward a Mine-Free World*, (New York: Human Rights Watch, October 2005).

[2] J. M. Sabatier and N. Xiang, "Laser-Doppler based acoustic-to-seismic detection of buried mines," in *Detection and Remediation Technoligies for Mines and Minelike Targets IV*, Proc. of SPIE, **3710** (1999).

[3] J. M. Sabatier and N. Xiang, "An investigation of a system that uses acoustic-to-seismic coupling to detect buried anti-tank landmines," IEEE Trans. Geoscience and Remote Sensing **39**, 1146-1154 (2001).

[4] D. Donskoy, A. Ekimov, N. Sedunov, and M. Tsionskiy, "Nonlinear seismo-acoustic land mine detection and discrimination," J. Acoust. Soc. Am. **111**, No. 6, 2705–2714 (2002).

[5] W.D. Iwan, "A Distributed-Element Model for Hysteresis and its Steady-State Dynamic Response," J. Appl. Mech.: Trans. ASME, **66**, 1–8 (1966).

[6] P.P. Delsanto and M. Scalerandi, "Modeling nonlcassical nonlinearity, conditionoing, and slow dynamics effects in mesoscopic elastic materials," Phys. Rev. B, **68**, 064107 (2003).

[7] T.K. Caughey, "Sinusoidal Excitation of a System with Bilinear Hysteresis," J. Appl. Mech.: Trans ASME, 640-643 (1960).

[8] R.A. Guyer, J. TenCate, and P. Johnson, "Hysteresis and the Dynamic Elasticity of Consolidated Granular Materials," Phys. Rev. Lett., **82**, No. 16, 3280-3283 (1999).

[9] L.E. Kinsler and A.R. Frey, *Fundamentals of Acoustics*, 2nd Ed., New York: John Wiley and Sons, Inc., 9-10 (1962).

[10] L.E. Kinsler, A.R. Frey, A.B. Coppens, J.V. Sanders, *Fundamentals of Acoustics*, John Wiley and Sons. 59 (1982).

[11] W.D. Iwan, "The Dynamic Response of the One Degree of Freedom bilinear Hysteretic System," Proc. Third World Conf. Earthquake Eng. (1964).

[12] T.W. Darling, J.A. TenCate, D.W. Brown, B. Clausen, and S.C. Vogel, "Neutron diffraction study of the contribution of grain contacts to nonlinear stress-strain behavior," Geophy. Res. Lett., **31**, L16604 (2004).

[13] N. Minorski, "Non-Linear Mechanics," J.W. Edwards, Ann Arbor, Mich., 1947.

[14] Paul M. Goggans, C. Ray Smith, and Ning Xiang, "Increasing speckle noise immunity in LDV-based acoustic mine detection," Proc. SPIE Int. Soc. Opt. Eng. 4038, 719 (2000).

[15] W.P. Mason, *Electromechanical Transducers and Wave Filters*, 1948.